Université de Neuchâtel

Institut de Microtechnique

Properties of light fields near sub-micro and nano-scale structures

Thèse

Présentée à la faculté des sciences
pour obtenir le grade de docteur ès sciences
par

Carsten Rockstuhl

Neuchâtel, juillet 2004

UFO Dissertation Band 441

Die Deutsche Bibliothek – CIP-Einheitsaufnahme
Ein Titeldatensatz für diese Publikation ist bei
Der Deutschen Bibliothek erhältlich.

Dissertation der Universität Neuchâtel
Datum der mündlichen Prüfung: 31.08.2004
Referenten: Dr. S. Quabis
Prof. Dr. H.P. Herzig
Prof. Dr. R. Dändliker
Prof. Dr. C. Hafner

UFO Atelier für Gestaltung & Verlag GbR · D-78476 Allensbach
Internet: www.ufo-verlag.de

ISBN 3-935511-42-6

IMPRIMATUR POUR LA THESE

Properties of light fields near sub-micro and nano-scale structures

M. Carsten ROCKSTUHL

UNIVERSITE DE NEUCHATEL

FACULTE DES SCIENCES

La Faculté des sciences de l'Université de Neuchâtel, sur le rapport des membres du jury

Mme S. Quabis (Erlangen D),
MM. H.P. Herzig (directeur de thèse),
R. Dändliker et
C. Hafner (ETH Zürich)

autorise l'impression de la présente thèse.

Neuchâtel, le 17 septembre 2004

La doyenne:

Prof. M. Rahier

Liste de Publications

Cette thèse est une collection des publications scientifiques de l'auteur dans le domaine de micro et nano optique :

I C. Rockstuhl, M. Salt and H. P. Herzig, "Application of the Boundary Element Method to the interaction of light with single and coupled metallic nano particles", J. Opt. Soc. Am. A, Vol. 20, 2003, 1969-1973

II C. Rockstuhl, M. Salt and H. P. Herzig, "Analyzing the scattering properties of coupled metallic nano-particles", J. Opt. Soc. Am. A, Vol. 21, 2004, 1761-1768

III C. Rockstuhl, M. Salt and H. P. Herzig, "Analyzing the phonon response of Silicon Carbide micro- and nano-particles using the Boundary Element Method", accepted for publication in J. Opt. Soc. Am. B

IV C. Rockstuhl and H. P. Herzig, "Wavelength dependent optical force on elliptical silver cylinders at plasmon resonance", Opt. Lett., Vol. 29, 2004, 2181-2183

V C. Rockstuhl and H. P. Herzig, "Rigorous diffraction theory applied to the analysis of the optical force on elliptical nano- and micro-cylinders", J. Opt. A: Pure Appl. Opt., Vol. 6, 2004, 921-931

VI C. Rockstuhl and H. P. Herzig, "Calculation of the torque on dielectric elliptical cylinders", accepted for publication in J. Opt. Soc. Am. A

VII C. Rockstuhl, M. Salt and H. P. Herzig, "Theoretical and experimental investigation of phase singularities generated by optical micro- and nano-structures", J. Opt. A: Pure Appl. Opt., Vol. 6, 2004, S271-S276

VIII C. Rockstuhl, M. Salt and H. P. Herzig, "Investigation of the basic properties of phase singularities generated by a phase bar or trench", Optics Communications, Vol. 235, 2004, 11-21

IX C. Rockstuhl, A. A. Ivanovskyy, M. S. Soskin, M. Salt, H. P. Herzig and R. Dändliker, "High-resolution measurement of phase singularities produced by computer-generated holograms", accepted for publication in Optics Communication

Application of the Boundary Element Method to the interaction of light with single and coupled metallic nano particles

Carsten Rockstuhl, Martin Guy Salt, Hans Peter Herzig

University of Neuchâtel, Institute of Microtechnology,
Rue A.-L. Breguet 2, CH-2000 Neuchâtel, Switzerland

July 23, 2004

Abstract

The Boundary Element Method is applied to the interaction of light with resonant metallic nano particles. At a certain wavelength, excitation of a surface plasmon takes place which leads to a resonantly enhanced near-field amplitude and a large scattering cross section. The resonance wavelength for different scatterer geometries is determined. Alteration of the scattering properties in the presence of other metallic nano particles is discussed. To treat this problem, a novel formulation of the Boundary Element Method is presented, which solves the interaction problem for all the coupled particles.

OSICS codes: 050.1960, 240.6680.

1 Introduction

When illuminating metallic nano particles at an appropriate wavelength, excitation of surface plasmons can take place. Surface plasmons are a collective oscillation of free electrons within the material[1]. The excitation leads to a resonantly enhanced near-field amplitude and a large scattering cross section (SCS) for a narrow wavelength band. The principal effect has been known for centuries. Unfortunately, the conditions for the appearance of the resonances can only be predicted analytically in the case of elliptical particles within the electrostatic limit (dimensions much smaller than the wavelength)[2]. For example, in the ideal case of an infinite circular cylinder surrounded by air[3] the material must have a relative complex permittivity of $\epsilon_{2D} = -1$ and a sphere of $\epsilon_{3D} = -2$. Silver and gold are two materials which approximately fulfill this condition. Their resonances appear in the blue region of the visible spectrum. For other structures and even for the exact solution of spherical particles having a finite feature size, prediction of the scattering properties asks for an exact solution of Maxwell's Equations. In the course of time, various numerical tools have been presented. Moreno and co-workers used the Multiple Multipole Method(MMP) [4], Schatz employed the Discrete Dipole Approximation (DDA) to the problem [5] and Kottmann and Martin in a series of pioneering publications applied Green's Dyadic Function to the problem [6, 7].
In the present work we have used the Boundary Element Method (BEM) to simulate the interaction of light with resonant metallic nano particles. An advantage of this method is its numerical stability and the relatively easy incorporation of additional scatterers and the subsequent solution of the coupled particle problem.

2 Scattering cross section and near-field amplitudes for a single particle

The Boundary Element Method is a well known technique in fields such as acoustics, fluid mechanics, elasticity and fracture mechanics[8]. But only a few authors have applied this method to micro-optical problems. The method was used mainly for analyzing the diffraction properties of mirrors[9], layered spheres[10] and cylindrical microlenses[11]. The present implementation is based on some pioneering work conducted by Prather *et al*[12, 13]. They

applied the method to Fresnel lenses.
The basic two-dimensional scattering problem consists of a homogenous scatterer having a relative permittivity of ϵ_I. It is described by its surface contour C and its outward normal $\hat{n}_I$. The structure is invariant in the third dimension z and illuminated by an incident wave-field $u^{inc}(\rho)$ from a region with a homogenous permittivity ϵ_0. ρ is an observation point in the x-y-plane. If the incoming field is TE-polarized, the field component $u(\rho)$ denotes the $E_z(\rho)$ component of the electric field. If the field is TM-polarized, $u(\rho)$ denotes the magnetic field component $H_z(\rho)$. For both cases the total field, $u^{tot}(\rho)$, is the sum of the incoming field $u^{inc}(\rho)$ and the scattered field $u^{sc}(\rho)$. The normal derivatives of the different fields with respect to the boundary are denoted by $v^{inc}(\rho)$, $v^{sc}(\rho)$ and respectively $v^{tot}(\rho)$. It is assumed that the materials are non-magnetic, i.e. the relative permeability reads as $\mu_r = 1$.
The total field in the interior region has to be a solution of the homogeneous wave equation, in the exterior region a solution of the inhomogeneous wave equation. This is due to the presence of an additional source term $f(\rho)$, which is defined on a infinite large circle. The source term describes in principal the incident wave field. The wave equations read as

$$\begin{aligned} 0 &= \nabla^2 u_I^{tot}(\rho) + k_I^2 u_I^{tot}(\rho) \quad \text{for } \rho \in I \\ -f(\rho) &= \nabla^2 u_O^{tot}(\rho) + k_O^2 u_O^{tot}(\rho) \quad \text{for } \rho \in O, \end{aligned} \tag{1}$$

with $k_{I,O} = \frac{2\pi\sqrt{\epsilon_{I,O}}}{\lambda_0}$ being the wave number in the interior (I) and exterior (O) region respectively. Applying Green's Second Identity, the boundary integral equations can be derived. They read as [12]

$$\begin{aligned} 0 &= u^{sc}(\rho_S) + \int_C \left\{ u^{sc}(\rho') \frac{\partial G_I(\rho_S, \rho')}{\partial \hat{n}_I} - p_I G_I(\rho_S, \rho') v^{sc}(\rho') \right\} dl' \\ &+ u^{inc}(\rho_S) + \int_C \left\{ u^{inc}(\rho') \frac{\partial G_I(\rho_S, \rho')}{\partial \hat{n}_I} - p_I G_I(\rho_S, \rho') v^{inc}(\rho') \right\} dl' \quad \text{for } \rho_S \in I \\ 0 &= u^{sc}(\rho_S) + \int_C \left\{ u^{sc}(\rho') \frac{\partial G_O(\rho_S, \rho')}{\partial \hat{n}_O} + p_O G_O(\rho_S, \rho') v^{sc}(\rho') \right\} dl' \quad \text{for } \rho_S \in O. \end{aligned} \tag{2}$$

$u^{inc}(\rho_S)$ and $u^{sc}(\rho_S)$ are the field values along the contour and the remaining integral terms describe the scattered contribution of the scattered field from each point of the surface[1]. It has to be kept in mind that the contour

[1] A more detailed derivation of the boundary integral equations can be found in appendix I

normal pointing in the exterior space has a different sign than that pointing in the interior space, i.e. $\hat{n}_I = -\hat{n}_O$. $G_{I,O}$ are the two-dimensional free space Green's functions in the interior and exterior region. $p_{I,O}$ is a factor that depends on the polarization. It reads as $p_{I,\,O} = 1$ in the case of TE polarization and $p_{I,\,O} = \epsilon_{I,\,O}$ for TM polarization. Eq. (2) can be cast into a set of linear equations by expanding the unknown scattered field $u^{sc}(\rho)$ and its normal derivative $v^{sc}(\rho)$ in terms of linear interpolation functions across the surface [12]. Solution of this system of linear equations gives the unknown scattered field and its derivative at the nodal points. The scattered field can then be calculated everywhere in space using

$$u^{sc}(\rho) = \int_C \left\{ u^{sc}(\rho') \frac{\partial G_O(\rho, \rho')}{\partial \hat{n}_I} - p_O G_O(\rho, \rho') v^{sc}(\rho') \right\} dl'. \tag{3}$$

In a final step the total field is calculated by adding the field distribution of the incoming wave. A detailed derivation can be found in [12, 13].

The aim of this work is the description of systems which consist of more than a single scatterer. To incorporate additional scatterers in the formulation, the incoming wave field $u_m^{inc}(\rho)$ on particle m is written as

$$u_m^{inc}(\rho_m) = u_0^{inc}(\rho_m) + \sum_{n \neq m} \int_C \left\{ u_n^{sc}(\rho_n') \frac{\partial G_O(\rho_m, \rho_n')}{\partial \hat{n}_I} - p_O G_O(\rho_m, \rho_n') v_n^{sc}(\rho_n') \right\} dl' \tag{4}$$

with $u_0^{inc}(\rho_m)$ being the illuminating source wave field on particle m and the second term describes the contribution of the scattered wave field from each other particle n on particle m. A similar expression can be found for the field derivatives of the new incoming wave field $v_m^{inc}(\rho_m)$. Inserting Eq. (4) in Eq. (2) makes it possible to derive a similar system of linear equations as in the classical BEM, but now it solves the coupled interaction for all particles. Once this system is solved, the scattered field and its derivative along the surface of each scatterer is known. The entire field is finally just a superposition of the incoming wave field and the contribution from each scatterer, calculated by Eq. (3).

In the present work we have concentrated on silver as the particle material. Its negligible imaginary part of the permittivity function in the region of interest promises sharp and strong resonant behavior over a small wavelength band. First simulations have been made partly using a Drude-model[2]. The

[2]The imaginary part can be neglected for the heuristic explanation of the effect, as the appearance of plasmons does not depend on the exact value of the imaginary part of the

dielectric constant is given by [4]

$$\epsilon_{Ag}(\omega) = 1 + \frac{i\tau\omega_p^2}{\omega(1 - i\omega\tau)}, \tag{5}$$

with the relaxation time $\tau = 1.45 \times 10^{-14}$ s and the the plasma frequency $\omega_P = 1.32 \times 10^{16}$ rad s^{-1}.

Excitation of plasmons is only possible using TM-polarized light, i.e. with a component of E normal to the surface[3]. For all structures, near-field amplitude distributions (assuming an amplitude of the illuminating wave field equal to unity) and the scattering cross section Q^{sc} as defined in [14] have been calculated. The scattering cross section is the energy radiated into the far-field.

First simulations were made for a circular cylinder having a radius of $r = 25$ nm. The structure is invariant in the third direction. Its SCS is shown in Fig 1 and the near-field amplitude for the first two surface plasmons is shown in Fig. 2. A dipole excitation takes place at $\lambda = 250$ nm and a quadrupole excitation at $\lambda = 214$ nm. The illumination direction is indicated by the arrows in Fig. 2. The near-field amplitude and likewise the SCS is strongest for the quadrupole. The different resonances cannot be discriminated by looking only at the SCS.

To investigate the influence of the shape on the plasmon response, we then analyzed elliptical cylinders. The radius of the minor axis is $r_1 = 10$ nm, the radius of the major axis is $r_2 = 20$ nm. Figure 3 shows the SCS upon illuminating from three directions (along the minor axis, along the major axis and at an angle of 45°). It can be seen that two fundamental and relatively broad resonances appear at specific wavelengths for the two principal directions. Upon illuminating along the minor axis, excitation of the dipole takes place at ≈ 266 nm. Meanwhile, illuminating along the major axis excites a dipole at ≈ 181 nm. These fundamental plasmons are likewise excited after illuminating the structure at an angle of 45° but with a somewhat lower strength. It is obvious that the resonances are related to the principal axes

dielectric constant. The imaginary part of the dielectric constant will cause only a slight damping and broadening of the response. In addition it has to be mentioned, that the used Drude-model has a significant lower imaginary part at the plasmon resonance than the real material.

[3]The present orientation of the electric field with a component of $E_z = 0$, herein defined defined as TM polarization, appears in literature due to various definition sometimes as TE polarization.

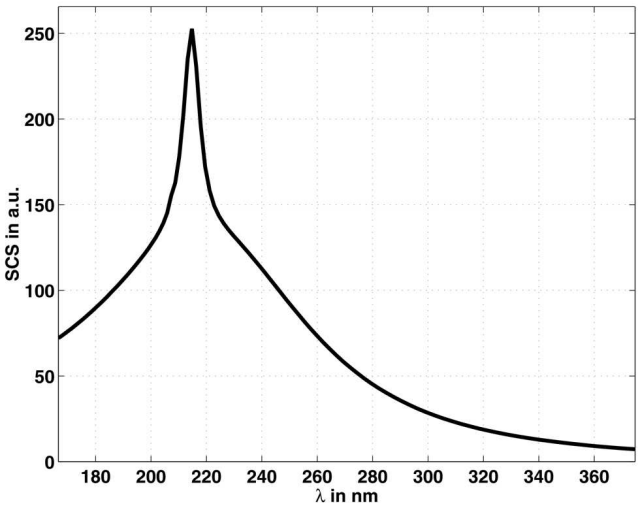

Figure 1: SCS of a silver circular cylinder(r = 25 nm) assuming a Drude-model.

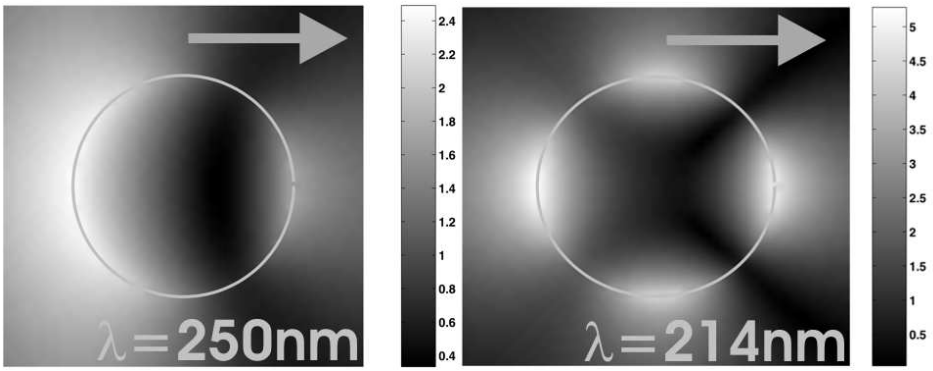

Figure 2: Near-field amplitude of the magnetic field for the excited plasmons (dipole and quadrupole).

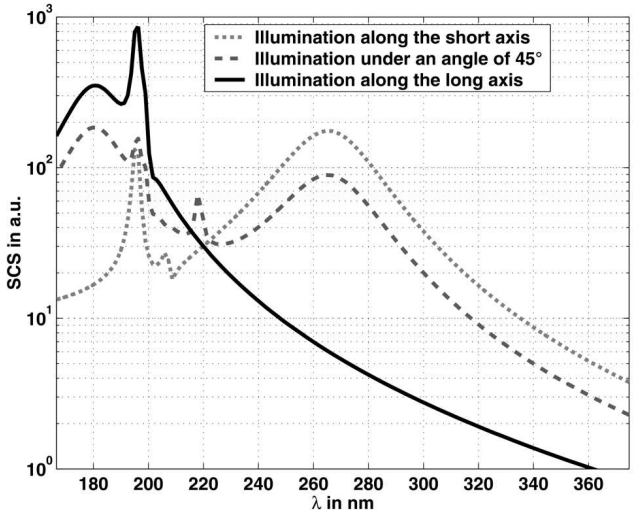

Figure 3: SCS of a silver elliptical cylinder ($r_1 = 10$ nm, $r_2 = 20$ nm) assuming a Drude-model.

of the structure and illuminating the scatterer at an angle can be understood as a projection of the incoming wave on the main axes, thus exciting both resonant plasmons. Additional higher order plasmons are excited at appropriate wavelengths. They lead to a strongly enhanced amplitude in the near-field and a huge SCS for only a small band of wavelength. The field distributions for the dipoles related to the principal axis and two supplementary excited quadrupoles are shown in Fig. 4. The quadrupoles are at $\lambda = 219$ nm for illuminating the particle under an angle of 45^o and at $\lambda = 195$ nm for illumination along the major axis.

3 Scattering cross section and near-field amplitudes for coupled particles

Coupled metallic nano particles are e.g. used in Surface Enhanced Raman Spectroscopy (SERS) experiments [16]. Recently they were used in single molecule detection [17]. A species such as Hemoglobin is placed between two metallic nano particles where field enhancement is highest. If the metallic particles are very close the resulting field value between the two particles is enhanced in such a way that it may exceed the value from the single particle

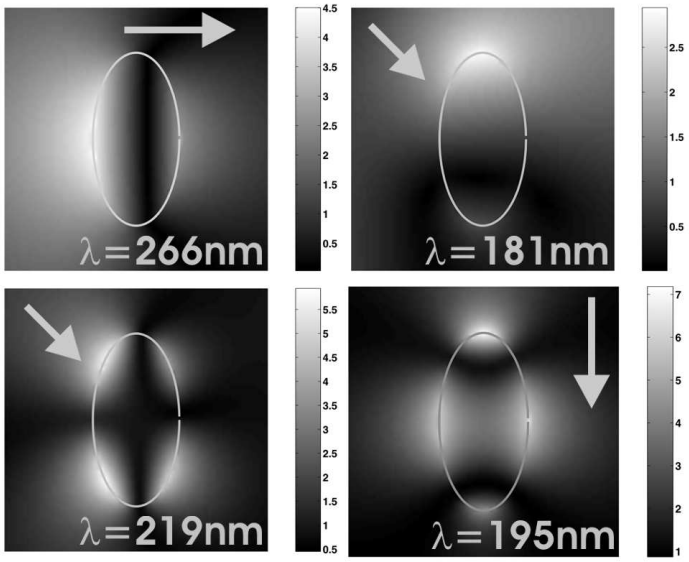

Figure 4: Near-field amplitude of the magnetic field for various plasmons of a Drude-silver elliptical cylinder ($r_1 = 10$ nm, $r_2 = 20$ nm) at different wavelengths and illumination angles.

by orders of magnitude. This field enhancement makes it possible to excite a single molecule so strongly that its Raman spectrum can be detected.
We have applied the BEM to the interaction problem of two coupled circular silver cylinders. They both have a radius of 25 nm. Again the Drude-Model for the permittivity was assumed. Figure 5 shows the SCS if the cylinders have a distance from surface to surface of 5 nm, under three different directions of illumination. In the present geometry an illumination angle of 0^o means that the two cylinders are perpendicular to the illumination direction, 90^o means that they are in-line with the illumination direction. It can be seen that the SCS shows a rather chaotic behavior for all the three illumination directions and a simple denomination of the various plasmons is not possible anymore. Some of the generated field distributions of the surface plasmons can be seen in Fig. 6. The amplitudes after illuminating the two coupled nano cylinders at an angle of 90^o (illumination is from above) are shown. In principle it can be said that the smaller the wavelength the higher the nodal number of the excited surface plasmons. The fundamental mode appears at $\lambda = 303$ nm. It is the most promising for SERS measurements because a molecule situated directly between the two resonant particles will be exposed

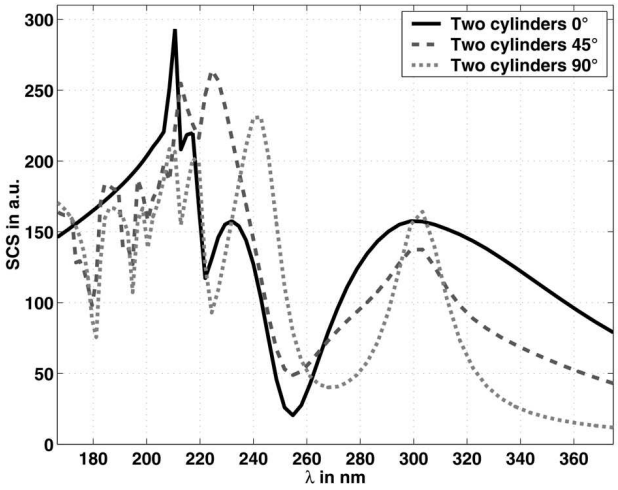

Figure 5: SCS for two coupled silver circular cylinders ($r = 25$ nm) that have a surface separation of $d = 5$ nm assuming a Drude-model.

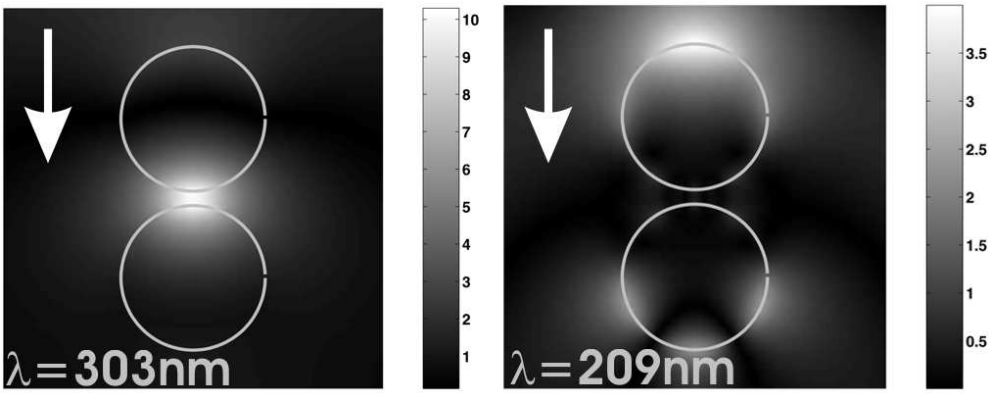

Figure 6: Near-field amplitude of the magnetic field after illuminating two coupled silver circular cylinders ($r = 25$ nm, $d = 5$ nm) from above at $\lambda_1 = 209$ nm and $\lambda_2 = 303$ nm.

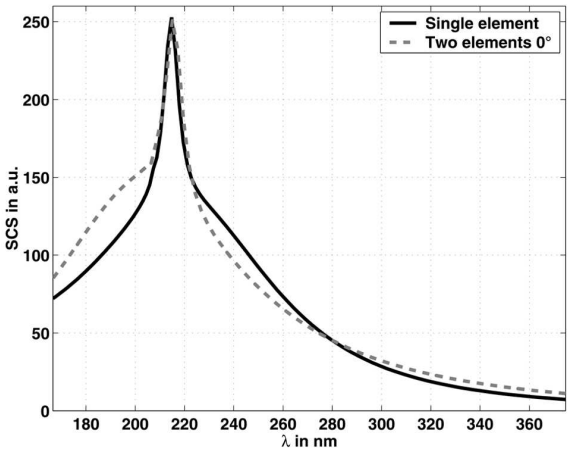

Figure 7: SCS (divided by two) for two coupled silver circular cylinders ($r = 25$ nm, $d = 75$ nm) compared with that for a single cylinder.

to a homogenous and high field. We have to admit that this richness of plasmons will be not excited if the true refractive index of silver is assumed. Nonetheless, the fundamental mode will appear. For the prediction of the behavior of the real system the real values have to be taken into account (e.g. values published by Johnson and Christy[15]). Detailed theoretical investigations of coupled particles that take the experimental real refractive index values into account will be published elsewhere.

As the distance between the particles becomes larger, fewer plasmons are excited. The SCS becomes less turbulent and tends to the SCS of the single particle. As one can imagine, this is already the case for quite small distances, if the illumination direction is perpendicular to the coupled particles. i.e. they are not in the geometrical shadow. Figure 7 shows the SCS divided by two for the two particles under perpendicular illumination at a distance of 75 nm, compared with the SCS of the single particle. They are qualitatively as well as quantitatively comparable. By calculating the field distributions around the particle one can state that the same plasmons are excited as in the single particle case. They can be treated as decoupled.

4 Conclusions

In this article we have applied the Boundary Element Method to the interaction of light with resonant metallic nano particles. A formulation for the BEM has been presented, which makes it possible to treat coupled particle systems. We have determined the SCS and corresponding near-field amplitude distributions of circular and elliptical cylinders. The elliptical structures have resonances in accordance with their geometrical axis and illuminating the object at an angle to either axis will excite both resonances with an appropriately lower amplitude. We have treated the problem of coupled particles as they appear in SERS measurements. If particles are close, various surface plasmons are excited. With increasing distance these turbulences will decrease and from a certain distance, which has been determined for two coupled circular silver cylinders perpendicular to the illumination direction, the system can be regarded as decoupled. SCS and amplitude near-field distributions equal then those of a single particle.

The research was supported by the European Union within the framework of the Future and Emerging Technologies-SLAM program.

References

[1] M. Scharte, R. Porath, T. Ohms, M. Aeschlimann, J. R. Krenn, H. Ditlbacher, F. R. Aussenegg and A. Liebisch, "Do Mie plamons have a longer lifetime on resonance than off resonance?," Appl. Phys. B **73,** 305–310 (2001).

[2] D. Wang, S. Guo, H. Ren and S. Yin, "Optical characteristics of silver-doped polarizing glass," Opt. Lett. **27,** 992–994 (2002).

[3] C. F. Bohren and D.R. Huffmann, *Absorption and Scattering of Light by Small Particles* (Wiley, New York, 1983).

[4] E. Moreno, D. E. Erni, C. Hafner and R. Vahldieck, "Multiple Mulitpole method with automatic multipole setting applied to the simulation of surface plasmons in metallic nanostructures," J. Opt. Soc. Am. A **19,** 101–111 (2002).

[5] W. H. Yang, G. C. Schatz and R. P. Van Duyne, "Discrete dipole approximation for calculating extinction and Raman intensities for small particles with arbitary shape," J. Chem. Phys. **103,** 869–875 (1995).

[6] J. P. Kottmann and O. J. F. Martin, "Accurate Solution of the Volume Integral Equation for High-Permittivity Scatterers," IEEE Trans. Antennas Propag. **48,** 1719–1726 (2000).

[7] J. P. Kottmann and O. J. F. Martin, "Influence of the cross section and the permittivity on the plasmon-resonance spectrum of silver nanowires," Appl. Phys. B **73,** 299–304 (2001).

[8] L. C. Wrobel and M. Aliabadi, *The Boundary Element Method* (Wiley, New York, 2002).

[9] J. M. Bendickson, E. Glytsis and T. K. Gaylord, "Focusing diffractive cylindrical mirrors: rigorous evaluation of various design methods," J. Opt. Soc. Am. A **18,** 1487–1494 (2001).

[10] M. K. Choi, "Numerical calculation of light scattering from a layered sphere by the boundary-element method," J. Opt. Soc. Am. A **18,** 577–583 (2001).

[11] J. Liu, B.-Y. Gu, B.-Z. Dong and G.-Z. Yang, "Interference effect of dual diffractive cylindrical microlenses analyzed by rigorous electromagnetic theory," J. Opt. Soc. Am. A **18,** 526–536 (2001).

[12] D. W. Prather, M. S. Mirotznik and J. N. Mait, "Boundary integral method applied to the analysis of diffractive optical elements," J. Opt. Soc. Am. A **14,** 34–43 (1997).

[13] D. W. Prather, J. N. Mait, M. S. Mirotznik and J. P. Collins, "Vector-based synthesis of finite aperiodic subwavelength diffractive optical elements," J. Opt. Soc. Am. A **15,** 1599–1607 (1998).

[14] M. Born and E. Wolf, *Principles of Optics* (Cambridge University Press, 1999).

[15] P. B. Johnson and R. W. Christy, "Optical Constants of the Nobel Metals," Phys. Rev. B **6,** 4370–4379 (1972).

[16] M. Moskovits, "Surface-enhanced spectroscopy," Rev. Mod. Phys. **57,** 783–825 (1985).

[17] H. Xu, E. J. Bjernfeld, M. Käll and L. Börjesen, "Spectroscopy of Single Hemoglobin Molecules by Surface Enhanced Raman Scattering," Phys. Rev. Lett. **83,** 4357–4360 (1999).

Analyzing the scattering properties of coupled metallic nano-particles

Carsten Rockstuhl, Martin Guy Salt, Hans Peter Herzig

University of Neuchâtel, Institute of Microtechnology,
Rue A.-L. Breguet 2, CH-2000 Neuchâtel, Switzerland

October 15, 2004

Abstract

We apply the Boundary Element Method to the analysis of the plasmon response of systems that consist of coupled metallic nano scatterers. For systems that are made of two or more objects, the response depends strongly on the individual particle behavior, as well as on the separation distance and arrangement of the particles relative to the illumination direction. By analyzing the behavior of these systems, we determine the smallest interaction distance from which the particles can be considered as decoupled. We discriminate the two cases in which a particle system consists of scatterers with the same and different resonance wavelengths.

OSICS codes: 050.1960, 240.6680.

1 Introduction

By illuminating metallic nano- and micro-particles at a well-defined wavelength, it is possible to excite a collective oscillation of the electrons in the material, which is in resonance with the driven wave-field[1]. These plasmon resonances appear in the blue and green part of the spectrum for metallic materials such as gold and silver[2]. If a plasmon is excited, a large scattering cross section (SCS) and a strong near-field amplitude can be observed. The visual result of this effect has been known for centuries, where artisans incorporated metallic particles into ceramics to give them beautiful iridescent reflections[3]. Except for the special case of a circular cylinder or a sphere where Mie-theory can be applied, the exact wavelength for which the plasmon resonance is excited cannot be determined analytically. The condition for plasmon excitation for a circular cylinder is a real part of the dielectric constant that equals -1. In the case of a sphere the condition is a real part of the dielectric constant of -2 assuming air as the ambient media[4]. For certain wavelengths silver and gold fulfill this condition to a good approximation. The remaining imaginary part in the dielectric constant will principally lead to a damping, broadening and a slight red shift in the SCS. For objects that deviate from this simple geometry, such a quasi-analytical condition can no longer be given[5]. Consequently various efforts have been made to analyze the scattering properties and to determine rigorously the plasmon response of arbitrarily shaped micro-particles by using a broad range of different numerical techniques. Among others, the Discrete Dipole Approximation (DDA)[6], the Greens Dyadic Function (GDF)[7], and the Generalized Multiple Multipole Method (MMP)[8] have been successfully applied. We will use the Boundary Element Method (BEM)[9] for the numerical treatment of resonant metallic nano-particles and we will concentrate on the influence of the plasmon response if the system consists of two or more scatterers for small separation distances. The method is chosen because it formulates the problem as a surface one, which reduces the computational effort in comparison with other methods. The method is a direct numerical solution of the Boundary Integral Equation that is derived from Maxwell's equations[10]. Except for a discretized sampling of the surface of the particles no approximations are done and especially the field retardation within the particles is fully taken into account. The basic equations of the method and all the necessary parameters that describe the problem are given in appendix A.

Such systems of particles in close proximity can play a major role in an application like Surface Enhanced Raman Spectroscopy (SERS)[11] for the detection of fluorescent molecules. Ideally the molecules under consideration are placed directly between two metallic particles. By choosing proper system parameters, a surface plasmon is excited. The surface plasmon will lead to a large SCS and a high near-field amplitude. The enhancement of the amplitude can be dramatic, with the point of the highest near-field directly between the two particles[12]. If the fluorescent molecule is positioned directly at this "hot spot" and exposed to the large near-field, its fluorescent signal will be likewise dramatically enhanced. The enhancement even allows single molecule detection.

Another interesting application for coupled metallic nano-particles is their usage for light guidance on a length scale significantly below the diffraction limit[13, 14, 15]. The basic idea is to arrange the particles in a chain or a form appropriate to fulfil an optical function like bending or beam splitting[16]. The first particle in the chain is excited at a resonant wavelength. The particle is coupled evanescently with the subsequent one and energy is transferred between the particles and consequently light guidance is possible. The process is highly efficient because the near-field is resonantly enhanced in the vicinity of the particles due to the plasmon excitation. Such a coupling between particles has already been proven experimentally by using a SNOM tip as a spatially highly confined light source[17].

For an experimental investigation of the properties of coupled particles in a controlled manner, structures written by an e-beam[18] and suspended particles centrifuged on glass were used[19]. It was shown experimentally that the SCS will be red-shifted and broadened if the separation between the particles is reduced.

The case of two coupled circular cylinders has been analyzed theoretically using GDF in the past by Kottmann et al [12, 20]. Generally, they found that if particles are in close proximity, the response of the entire system is broadened and red-shifted. Coupling effects will become dominant and the two objects will show a characteristic scattering response that deviates strongly from the response of a single object. If the particles are in very close proximity, a second well distinguishable resonance appears at higher wavelengths. By increasing the separation distance, the pronounced interaction of the particles will be reduced and above a certain distance the response of the coupled particles will converge to the response of the single particle system. They can be treated as decoupled.

We focus this study on the analysis of systems that consist of two or more coupled cylinders with a circular or elliptical geometrical cross section, which is done to the best of the authors knowledge for the first time. We will determine the distance from which such a pair of particles can be treated as decoupled. In theory, no sharp change between coupled and decoupled particles exists. As the criteria for the discrimination between coupled and decoupled particles, we firstly require the effective suppression of the excitation of plasmons that are associated with the coupled geometry and which have no equivalent in the spectrum of each of the single particles involved in the system. This is probably the most import criterion, if e.g. the metallic nano-particles are used for an optical data storage system as proposed by Ditlbacher et al.[21], in which the spectrum of the reflected light within a diffraction limited spot size is analyzed. In this spot size particles with different geometries are placed and analyzing the plasmon peaks in the spectrum reveals the existence of the particles. For such a system it is of vital importance that no additional peaks appear, as they would indicate the presence of different particles, which don't actually exist in the real system. As a second weaker criteria we have used the accordance of the plasmon wavelengths in the coupled system with its counterpart in each of the single particle systems.

In the second section we will apply the BEM to a system with two silver circular or elliptical cylinders. For the prediction of the behavior, the dielectric constant experimentally determined and published by Johnson and Christy[22] has been used. The elliptical cylinders will support two different resonance wavelengths by illuminating them along the two principal axes. The resonance wavelengths are principally determined by the axis ratio. By rotating one of the elliptical cylinders by an angle of 90^o relative to the other, the two objects are resonantly detuned. For the same illumination direction, their resonance wavelength is a different one. We will show that the interaction of these two particles is less pronounced even at small separation distances. Finally we will analyze the SCS of a larger number of elliptical particles, which have different resonance wavelengths.

2 Analysis of two objects with the same resonance wavelength

2.1 Circular cylinder

For the investigation of the principal behavior we have analyzed the scattering response of two circular cylinders ($r = 25\ nm$) for various separation distances. As a general remark, all the separation lengths that are given in the text are the surface-surface separations of the particles. A plasmon can only be excited if the light is TM-polarized, meaning that the magnetic field vector oscillates parallel to the cylinder. The generation of a surface charge requires an electric field normal to the surface. As in the two-dimensional geometry the magnetic field has only a single component for TM polarization, we show for simplicity in all the corresponding figures the near-field amplitude of the magnetic field to visualize the excited plasmons.
For a clear relation between the arrangement of the particles and the illumination direction, we will give the angle of illumination. This angle is defined between the normal of the center-center line between the particles and the wave-vector of the illuminating beam. An illumination direction of 0^o means that the normal to the center-center line is parallel to the direction of the incoming wave. 90^o means that the normal is perpendicular to the wave-vector of the illuminating beam. In the figures, which show the amplitude distribution of the magnetic field in the near-field of the particles, we have added an arrow that shows the direction of the wave-vector of the illuminating beam.
Figure 1 shows the SCS of two circular cylinders at a separation distance of 5 nm for three different illumination directions. The resonance condition for a circular cylinder is a real part in the dielectric constant of -1. Such a condition is approximately fulfilled for silver at 340 nm. Independent of the illumination direction we have a local maximum in the SCS at approximately this resonance wavelength, which is the dipole excitation wavelength for the single cylinder. Additionally, a second plasmon is excited at a wavelength that is red-shifted relative to the dipole wavelength (approximately 380 nm). These resonances are clearly attributed to the coupling effect of the neighboring particles. The interaction is less pronounced for the illumination direction at 90^o. In such a configuration the field inside each of the two particles does not oscillate in phase due to the retardation of the incoming wave and coupling between the particles is less pronounced than in the case

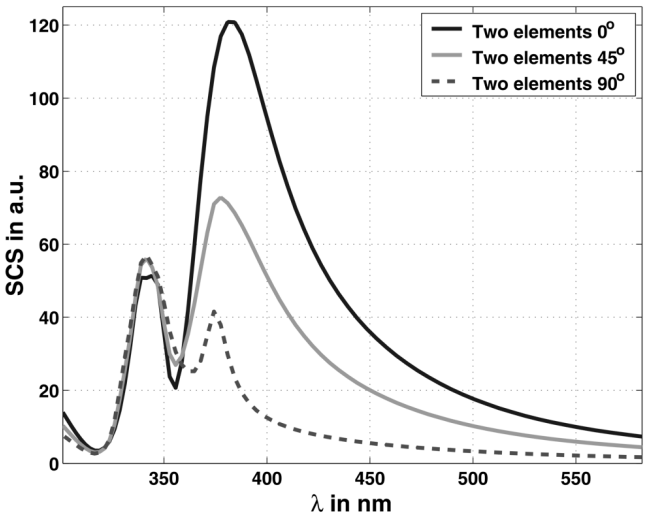

Figure 1: SCS of two circular cylinders with $r = 25\ nm$ at a separation distance of $d = 5\ nm$.

of an illumination at 0^o. The wave vector for this illumination direction is perpendicular to the axis joining the two particles and the scattered fields inside the particles oscillate in phase[12]. This plasmon is the fundamental mode of the two-particle configuration. The field amplitude has its highest value directly between the two particles for this plasmon. In Fig. 2 we show the field distributions of the excited plasmons for an illumination direction of 90^o.

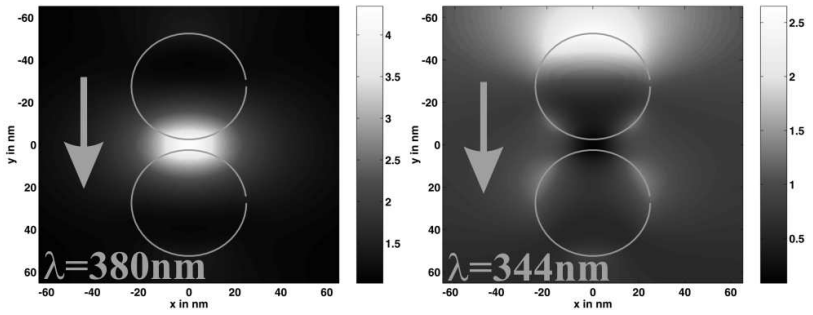

Figure 2: Near-field amplitude of the magnetic field for plasmons excited at two circular cylinders with $r = 25\ nm$ at a separation distance of $d = 5\ nm$.

By increasing the separation, the interaction is reduced. Figure 3 shows the

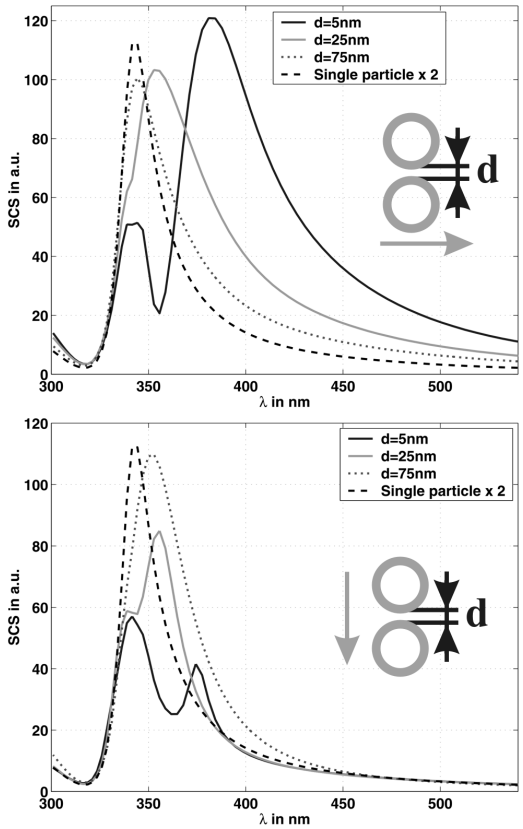

Figure 3: SCS of two circular cylinders with $r = 25\ nm$ at different separation distances for an illumination direction of 0^o in the upper figure and of 90^o in the lower figure.

SCS at a separation of 5 nm, 25 nm and 75 nm in comparison with the SCS of a single particle (multiplied by a factor of two) for two different illumination directions (they are indicated in the inset of the figure). It can be clearly seen that both SCS's at a separation distance of 75 nm are comparable to the SCS of the single particle. The particles can be treated as decoupled from this separation distance. The remaining effect on the SCS is a broadening and a marginal damping. Figure 4 shows the near-field amplitude at the maximum of the SCS for an illumination direction of 0^o. This maximum in the SCS correlates to the excitation of a dipole and the two local maxima in the amplitude can be seen. Nonetheless, an influence of the neighboring scatterer still remains, which results in a slight distortion of the field from

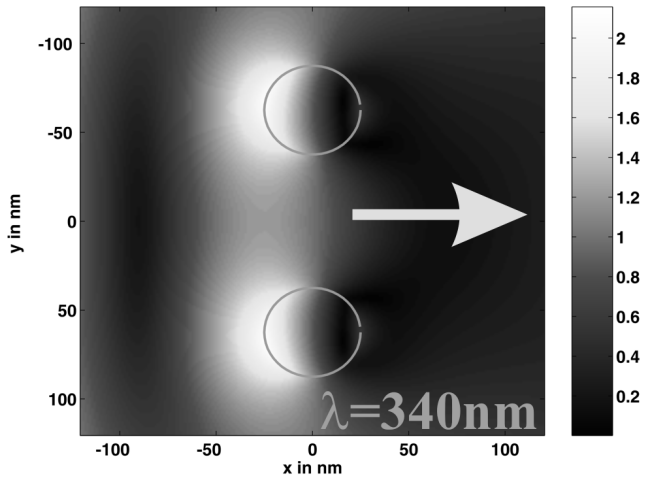

Figure 4: Near-field amplitude of the magnetic field for a plasmon excited at two circular cylinders with $r = 25\ nm$ at a separation distance of $d = 75\ nm$.

the axis-symmetric distribution across the particle.

2.2 Elliptical cylinder

Similar investigations can be carried out for elliptical cylinders. These particles will have a resonance at two different wavelengths, which for small particles (radius much smaller than the wavelength) depends only on the axis ratio. Illuminating the particles under an angle relative to the principal axis will excite both plasmons but with a somewhat lower strength[9]. The strength is related to the projection of the incoming wave front on the two principal axes. If the two elliptical cylinders in the system have the same alignment relative to the illumination direction, it is assumed that the interaction is likewise pronounced as in the case of the circular cylinders, because the resonance wavelength is the same for the two elliptical objects. Figure 5 shows the SCS of two elliptical particles ($r_1 = 10\ nm, r_2 = 20\ nm$) for the illumination directions of 0^o along the major axis and 90^o, which corresponds to an illumination direction along the minor axis, at three different separation distances (5 nm, 10 nm and 80 nm). The geometrical arrangement is shown in the inset of Fig. 5. Please note that the y-scale is now a logarithmic one. For a separation distance of 5 nm two well-pronounced maxima exist for an illumination direction of 0^o. By comparing the response of the coupled sys-

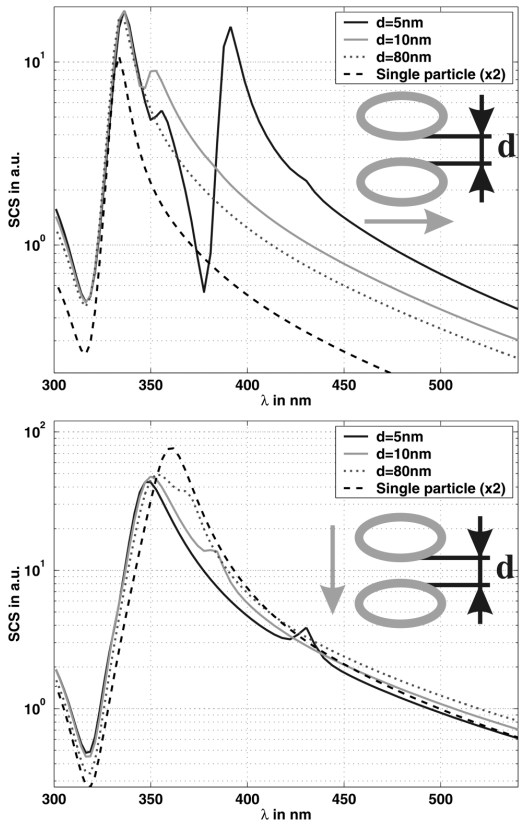

Figure 5: SCS of two elliptical cylinders with $r_1 = 10\ nm$ and $r_2 = 20\ nm$ at different separation distances for an illumination direction of 0^o in the upper figure and of 90^o in the lower figure.

tem with the single particle it becomes obvious that the plasmon at 335 nm is related to the wavelength for which the dipole is excited in the single elliptical particle by illuminating such a particle along its major axis. When a second particle is present in the set-up, this wavelength is slightly red-shifted relative to the resonance wavelength of the single particle. Additionally, the second plasmon is excited at a higher wavelength of 390 nm if the particles are in a close vicinity. Increasing the separation distance, the second plasmon decreases strongly and becomes blue shifted. In such a scattering configuration the fields inside the particles oscillate in phase and the interaction is pronounced in a similar way to the circular cylinders. On the other hand, choosing the illumination along the axis joining the two particles, the inter-

action becomes much weaker. A strong plasmon is excited around 360 nm, corresponding to the plasmon of the single particle upon illumination along the short axis. For a separation distance of 5 nm an additional plasmon is weakly excited at 430 nm. By increasing the distance between the particles, this resonance wavelength is shifted towards the resonance wavelength of the single particle. Because its strength is small compared to the strength of the dipole excitation, the dipole contribution dominates the entire SCS and the signature of the second plasmon vanishes.
By comparing the strength of the fundamental plasmon, it can be seen that this strength is always enhanced at an illumination direction at 0^o due to the in-phase oscillation of the field inside the particles. The dipole strength for an illumination direction of 90^o is always lower than the strength of the single particle.
For both illumination directions the problem can be treated as decoupled at a separation distance of 80 nm.

3 Analysis of two objects with different resonance wavelengths

For the analysis of particles with different resonance wavelengths, we have used elliptical particles with different axis ratios. The axis ratio is given by the radius of the particle that is perpendicular to the wave-vector of the illuminating beam divided by the radius of the particle that is parallel to the wave-vector.
Figure 6 shows the SCS of two elliptical particles, which have again a radius of $r_1 = 10\ nm$ for the minor axis and $r_2 = 20\ nm$ for the major axis. They have a relative rotation of their axes of 90^o such that by illuminating the particles under an angle of 0^o, one of the particles has a resonance wavelength at 360 nm (axis ratio 2/1) and the other particle has a resonance wavelength at 335 nm (axis ratio 1/2). The SCS is shown for three different separation distances (5 nm, 10 nm and 35 nm) and again for two illumination directions. In addition, the sum of the SCS for the two principal axes is shown in the figures. The exact geometry is shown in the inset of the figure. It can be seen that even for small separation no significant additional plasmon is excited. The only remaining influence of the presence of a neighboring particle on the SCS is a red shift of the entire SCS of about 20 nm for a separation distance

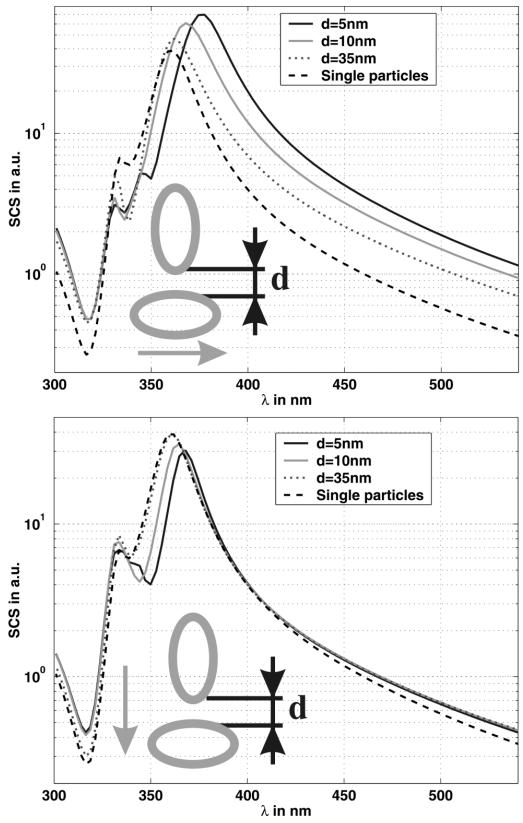

Figure 6: SCS of two elliptical cylinders with $r_1 = 10\ nm$ and $r_2 = 20\ nm$, which have a relative rotation of 90^o, at different separations for an illumination direction of 0^o in the upper and of 90^o in the lower figure.

of 5 nm. Additionally, the plasmon response is damped upon illuminating the structures parallel to the two particles and enhanced if the particles are perpendicular to the illumination direction, due to the reasons outlined in the last section. The plasmon resonance is broader for an illumination direction of 0^o. This is the only remaining signature of a perturbation. By increasing the separation distance between the particles both effects are reduced in the characteristic strength and already at a separation of 35 nm the SCS of the coupled system is comparable to the SCS of the two single systems. For an explanation of the behavior Fig. 7 shows the near-field distribution of the coupled particles at the two resonance wavelengths (334 nm and 362 nm). Obviously, the particles behave nearly transparently at wavelengths for which

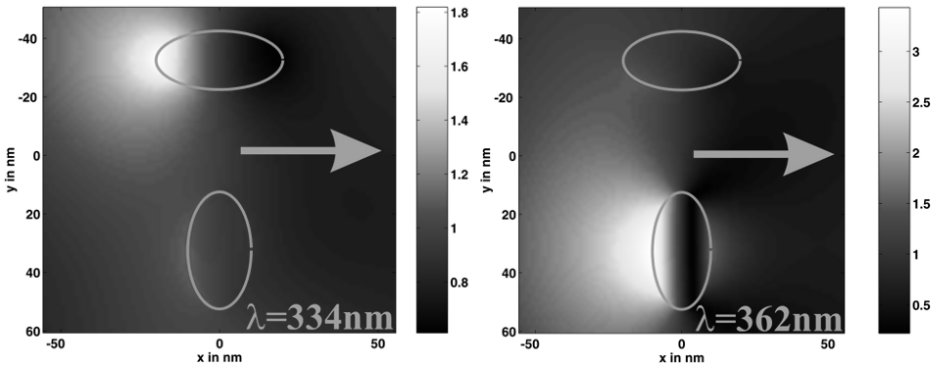

Figure 7: Near-field amplitude of the magnetic field for plasmons excited at two elliptical cylinders with $r_1 = 10\ nm$ and $r_1 = 20\ nm$ at a separation distance of $d = 35\ nm$ for two different wavelengths.

they are not resonant. They will not produce a significant portion of scattered light that could perturb the second particle. As a consequence, this particle can act as if it were alone and the SCS will converge to the SCS of the two single particles even for small separation distances. They are effectively resonantly detuned.

4 Analysis of various objects with different resonance wavelengths

The possibility of tuning the resonance wavelength of elliptical particles allows the calculation of a set of particles with plasmons that can cover a broad range of wavelengths. Additionally, changing the absolute size of the particles while keeping the axis ratio constant can change the scattering strength of the particles in a controlled manner. For small particles within the electrostatic approximation the scattering strength will scale with the fourth power of the radius. For larger particles the phase retardation of the field inside the particle cannot be neglected and the scattering strength will saturate. In addition, the wavelength for which the plasmon resonance is excited will shift to a higher wavelength and the full width at half maximum of the SCS will be increased. By using these properties it is possible to design some particles such that their SCS becomes clearly distinguishable in the spectral domain and the strength of the scattering signal is approximately the same

for all the particles. The SCS for a set of nine silver particles that have different resonance wavelengths and approximately the same strength is shown in Fig. 8. For completeness Table 1 shows the exact radii of each particle. It

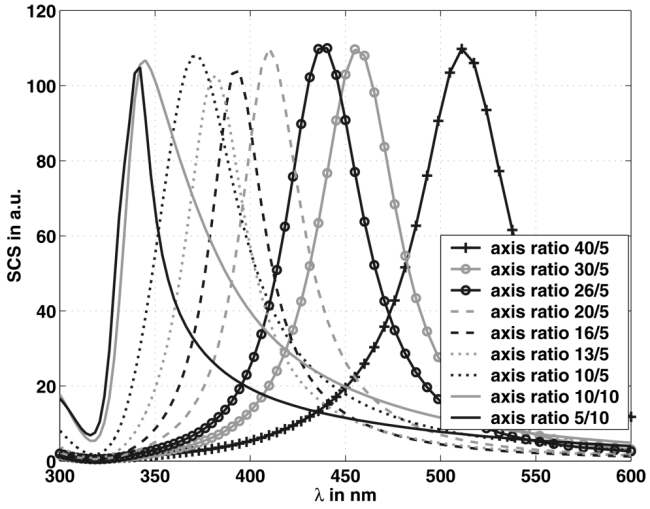

Figure 8: SCS of nine elliptical cylinders as a function of the axis ratio.

is possible to tune the resonance wavelength over a range of approximately 200 nm.

Table 1: Radii of the analyzed particles

axis ratio	1/2	1	2/1	13/5	16/5	20/5	26/5	30/5	40/5
r_1 in nm	35	41	39.0	33.8	32.3	34.0	36.3	36.5	40
r_2 in nm	70	41	19.5	13.0	10.1	8.5	7.0	6.1	5

For the analysis of incoherent superposition we use only four of the particles because each element should show a clear spectral signature. This incoherent superpositioned SCS of the four particles is shown in Fig. 9. The particles that were used in the calculation had an axis ratio of 40/5, 30/5, 20/5 and 5/10. The different elliptical particles in the inset of the figure show the geometry of the elliptical particle that is associated with the corresponding plasmon wavelength.
Figure 10 shows the SCS of the four coupled particles as a function of the

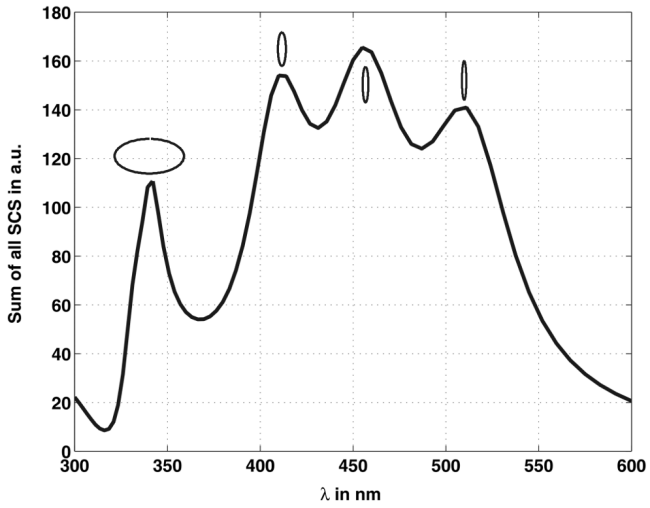

Figure 9: Incoherent superposition of the SCS of four elliptical cylinders.

surface-surface distance for an illumination direction perpendicular to the particle chain. The arrangement of the particles was 40/5, 5/10, 30/5 and 20/5. Similar responses have been obtained with other arrangements.
It can be seen that as long as the particles have a large separation (70 nm) all the maxima in the SCS are well defined and each of the four particles clearly reveals its existence by leaving a signature in the common SCS. By reducing the distance between the particles, the entire SCS becomes red-shifted and slightly damped. Nevertheless, at a distance of 35 nm all particles can be discriminated in the SCS. An additional decrease of the particle distance will further red shift the spectra. This is especially well pronounced for the particles with a higher axis ratio. The coupling effects among neighboring particles will play a dominant role and the spectral peaks are nor longer precisely resolved. We conclude that the smallest interaction distance from which coupled particle systems can be treated as decoupled is about 35 nm for systems where the plasmon resonance wavelengths are different.

5 Conclusions

In the present work we have applied the Boundary Element Method to analyze the influence on the SCS of metallic nano-particles when they are perturbed by additional particles.

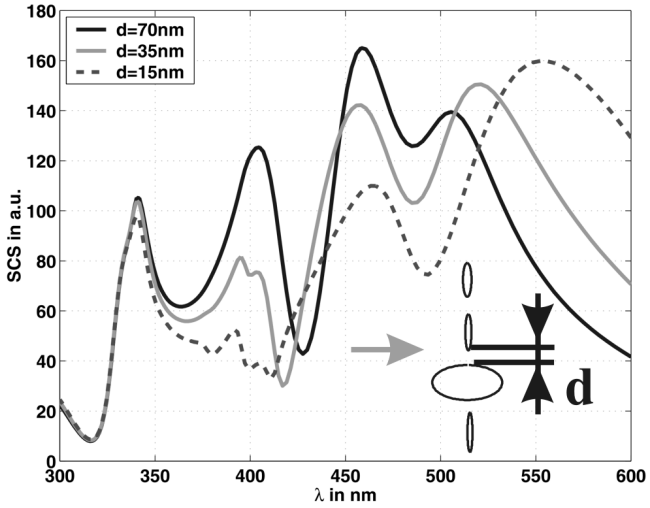

Figure 10: SCS for four coupled silver elliptical cylinders for different separation distances.

Generally, the coupling effects are stronger if the particles are arranged in a plane which is perpendicular to the illumination direction, because in such a geometry the scattered field emanating from the particles is in phase, which leads to an enhancement of the interaction. By contrast, the effects are less pronounced if the particles are arranged parallel to the illumination direction, because the oscillating scattered fields from the particles are out of phase.
For all particles that are in close proximity, an additional plasmon resonance is excited, which has no equivalent in the single particle case. By increasing the distance between the particles the interaction is less pronounced, the strength of this additional plasmon is reduced and beyond a certain separation distance the particles can be treated as decoupled. This separation distance depends strongly on the plasmon wavelength for the two particles that are involved. If the particles have their resonance at the same wavelength, the particles have to be separated by at least 75 nm.
If the particles are resonantly detuned, which means that their plasmon resonances are at different wavelengths, the interaction is less pronounced. In this case the only alteration that can be observed in the resulting SCS is a broadening and a slight red-shift of the SCS. Both are more pronounced for an illumination direction perpendicular to the particle arrangement.
We have shown that the resonance wavelength for elliptical particle is tunable

over a broad wavelength range just by changing the axis ratio. The strength of the scattering signal can be tuned by changing the overall size of the geometrical cross section. A set of nine elliptical cylinders was presented which have a clearly distinguishable resonance wavelengths and approximately the same scattering strength. The collective response of four of these elliptical cylinders was analyzed again for different particle distances. We found that a separation of 35 nm is necessary for the treatment of the system as an uncoupled one, which means that all the particles can be spectrally resolved.
This research was supported by the European Union within the framework of the Future and Emerging Technologies-SLAM program under grant No. IST-2000-26479.
Carsten Rockstuhl can be reached by e-mail at carsten.rockstuhl@unine.ch.

Appendix A

We assume that the system consists of M homogenous scatterers with a dielectric constant ϵ_{I_m}. The objects are described by their contour C_m and their normal $\hat{n}_{I_m}$ and they are illuminated with an arbitrary wave-field $u_0^{inc}(\rho)$ from a region with a homogenous permittivity ϵ_0. ρ is an observation point in the x-y-plane. If the field is TE-polarized, $u(\rho)$ denotes the $E_z(\rho)$ component of the electromagnetic field and $u(\rho)$ denotes the $H_z(\rho)$ component if the field is TM-polarized. The total field $u^{tot}(\rho)$ can be written as a superposition of the illuminating field $u_0^{inc}(\rho)$ and the scattered field from each of the particles $u_m^{sc}(\rho)$. The normal derivatives of the different fields with respect to the boundary are denoted by $v_0^{inc}(\rho)$, $v_m^{sc}(\rho)$ and $v^{tot}(\rho)$. It is assumed that the materials are non-magnetic, i.e. the relative permeability is $\mu_r = 1$.
In the interior region of each particle the total field is a solution of a homogenous wave equation, in the exterior region the total field is a solution of an inhomogeneous wave equation. The boundary integral equations can be derived by applying Green's Second Identity [10] to these Helmholtz equations. For a particle m they read as

$$\begin{aligned} 0 \;=\; u_m^{sc}\,(\rho_m) + \int_{C_m} \Bigg\{ u_m^{sc}\,(\rho'_m) \frac{\partial G_{Im}(\rho_m, \rho'_m)}{\partial \hat{n}_{I_m}} \\ - p_{I_m} G_{Im}(\rho_m, \rho'_m) v_m^{sc}\,(\rho'_m) \Bigg\}\, dl' \end{aligned}$$

$$
\begin{aligned}
+ \quad & u_m^{inc}(\rho) + \int_{C_m} \left\{ u_m^{inc}(\rho'_m) \frac{\partial G_{Im}(\rho_m, \rho'_m)}{\partial \hat{n}_{I_m}} \right. \\
& \left. - p_{I_m} G_{I_m}(\rho_m, \rho'_m) v_m^{inc}(\rho'_m) \right\} dl' \quad \text{for } \rho \in I \\
0 \quad = \quad & u_m^{sc}(\rho_m) + \int_{C_m} \left\{ u_m^{sc}(\rho') \frac{\partial G_O(\rho_m, \rho'_m)}{\partial \hat{n}_{O_m}} \right. \\
& \left. + p_O G_O(\rho_m, \rho'_m) v_m^{sc}(\rho'_m) \right\} dl' \quad \text{for } \rho \in O. \qquad (1)
\end{aligned}
$$

$G_{I_m}(\rho_m, \rho'_m)$ and $G_O(\rho_m, \rho'_m)$ are Green's functions related to the field inside and outside of the objects. $p_{I_m,\,O}$ is a parameter that depends on the polarization and it equals unity if the field is TE-polarized and $\epsilon_{I_m,\,O}$ if the field is TM-polarized. The incident wave field on particle m, $u_m^{inc}(\rho)$, is a superposition of the illuminating wave field $u_0^{inc}(\rho_m)$ and the scattered contribution from all the other particles the system consists of. It reads as

$$
\begin{aligned}
u_m^{inc}(\rho_m) = u_0^{inc}(\rho_m) + \sum_{n \neq m} \int_{C_n} & \left\{ u_n^{sc}(\rho'_n) \frac{\partial G_O(\rho_m, \rho'_n)}{\partial \hat{n}_{I_n}} \right. \\
& \left. - p_O G_O(\rho_m, \rho'_n) v_n^{sc}(\rho'_n) \right\} dl'. \qquad (2)
\end{aligned}
$$

By expanding the field and its derivative normal to the surface for each of the particles in terms of linear interpolation functions, a system of linear equations can be derived that is solved by standard matrix techniques for the unknown field components of all the particles in parallel[9].
Once the scattered field and its derivative along the surface are known, the entire field outside the particles can be calculated using an equation similar to equation 2.

References

[1] M. Scharte, R. Porath, T. Ohms, M. Aeschlimann, J. R. Krenn, H. Ditlbacher, F. R. Aussenegg, and A. Liebisch, "Do Mie plamons have a longer lifetime on resonance than off resonance?", Appl. Phys. B **73**, 305–310 (2001).

[2] C. Sönnichsen, T. Franzl, T. Wilk, G. von Plessen, and J. Feldmann, "Plasmon resonances in large noble-metal clusters", New J Phys **4**, 93.1–93.8 (2002).

[3] G. Padeletti and P. Fermo, "How the masters in Umbria, Italy, generated and used nanoparticles in art fabrication during the Renaissance period ", Appl. Phys. A **76**, 515–525 (2003).

[4] C. F. Bohren and D.R. Huffmann, *Absorption and Scattering of Light by Small Particles* (Wiley, New York, 1983).

[5] J. P. Kottmann and O. J. F. Martin, "Influence of the cross section and the permittivity on the plasmon-resonance spectrum of silver nanowires," Appl. Phys. B **73,** 299–304 (2001).

[6] W. H. Yang, G. C. Schatz, and R. P. Van Duyne, "Discrete dipole approximation for calculating extinction and Raman intensities for small particles with arbitary shape," J. Chem. Phys. **103,** 869–875 (1995).

[7] J. P. Kottmann and O. J. F. Martin, "Accurate Solution of the Volume Integral Equation for High-Permittivity Scatterers," IEEE Trans. Antennas Propag. **48,** 1719–1726 (2000).

[8] E. Moreno, D. E. Erni, C. Hafner, and R. Vahldieck, "Multiple Multipole method with automatic multipole setting applied to the simulation of surface plasmons in metallic nanostructures," J. Opt. Soc. Am. A **19,** 101–111 (2002).

[9] C. Rockstuhl, M. Salt, and H. P. Herzig. "Application of the boundary-element method to the interaction of light with single and coupled metallic nanoparticles", J. Opt. Soc. Am. A **20**, 1969–1973 (2003).

[10] D. W. Prather, M. S. Mirotznik and J. N. Mait. "Boundary integral method applied to the analysis of diffractive optical elements", J. Opt. Soc. Am. A, **14**, 34–43 (1997).

[11] M. Moskovits, "Surface-enhanced spectroscopy," Rev. Mod. Phys. **57,** 783–825 (1985).

[12] J.P. Kottmann and O.J.F. Martin, "Retardation-induced plasmon resonances in coupled nanoparticles", Opt. Lett. **26,** 1096–1098 (2001).

[13] J. R. Krenn, J. C. Weeber, A. Dereux, E. Bourillot, J. P. Goudonnet, B. Schider, A. Leitner, F. R. Aussenegg, and C. Girard, "Direct observation of localized surface plasmon coupling", Phys. Rev. B **60**, 5029–5033 (1999).

[14] S. A. Maier, M. L. Brongersma, P. G. Kik, S. Meltzer, A. A.G. Requicha, and H. A. Atwater, "Plasmonics - a route to nanoscale optical devices", Adv. Mater. **13,** 1501–1505 (2001).

[15] M. Quinten, A. Leitner, J. R. Krenn, and F. R. Aussenegg, "Electromagnetic energytransport via linear chains of silver nanoparticles", Opt. Lett. **23,** 1331–1333 (1998).

[16] M. L. Brongersma , J. W. Hartman, and H. A. Atwater, "Electromagnetic Energy Transfer And Switching In Nanoparticle Chain Arrays Below The Diffraction Limit", Phys. Rev. B **62**, R16356–R16359 (2000).

[17] S. A. Maier, P. G. Kik, H. A. Atwater, S. Meltzer, E. Harel, B. E. Koel, and A. A.G. Requicha, "Local detection of electromagnetic energy transport below the diffraction limit in metal nanoparticle plasmon waveguides", Nature Materials **2**, 229–232 (2003).

[18] W. Rechberger, A. Hohenau, A. Leitner, J. R. Krenn, B. Lamprecht, and F. R. Aussenegg, "Optical properties of two interacting gold nanoparticles", Opt. Commun. **220,** 137–141 (2003).

[19] H. Tamaru, H. Kuwata, H. T. Miyazaki, and K. Miyano, "Resonant light scattering from individual Ag nanoparticles and particle pairs", Appl. Phys. Lett. **80,** 1826–1828 (2002).

[20] J.P. Kottmann and O.J.F. Martin, "Plasmon resonant coupling in metallic nanowires", Opt. Express **8,** 655–663 (2001).

[21] H. Ditlbacher, J. R. Krenn, B. Lamprecht, A. Leitner and F. R. Aussenegg, "Spectrally coded optical data storage by metal nanoparticles", Opt. Lett. **25,** 563–565 (2000).

[22] P. B. Johnson and R. W. Christy, "Optical constants of the noble metals", Phys. Rev. B **6**, 4370–4379 (1972).

Analyzing the phonon polariton response of Silicon Carbide micro- and nano-particles using the Boundary Element Method

Carsten Rockstuhl, Martin Guy Salt, Hans Peter Herzig

University of Neuchâtel, Institute of Microtechnology,
Rue A.-L. Breguet 2, CH-2000 Neuchâtel, Switzerland

October 15, 2004

Abstract

We investigate the small particle phonon polariton response of several microstructures that are made of Silicon Carbide. Phonon polaritons can be excited in a wavelength region between 10 μm and 12 μm. Simple structures such as elliptical cylinders support phonon polaritons at two wavelengths, which depend on the axis ratio of the particle. In particles with a more irregular shape such as rectangular or triangular cylinders up to five phonon polaritons can be excited. By comparing the strength of phonon polariton excitation with the similar effect of the plasmon polariton excitation in metallic nano particles, it is found that the excitation of phonon polaritons is more efficient. This behavior is attributed to the lower imaginary part of the dielectric constant of Silicon Carbide.

OSICS codes: 050.1940, 260.3060, 260.5740

1 Introduction

Silicon Carbide (SiC) is a material that has recently attracted interest due to its applications as a wide-bandgap semiconductor, used for high temperature and high power microelectronics. For example it can be applied in a Schottky-contact[1] or as the emitting material in a blue laser diode[2]. Another interesting property of the material is its special dielectric constant in the far-infrared region of the spectrum between 10 μm and 12 μm[3, 4]. In this spectral region the real part has a negative value between -1 and -10 and the imaginary part is very small. This dielectric function is comparable to that of metals such as silver in the blue and gold in the green parts of the spectrum[5]. Illuminating small particles made of these metallic materials at the appropriate wavelengths will excite a surface plasmon, which is a collective oscillation of the free electrons[6]. Nevertheless the physical origin is hidden behind the dielectric constant and the physical interpretation of the behavior is based on arguments from solid-state physics. The frequency of the driving illumination wave-field equals the oscillating frequency of the free electrons in the metallic bulk material and the movement of the electrons becomes resonant. In SiC the free electrons play only a minor role, but the frequency of the illuminating wave-field might instead match the resonance frequency of the Si- and C-sublattices[7] and a small particle phonon polariton is thus excited. This excitation leads to an enhanced field amplitude in the vicinity of the particle (near-field) and to a strong scattering cross section (SCS) at the resonance wavelength. The first investigations of the resonant scattering behavior in the infrared region of the spectrum for SiC were made for the detection of the mass outflow of carbon stars and meteorites[8]. In addition this unique property of SiC found an interesting application as a coherent, directed emitter in the corresponding spectral region[9, 10].
Experimental investigations of excited phonon polaritons at nano- and micrometer sized SiC particles attracted the interest of some researchers. For example Hillenbrand et al measured the field distribution in the vicinity of microstructures made of SiC with a scanning near-field optical microscope [11]. They applied electrostatic theory to compare the resonance behavior of particles made of SiC with particles made of silver and gold. Anderson showed that the excitation of phonon resonances in small spheres made of SiC will lead to an enhanced infrared absorbtion for molecules attached to the surface of the particles, if the illumination wavelength is chosen to be equal to the phonon resonance wavelength[12].

SiC particles can be used as a complement for metallic particles in various recently developed optical devices designed e.g. for the guiding of light[13], filter applications[14] or an optical data storage system[15]. A significant advantage in the use of SiC instead of metals is its smaller imaginary part in the dielectric constant[11]. This will result in a weaker damping and a corresponding sharper resonance. As the light source for the different applications, a quantum cascaded laser could be used[16], which emits in the appropriate spectral region. In addition, SiC offers the advantage that environmental conditions affect the lattice parameters, resulting in a change in the phonon polariton spectrum. This enables a broad range of sensor-type applications for the detection of changing environmental parameters such as temperature or pressure. However, for all these application, it is first necessary to understand in detail the characteristics of the phonon polariton resonance in SiC particles. As the geometrical shape of the scatterer is one of the major parameters, which influences the phonon polariton response, we will present a detailed study of the excitation of small particle phonon polaritons in cylindrical particles made of 6H-SiC as a function of the geometrical cross section. The cylinders have an infinite extension in the third dimension. These calculations serve as a preliminary analysis for an experimental investigation that is currently in progress. The structures that are currently fabricated, are essentially one-dimensional gratings, which corresponds to the simulated situation.

The numerical method used to analyze the scattering properties is the Boundary Element Method (BEM)[17]. A detailed description of the method can be found in Appendix I. We will start our investigations in analyzing the simplest structures; circular and elliptical cylinders. Such particles exhibit two resonance wavelengths. Illuminating the particle under an angle will excite both phonon polaritons. It will be shown that the resonance wavelength can be tuned by changing the axis ratio of the elliptical particles. The strength can be tuned by changing the size of the particles at a constant axis ratio. Additionally we will analyze objects, which exhibit a more complicated phonon polariton response, like rectangular and triangular cylinders. Their phonon polariton response is split into a band that are all excited independent of the illumination direction. Finally we will compare the excitation of phonon polaritons with the excitation of plasmon polaritons in metallic nano particles.

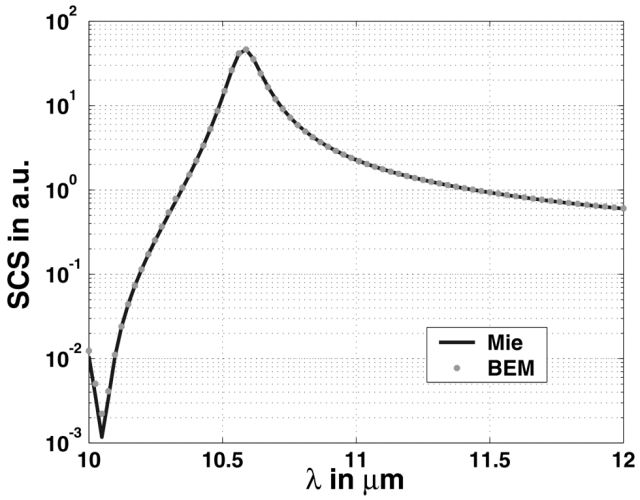

Figure 1: SCS of a SiC circular cylinder with $r = 500\ nm$ calculated with BEM and Mie theory.

2 Response of circular and elliptical cylinders

The simplest structure that can be analyzed is a circular cylinder. Figure 1 shows the SCS as a function of the wavelength for a circular scatterer with a radius of $r = 500\ nm$. Excitation of phonon polaritons is only possible using TM-polarized light, which means that the magnetic field oscillates parallel to the cylinder. For all structures, we have calculated the magnitude of the near-field amplitude (illuminating amplitude is unity) distribution to visualize the excited surface phonon polaritons (H_z component of the electro-magnetic field) and the SCS as defined in [19]. Because the scattering problem consists of a plane wave incident on an infinite circular cylinder, Mie theory exists as a quasi-analytical solution and we can compare the results obtained from the BEM with the correct solution[20] to verify implementation of the BEM. It can be seen that the results for both theories are in excellent agreement and a sharp maximum in the SCS appears at 10.6 μm. A resonance is excited if the dielectric constant approaches a value of -1. The resonance wavelength corresponds to the local maximum of the SCS. In Fig. 2 the dielectric constant of 6H-SiC that was assumed in the calculation is shown[21]. These values were used for all calculations in this paper. At a wavelength of 10.6 μm the dielectric constant of SiC is $-1.15 + i\ 0.13$ which is close to the resonance condition. The slight red-shift of the resonance

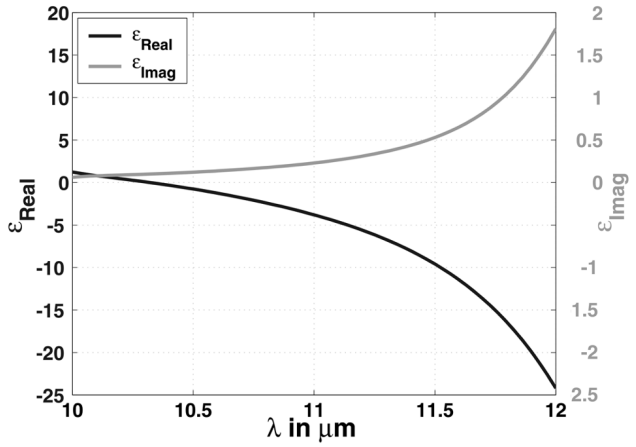

Figure 2: Real and imaginary part of the dielectric constant of SiC.

wavelength (the real part is -1 at $\lambda = 10.55\ \mu m$) is due to the finite size of the cylinder and the non-zero imaginary part of the dielectric constant. The resonant excitation of the dipole will lead to an enhanced SCS within a small wavelength range. The imaginary part diminishes the singular behavior. This leads to a damping and broadening of the response.

After the circular cross-section, the next simplest case is an elliptical cylinder. In Fig. 3, the SCS for an elliptical cylinder with a radius of the minor axis of $r_2 = 315\ nm$ and a radius for the major axis of $r_1 = 630\ nm$, illuminated along the two fundamental axes is shown. By illuminating the scatterer along its major axis (the k-vector is parallel to the major axis), a dipole will be excited at a wavelength of 10.45 μm. If the illumination direction is parallel to the minor axis, the dipole is excited at 10.78 μm. The near-field amplitudes for the phonon polaritons at the excitation wavelengths for which the SCS has its highest value are shown for the two illumination directions in Fig. 4. The arrow in the figure indicates the illumination direction, which is parallel to the k-vector. The field distribution of the dipole is comparable to the circular cylinder at the resonance condition. In Fig. 5 the SCS upon illuminating the object at three different angles, which are not coincident with one of the principle axis, are shown. The angles are 22^o, 45^o and 67^o and are taken with respect to the major axis.

As an intrinsic geometrical property the elliptical particle will support the two phonon polaritons at the two different wavelengths of 10.45 μm and 10.78 μm. By illuminating the structure at an angle, both phonon polari-

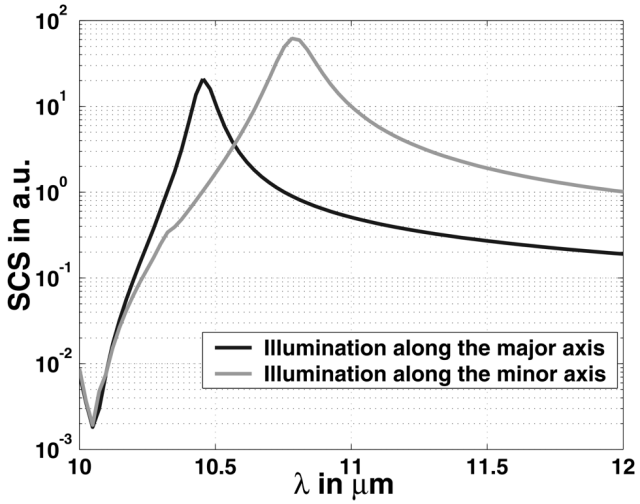

Figure 3: SCS of a SiC elliptical cylinder with $r_1 = 630\ nm$ and $r_2 = 315\ nm$.

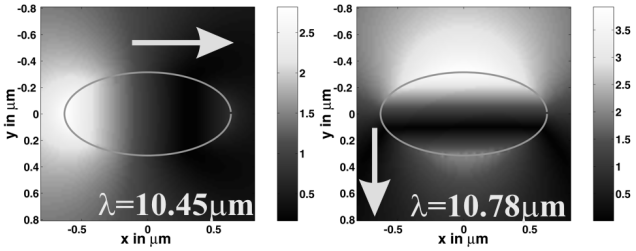

Figure 4: Near-field amplitude around an elliptical cylinder ($r_1 = 630\ nm$, $r_2 = 315\ nm$) at the resonance wavelengths.

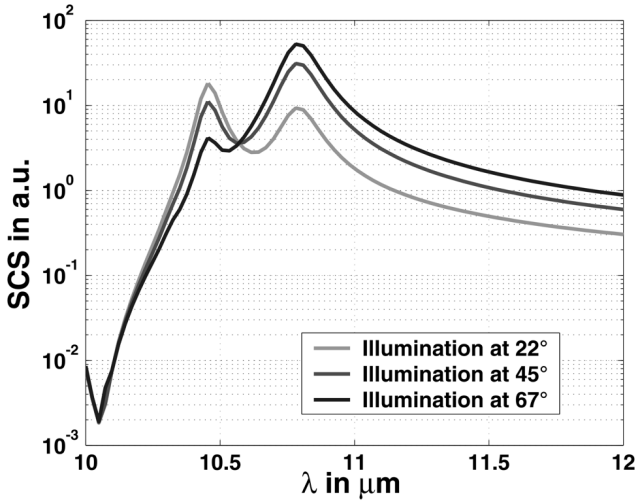

Figure 5: SCS of a SiC elliptical cylinder with $r_1 = 630\ nm$ and $r_2 = 315\ nm$ for three different illumination directions.

tons are excited. The strength of the excitation corresponds to the projection of the incoming wave vector on the two principal axes. In Fig. 6 the near-field distributions upon illuminating an elliptical particle at an angle of 45^o are shown. The wavelength corresponds to the two maxima in the SCS. Obviously the near-fields are comparable to the field distributions of the two dipoles. These are excited if one illuminates the particle along its principal axis, as shown in Fig. 4. The only noticeable difference is a slight rotation and consequently an asymmetry in the field distributions.

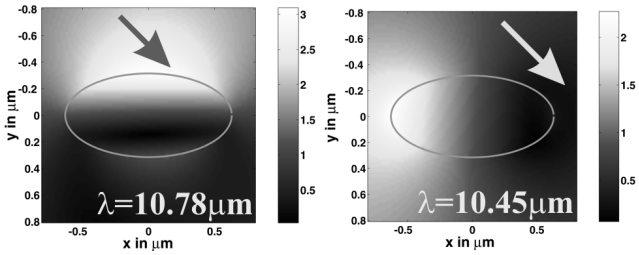

Figure 6: Near-field amplitude around an elliptical cylinder ($r_1 = 630\ nm$, $r_2 = 315\ nm$) at the resonance wavelength for an illumination direction of 45^o.

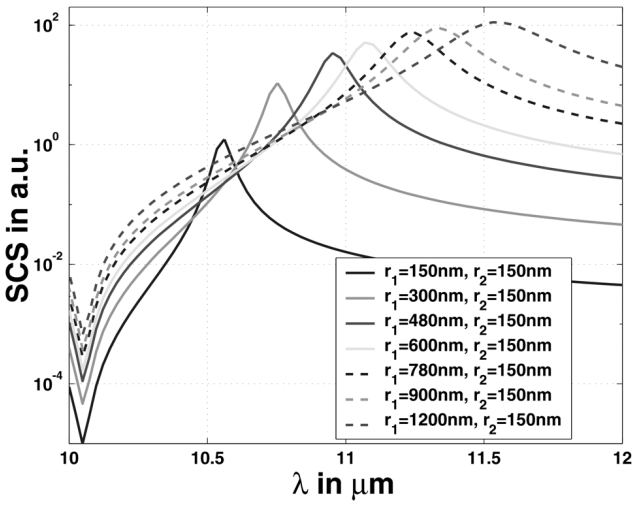

Figure 7: SCS of an elliptical cylinder as a function of the axis ratio (from 1 to 8).

3 Tuning the resonance wavelength of an elliptical particle

For an elliptical particle, two resonances exist corresponding to the radii of the major and minor axis. This is a straight forward response, which permits the tunability of the phonon polariton wavelength in an effective way. Just by changing the axis ratio of the particle, it is possible to manipulate the resonance behavior over a large wavelength range in an active manner. For sufficiently small particles, the size of the geometrical surface of the particle will not influence the resonance wavelength. Figure 7 shows the SCS for elliptical cylinders as a function of the axis ratio. The particles are illuminated along the minor axis. The minor axis is always 150 nm and the major axes are 150 $nm, 300$ $nm, 480$ $nm, 600$ $nm, 780$ $nm, 900$ nm and 1200 nm. The different resonance wavelengths can be well discriminated in Fig. 7 and span a range of approximately 1 μm. It can be seen from Fig. 7 that by increasing the axis ratio, the full width at half maximum will also be increased. It changes from a value of 100 nm at an axis ratio of 1, to a full width of 500 nm at an axis ratio of 8. This is due to two effects. The first reason is a steady increase in the imaginary part of the dielectric constant at higher wavelengths (see Fig. 2). As was shown in the previous section, the full

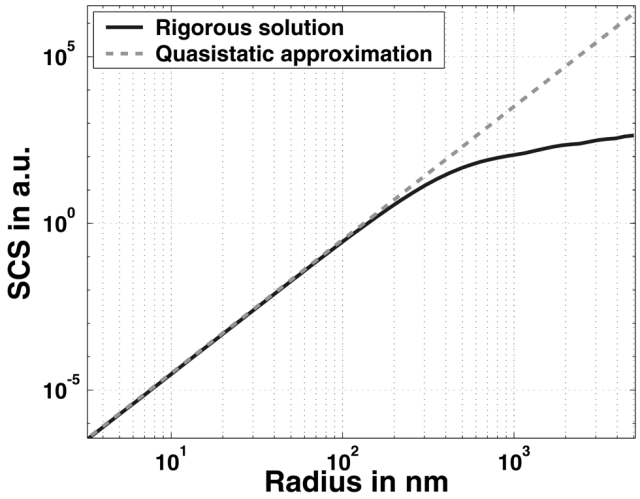

Figure 8: Maximum of the SCS as a function of the radius for a circular cylinder ($\lambda = 10.6\ \mu m$).

width at half maximum is increased if this part of the dielectric constant becomes larger. Another effect is an additional broadening and damping in the SCS, if the geometrical size of the particles becomes bigger. The field scattered by the particle suffers from phase retardation of the incoming wave front which broadens the SCS.
In summary, the wavelength at which the resonance occurs can be manipulated by changing the axis ratio of an elliptical particle. In the following section we will show how it is possible to control in addition the strength of the resonance, to balance the magnitude of the SCS for each of the particles.

4 Tuning the resonance strength of an elliptical particle

In Fig. 8 the maximum of the SCS as a function of the radius for a circular cylinder is shown. The maximum is at $\lambda = 10.6\ \mu m$. For comparison, the strength of the SCS calculated by applying the quasistatic approximation is likewise shown in the figure[20]. For small particles the strength of the SCS scales with the fourth power of the radius, which makes it possible to tune the strength of the SCS in a controlled manner, just by changing the size of the

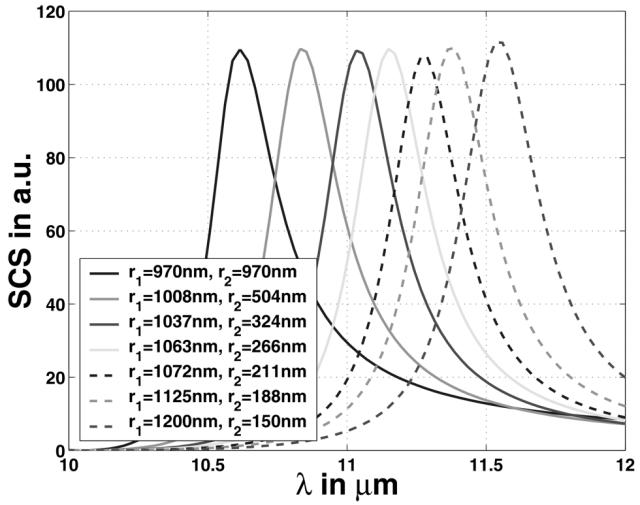

Figure 9: SCS of an elliptical cylinder as a function of the radii.

cylinder. The dipole wavelength remains constant for very small particles. For larger radii the strength as calculated using rigorous methods becomes weaker than predicted by the electrostatic approximation. The origin of this effect is the phase retardation inside the particle that results in a damping of the total field by scattered field contributions that are out of phase. Such a rigorous calculation of the scattering strength as a function of the size can be done for all the elliptical cylinders and qualitatively the behavior is the same independent of the axis ratio. The wavelength for which the maximum in the SCS occurs remains fixed as long as the size of the particles does not become too large. Increasing the size will cause a red shift in the resonance wavelength for moderate particle radii.

The tunability of the strength of the SCS by changing the size of the particles offers the possibility to adjust the SCS for all the particles to an equal level. Figure 9 shows the SCS on a linear scale for the particles with the same axis ratios as in Fig. 7, but with optimized overall size.

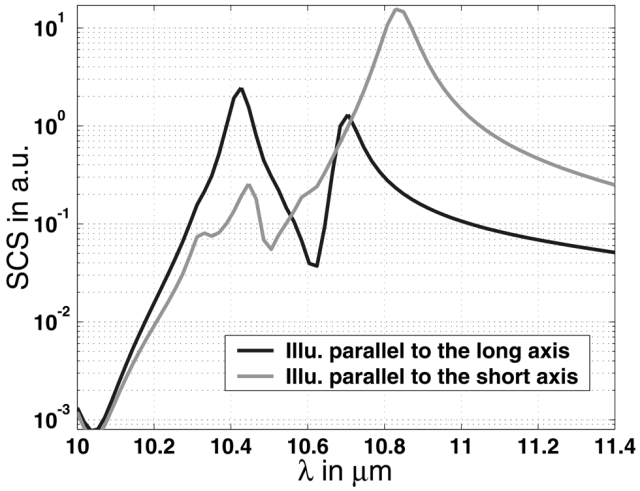

Figure 10: SCS of a SiC rectangular cylinder with $a = 672\ nm$ and $b = 328\ nm$.

5 Response of cylinders with different cross sections

5.1 The rectangular cylinder

To investigate geometries with a more complicated phonon polariton response, we have analyzed a rectangular object with a size of $328\ nm \times 672\ nm$. For a simulation of more realistic objects and to avoid numerical instabilities, the corners were approximated by circles with a radius of $40\ nm$. The SCS for two different illumination directions, which correspond to the axes of the particle, are shown in Fig. 10. Illuminating the rectangular cylinder along its short axis will excite a dominant dipole at $10.83\ \mu m$. A dipole for an illumination direction along the long axis is excited at $10.42\ \mu m$. Its amplitude is strongest on the illumination side and the field on the backside is significantly lower. This resembles the behavior of the dipole excitation at an elliptical cylinder (Fig. 6). An additional higher multipole is excited at $10.70\ \mu m$. The near-field distributions for the resonances when illuminating the structure along its long axis are shown in Fig. 11. Calculating all the near-field amplitudes upon illuminating the object along the short axis reveals likewise the excitation of an additional higher multipole at $10.42\ \mu m$. Nonetheless, the resonance strength is significantly lower than the strength

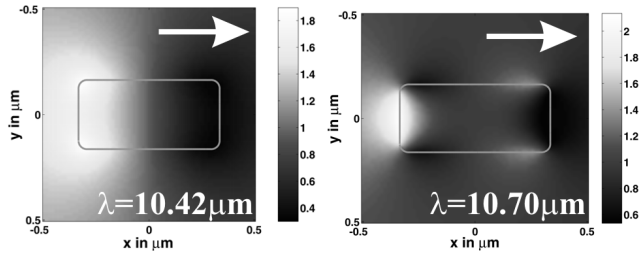

Figure 11: Near-field amplitude around a rectangular cylinder ($a = 672\ nm$, $b = 328\ nm$) at the resonance wavelength for an illumination direction along the long axis.

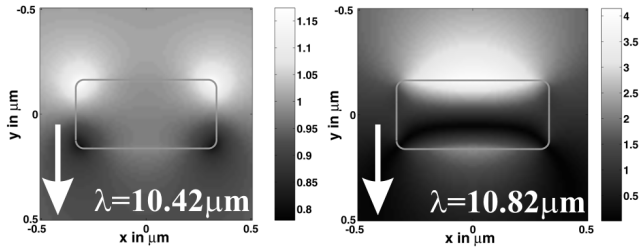

Figure 12: Near-field amplitude around an rectangular cylinder ($a = 672\ nm$, $b = 328\ nm$) at the resonance wavelength for an illumination direction along the short axis.

of the dominant dipole. Figure 12 shows the near-field amplitudes for the excited phonon polaritons of the rectangular cylinder for an illumination direction along the short axis. For an estimation of the size dependence of the SCS, we have calculated the SCS for the same axis ratio but for different absolute sizes of the cylinder with an rectangular cross section. In Fig. 13 the SCS for three rectangular cylinders is shown. The inset rectangle and arrow indicate the illumination direction relative to the particle. The sizes are $a_1 = 672\ nm,\ b_1 = 328\ nm$; $a_2 = 1680\ nm,\ b_2 = 820\ nm$ and $a_3 = 3360\ nm,\ b_3 = 1640\ nm$. It can be seen that like the behavior of a circular cylinder, the resonance wavelengths remain approximately constant for moderate particle sizes. An excessive increase will produce a red-shift of the spectra. The second important point that is comparable to the behavior of a circular cylinder is the increase of the half width of the SCS for increasing particle sizes. As was shown for cylinders with an elliptical cross section, the resonance wavelength can be tuned over a certain range by changing the

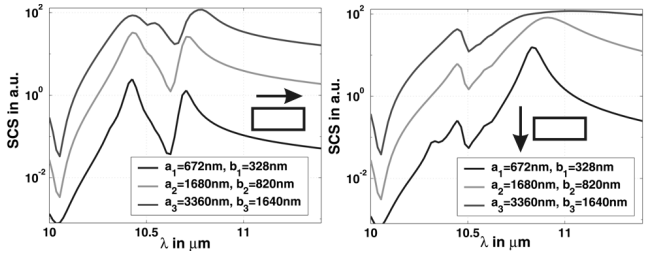

Figure 13: SCS of a SiC rectangular cylinder with different sizes at the the same axis ratio.

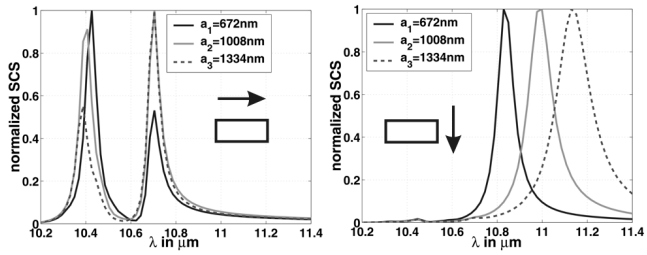

Figure 14: Normalized SCS of a SiC rectangular cylinder for three different object sizes.

axis ratio of the particle. Figure 14 shows the normalized SCS for a rectangular cylinder for three different axis ratios. The inset indicates the major axis, the length of the minor axis was kept constant at $b = 328nm$. The resonance wavelength can be well discriminated for the illumination along the short axis. The resonances for the illumination direction along the long axis remain to a good approximation constant. As one can see in the left part of Fig. 14, the only change occurs in the amplitude ratio between the two resonances. From this and similar calculations we have found that the rectangular cylinder will always support the excitation of two phonon polaritons.

5.2 The triangular cylinder

A further complicated structure is the triangular cylinder. We will treat here the special case of a right angled triangle. The base c is 848 nm and $a = b = 600\ nm$. A similar round-off procedure for the corner of the triangular as for the rectangular cylinder was applied. The radius of the

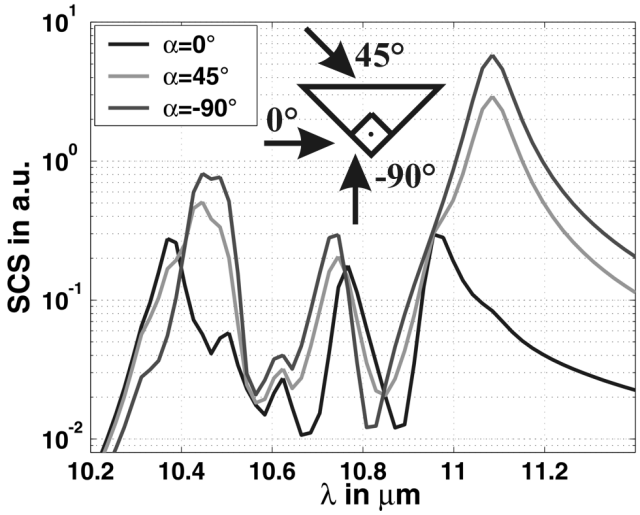

Figure 15: SCS of a SiC triangular cylinder with $c = 848\ nm$ and $a = b = 600\ nm$.

corner was 10 nm. The SCS of such an object for three different illumination directions is shown in Fig. 15. The geometry is shown in the inset to the figure. It can be seen that in good approximation five phonon polaritons are excited independent of the illumination direction. They are not present in the SCS for each illumination direction, because they are sometimes hidden behind the dominant contribution to the SCS of another phonon polariton, but calculating the near-fields reveals their existence. The single phonon polariton of a circular cylinder is split into a band of five phonon polaritons for a triangular cylinder. The near-field amplitude distributions of four excited phonon polaritons for the illumination direction of -90^o are shown in Fig. 16. Except for the phonon polariton excited at 11.08 μm, which is in good approximation a dipole, it becomes difficult to give the order of multipole for each of the phonon polaritons.
For the other illumination directions the field distributions look similar to the fields as shown for the illumination direction of -90^o and are omitted here.

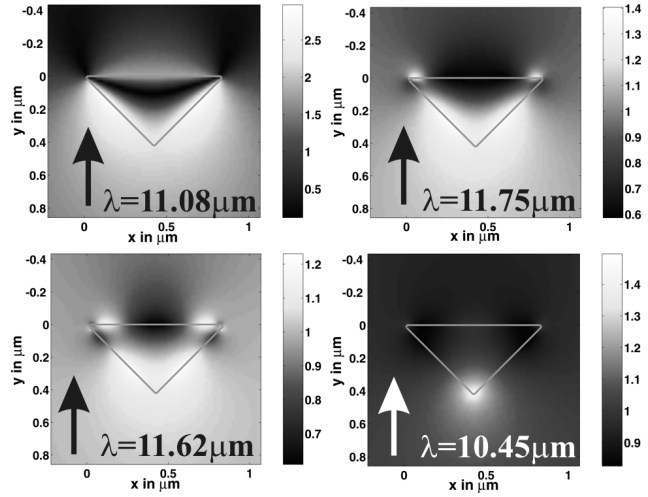

Figure 16: Near-field amplitude around a triangular cylinder ($c = 848\ nm$, $a = b = 600\ nm$) at the resonance wavelength for the (11)-direction as indicated by the arrow.

6 Comparing phonon polaritons with plasmon polaritons

A similar resonance effect that appears in metallic nano particles, is the excitation of a plasmon polariton. Such an excitation will also cause an enhanced SCS and a large near-field amplitude. A plasmon polariton is a resonant oscillation of free electrons in the material, as outlined in the introduction and appears in metals that have an appropriate negative dielectric constant in the visible part of the spectrum.
We used silver as the material in the simulations, because of its lower imaginary part in the dielectric constant compared to other metals such as gold or aluminium[5]. Two cardinal geometries, the circular and the quadratic cylinder, have been analyzed in terms of the scattering strength (SCS) and the amplitude enhancement of the magnetic field on the surface of the particle. To eliminate the influence of the absolute size on the response, the results are presented as a function of the wavelength divided by the radius of the circular cylinder or divided by the side length of the quadratic cylinder, respectively.
Figure 17 a shows the SCS of a circular cylinder made of silver ($r_{Ag} =$

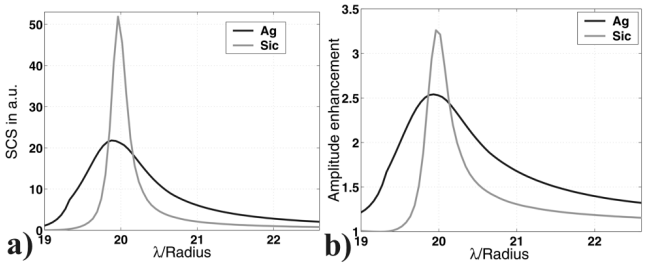

Figure 17: Comparing the SCS and the near-field amplitude enhancement of a circular cylinder made of Ag and SiC.

17.15 nm) and made of silicon carbide ($r_{SiC} = 530\ nm$). It can be seen that the strength of the SCS for the particle made of SiC is nearly double the strength of the silver particle. The full width at half-maximum (FWHM) for the SiC cylinder is four times smaller than the FWHM for the particle made of silver, assuming a wavelength per radius as the unit. The effect is attributed to the significantly smaller imaginary part in the dielectric constant, as the geometry with respect to the wavelength is the same for the two cylinders. The imaginary part for silver at the plasmon wavelength of roughly 340 nm is approximately double the corresponding value for SiC at about 10.6 μm and will cause a dampening and a broadening of the SCS. A similar behavior can be seen by analyzing the amplitude enhancement of the magnetic field directly at the surface of the particle. Results are shown in Fig. 17 b again for the same circular cylinders. The difference in the amplitude enhancement is less pronounced, but the enhancement is still higher for the particle made of SiC. The FWHM is again a factor of four smaller for the SiC particle than the corresponding value for silver.
Similar results have been obtained by comparing the scattering response of quadratic cylinders made of SiC ($a = b = 535\ nm$) and silver ($a = b = 18\ nm$). The SCS and the field enhancement on the surface for these objects are shown in Fig. 18 a and b, respectively. Again a difference in the strength and the FWHM for both the SCS and the field enhancement can be seen. The phonon polaritons are more efficiently excited and their singular nature is more pronounced, due to the lower imaginary part in the dielectric constant. Additionally a splitting of the single phonon polariton into three phonon polaritons is clearly observed. Such a splitting is attributed to the sharp corners in the geometry of the structure. The phonon polaritons are less strongly attenuated, whereas in silver the higher imaginary part in the

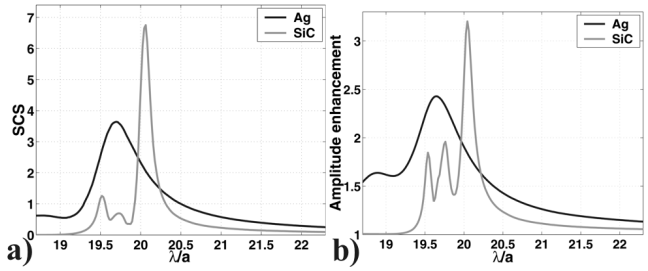

Figure 18: Comparing the SCS and the near-field amplitude enhancement of a quadratic cylinder made of Ag and SiC.

dielectric constant will cause a broadening and damping, such that the fine structures do not appear in the spectrum. The spectrum is dominated by the dipole response associated with the basic quadratic cross section.

7 Conclusions

We have applied the Boundary Element Method to the analysis of the small particle phonon polariton excitation in 6H-SiC. Phonon polaritons are lattice vibrations that can be resonantly excited at appropriate wavelengths in the far infrared part of the spectrum between 10 μm and 12 μm. Once a phonon polariton is excited, the energy that is scattered into the far-field as well as the near-field amplitude around the structure are enhanced. We have restricted the analysis to two-dimensional structures that are invariant in the third dimension. Firstly, we calculated the scattering properties of circular and elliptical cylinders and discussed the different damping mechanisms. These cylinders will support phonon polaritons at distinguishable wavelengths that can be related to the axis ratio of the particle. Illuminating the cylinder under an angle that does not correspond to one of the principal axes, will excite both resonances but with a strength that corresponds to the projection of the incoming wave-field on the two principal axis. It was shown that the resonance wavelength can be tuned in a controlled manner by changing the axis ratio. Changing the surface can control the scattering strength. Principally we found that the SCS becomes broadened and red-shifted for larger particles, independent of the geometrical cross section. For geometries other than elliptical, the single phonon polariton will be split into a band. Two phonon polaritons can be excited for rectangular and five phonon polaritons

for triangular cylinders.
By comparing the response of phonon polaritons excited in SiC and plasmon polaritons in silver, it is shown that the phonon polaritons are more efficiently excited due to the lower imaginary part in the dielectric constant. The singular nature of the phonon polaritons is more pronounced and a fine structure for the quadratic cylinders associated with the sharp corners was revealed. Such a response was not found for particles made of silver. The imaginary part in the dielectric constant of silver is too high, which will cause a significant damping and broadening of the plasmon polariton response compared with the response of SiC.

8 Acknowledgments

This research was supported by the European Union within the framework of the Future and Emerging Technologies-SLAM program under grant No. IST-2000-26479. The authors would like to thank Wataru Nakagawa for a careful reading of this manuscript.

References

[1] L. Zheng, R. P. Joshi and C. Fazi, "Effects of barrier height fluctuations and electron tunneling on the reverse characteristics of 6H-SiC Schottky contacts", J. Appl. Phys., **85**, 3701–3707 (1999).

[2] G. Ziegler, P. Lang, Dietmar Theis, C. Weyrich, "Single Crystal Growth of SiC Substrate Material for Blue Light Emitting Diodes", IEEE Trans. Elec. Dev., **30**, 277–281 (1983).

[3] K.-H. Lee, C. H. Park, B.-H. Cheong and K. J. Chang, "First-Principles study of the optical properties of SiC", Solid State Commun., **92**, 869–872 (1994).

[4] W. J. Moore, R. T. Holm, M. J. Yang and J. A. Freitas Jr., "Infrared dielectric constant of cubic SiC", J. Appl. Phys., **78**, 7255–7258 (1995).

[5] P. B. Johnson and R. W. Christy, "Optical Constants of the Nobel Metals", Phys. Rev. B, **6**, 4370–4379 (1972).

[6] J. P. Kottmann and O. J. F. Martin, "Influence of the cross section and the permittivity on the plasmon-resonance spectrum of silver nanowires", Appl. Phys. B, **73**, 299–304 (2001).

[7] H. Mutschke, A. C. Andersen, D. Clément, T. Henning and G. Peiter, "Infrared properties of SiC particles.", Astron. Astrophys., **345**, 187–202 (1999).

[8] T. Bernatowicz, G. Fraundorf, T. Ming, E. Anders, B. Wopenka, E. Zinner and P. Fraundorf, "Evidence for interstellar SiC in the Murray carbonaceous meteorite", Nature, **330**, 728–730 (1987).

[9] J. J. Greffet, R. Carminati, K. Joulain, J. P. Mulet, S. Mainguy and Y. Chen, "Coherent emission of light by thermal sources", Nature, **416**, 61–64 (2002).

[10] J. Le Gall, M. Olivier and J. J. Greffet, "Experimental and theoretical study of reflection and coherent thermal emissionby a SiC grating supporting a surface-phonon polariton", Phys. Rev. B, **55**, 10105–10114 (1997).

[11] R. Hillenbrand, T. Taubner and F. Keilmann, "Phonon-enhanced light-matter interaction at the nanometre scale ", Nature, **418**, 159–162 (2002).

[12] M. S. Anderson, "Enhanced infrared absorption with dielectric nanoparticles", Appl. Phys. Lett., **83**, 2964–2966 (2003).

[13] S. A. Maier, M. L. Brongersma, P. G. Kik, S. Meltzer, A. A. G. Requicha and H. A. Atwater, "Plasmonics - a route to nanoscale optical devices", Adv. Mater., **13**, 1501–1505 (2001).

[14] S. Linden, A. Christ, J. Kuhl and H. Giessen, "Selective suppression of extinction within the surface plasmon resonance of gold nanoparticles", Appl. Phys. B, **73**, 311–316 (2001).

[15] H. Dittlbacher, J.R. Krenn, B. Lamprecht, A. Leitner and F.R. Aussenegg,"Spectrally coded optical data storage by metal nanoparticles", Opt. Letters, **25**, 563–565 (2000)

[16] J. Faist, F. Capasso, D.L. Sivco, C. Sirtori, A.L. Hutchinson and A.Y. Cho, "Quantum cascade laser", Science, **264**, 553–556 (1994).

[17] A. Madrazo and M. Nieto-Vesperinas, "Scattering of electromagnetic waves from a cylinder in front of a conducting plane", J. Opt. Soc. Am. A, **12**, 1298–1309 (1995).

[18] C. Rockstuhl, M. Salt, H. P. Herzig, "Application of the boundary-element method to the interaction of light with single and coupled metallic nanoparticles", J. Opt. Soc. Am. A, **20**, 1969–1973 (2003).

[19] M. Born and E. Wolf, *Principles of Optics* (Cambridge University Press, 1999).

[20] C. F. Bohren and D. R. Huffmann, *Absorption and Scattering of Light by Small Particles* (Wiley, New York, 1983).

[21] E. Palik, *Handbook of optical constants of solids*, (Academic Press, San Diego, 1985).

Wavelength dependent optical force on elliptical silver cylinders at plasmon resonance

Carsten Rockstuhl and Hans Peter Herzig

University of Neuchâtel, Institute of Microtechnology,
Rue A.-L. Breguet 2, CH-2000 Neuchâtel, Switzerland

October 15, 2004

Abstract

In this letter we use rigorous diffraction theory to analyze the force on elliptical cylinders made of silver as a function of the elongation. We find that by illuminating the wires at the plasmon wavelength and placing them in a highly focussed Gaussian beam, they are attracted towards the optical axis if the waist of the laser is behind the wire and repelled if the waist is before the wire. Also, the force distribution for illumination wavelengths smaller and larger than the plasmon wavelength are analyzed.

OSICS codes: 240.668, 290.0290, 350.4990, 350.3950

Illuminating silver or gold nano-particles at appropriate wavelengths excites a surface plasmon, which is a resonant oscillation of the free electrons in the material[1]. For particles with a non-circular or non-spherical geometry, rigorous diffraction theory must be used to determine precisely the wavelength for which a plasmon is excited. At the resonance a large scattering cross section (SCS)[2] and an enhanced near-field amplitude are observed. The enhanced near-field in the vicinity of the particles could be applied for example to a scanning near-field optical microscope, in which a trapped metallic particle serves as a highly spatially confined probe[3]. Another application is the photonic force microscope[4]. For both applications an optical tweezer is used to trap the particles[5]. The optical tweezer is a highly focussed laser beam which exerts a force on the particle, such that it can be stably trapped at a certain point. This is possible if all the forces acting on the particle are in equilibrium.

To describe the working principle of an optical tweezer applied to metallic particles two main approaches have been used in the past. The first is a ray-optical model, which can be used if the particle is significantly larger than the wavelength[6]. If the particle is much smaller than the wavelength, a dipole model is used[7]. For spherical particles between these size domains, Mie theory can be used to calculate the forces on metallic particles precisely[8].

In this letter we will use rigorous diffraction theory to determine the force on metallic wires. Recently, Arias-Gonzales et al. calculated rigorously the force on two-dimensional circular cylinders under the plasmon resonance condition by means of the extinction theorem boundary condition, mainly for plane wave or weakly focussed Gaussian-beam illumination[7] above substrates. We will analyze the force on silver elliptical cylinders illuminated by a highly focused laser beam as a function of the axis ratio and the wavelength by using the Multiple Multipole Method(MMP)[10]. We restrict ourself to two-dimensional structures. For the excitation of a plasmon the electric field vector must have a component that oscillates perpendicular to the geometrical cross section, thus a TM-polarized field is used for the illumination. The numerical procedure to calculate the force consists of two steps. First, the electric and magnetic fields are calculated along the surface of the cylinder. The wires are illuminated with a highly focused Gaussian beam whose waist equals one wavelength ($\omega = \lambda$), the amplitude of the illuminating Gaussian beam is $6.9V/m$, which is the amplitude of a three-dimensional beam with a power of $100mW$. The dielectric constants for silver where taken from the publication by Johnson and Christy[11] and the area of the elliptical cylinders

was kept constant at $A = \pi(20nm)^2$. The different elongations were obtained by multiplying or dividing the radii using the factors $\sqrt{2}$, $\sqrt{3}$ and $\sqrt{4}$. If the radius in the longitudinal direction r_1 was multiplied with the given factor, the opposite transversal radius r_2 was divided by the same factor in order to maintain the area.
In the second step the force exerted on the cylinder is calculated by applying the Maxwell stress tensor. Only the time average of the electromagnetic force is observed at optical frequencies. For a wire embedded in an isotropic medium the force is calculated using [9]

$$\begin{aligned}\langle \mathbf{F} \rangle &= \int_S \Big\{ \frac{\epsilon}{2} Re\left[(\mathbf{E}\cdot\mathbf{n})\mathbf{E}^\star\right] - \frac{\epsilon}{4}(\mathbf{E}\cdot\mathbf{E}^\star)\mathbf{n} \\ &\quad + \frac{\mu}{2} Re\left[(\mathbf{H}\cdot\mathbf{n})\mathbf{H}^\star\right] - \frac{\mu}{4}(\mathbf{H}\cdot\mathbf{H}^\star)\mathbf{n} \Big\}\, dl', \end{aligned} \tag{1}$$

with S being the circumference of the wire and $\overrightarrow{n}$ the normal to the surface. The normalized SCS for wavelengths between $300nm$ and $450nm$ assuming plane wave illumination are shown in Fig.1. The insets show the cylinder ori-

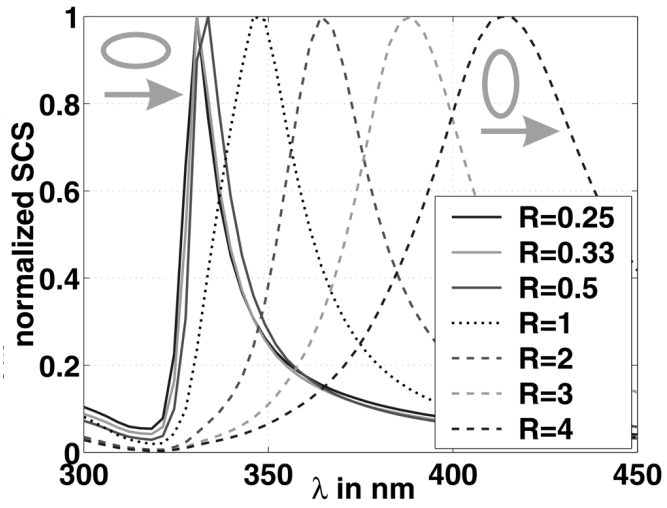

Figure 1: Normalized SCS of silver elliptical cylinders as a function of elongation.

entation with respect to the propagation direction of the illuminating beam for the two outermost elongated cylinders. The arrangement for all the other cylinders is the same. An excitation of a plasmon appears as a peak in the

SCS. r_1 is the radius of the wire parallel to the optical axis and r_2 is the perpendicular radius. It can be seen that the plasmon wavelength can be tuned over approximately 100nm and depends solely on the axis ratio ($R = r_2/r_1$), for a given material. The bigger the axis ratio the larger the red-shift as well as the full-width at half maximum (FWHM) of the excited plasmon. The reason for an increased FWHM for the wires with a bigger plasmon wavelength is mainly attributed to phase retardation inside the wire and an increasing imaginary part in the dielectric constant. Both effects causes a damping and broadening of the response and an overall smoothing of the SCS. The strength of the SCS is lowest for the wire with the lowest aspect ratio. The excited plasmons are dominated by a dipole excitation. An alternative way to control the plasmon wavelength is to change the size. Increasing the size of the cylinders will red-shift the wavelength and the overall achievable shift can be comparable to the difference of the plasmon wavelength between two subsequent chosen elongations. However, the overall achievable wavelength range is smaller and the major drawback is an increase of the width of the plasmon peak. We restrict our discussion hence to the possibility of changing the plasmon wavelength just by changing the elongation.

We calculated the force for different elongations as a function of the wavelength. A typical force distribution at the resonance wavelength is shown in Fig. 2 a for the circular cylinder ($r_1 = r_2 = 20nm$). The illumination wavelength was $\lambda_{Resonance} = 340nm$. The distribution of the force at a non-resonant wavelength is shown in Fig. 2 b ($\lambda = 450nm$) and c ($\lambda = 1500nm$). The amplitude distribution of the illuminating beam, which propagates in the positive z-direction, is shown in the background and the forces are shown on a non-linear scale to emphasize the direction. In the case of a wavelength close to the plasmon-wavelength (Figs. 2 a and b) the longitudinal force is always positive independent of the wire position, meaning that the wires are accelerated along the optical axis. For a wavelength far away from the plasmon resonance(Fig. 2 c), the gradient force dominates over the scattering force and the longitudinal force takes negative values on the optical axis behind the waist. The object could be trapped at a point a short distance behind the waist. The transversal force in the resonant case attracts the wire towards the optical axis if it is positioned before the waist and repels it from the optical axis if the wire is situated behind the waist. For a larger wavelength the wire is attracted towards the optical axis over an increased range including behind the waist. For a shorter wavelength the wire is repelled even at positions significantly before the waist. Such a behavior can be explained

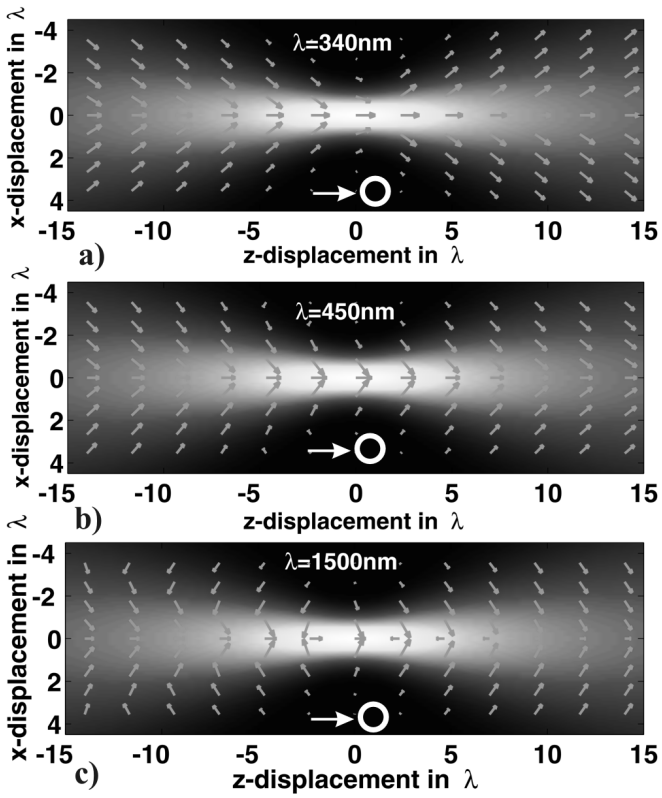

Figure 2: Force on a silver circular cylinder ($r_1 = r_2 = 20nm$) illuminated with a Gaussian beam at a) the plasmon resonance wavelength($\lambda = 340nm$), at b) an off-resonance wavelength($\lambda = 450nm$) and at c) a wavelength far away from the resonance($\lambda = 1500nm$).

by calculating the polarizability α of an elliptical cylinder assuming a dipole model. For an elliptical cylinder illuminated with a TM-polarized wave, α is proportional to $(\epsilon_i - \epsilon_a)(1 + R)(R\epsilon_a + \epsilon_i)^{-1}$, with ϵ_i being the dielectric constant of the cylinder, ϵ_a the dielectric constant of the surrounding medium. The real part of ϵ for silver in the relevant wavelength region is negative and for higher wavelengths this value decreases. For a simplified rough analysis we assume firstly that the imaginary part for the corresponding wavelength is small and can be hence neglected and discuss subsequently its influence on the behavior.

We can see that a plasmon is excited if the denominator becomes zero, which explains the increase of the plasmon wavelength for higher aspect ratios. For

wavelengths smaller than the plasmon wavelength, α becomes negative because the numerator, mainly given by $(\epsilon_i - \epsilon_a)$, is always smaller than zero and $R\epsilon_a + \epsilon_i$ is positive. The gradient force F_{grad}, proportional to $\alpha\nabla(\mid E \mid^2)$, points in the opposite direction to the gradient. This means that in this wavelength regime the wires are basically repelled from the optical axis. For wavelengths higher than the plasmon wavelength, the denominator also becomes negative and α becomes positive, which will cause an attraction of the wire towards the optical axis.
The entire wavelength dependence of the force for a wire whose minor axis is $r_1 = 20nm/\sqrt{3}$ and major axis is $r_2 = 20nm\sqrt{3}$ can be seen in Fig.3 a, where the on-axis longitudinal force as a function of the wavelength is shown. The longitudinal force is always maximum at the plasmon wavelength. This

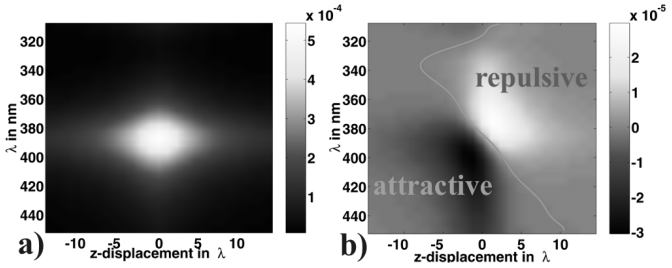

Figure 3: a) on-axis longitudinal force and b) transversal force evaluated parallel to the axis at $x = 0.44\lambda$ for an elliptical cylinder with $r_1 = \frac{20nm}{\sqrt{3}}, r_2 = 20nm\sqrt{3}$ as a function of the wavelength.

component is dominated by the scattering force, which is proportional to the intensity and the square of the absolute value of α, which is highest at the resonance. Correspondingly, a trapping of these objects at the plasmon wavelength is not possible by using a Gaussian beam, as the gradient force cannot equal the scattering force, which is the necessary condition for trapping. Trapping is possible instead by using a wavelength that is significantly larger than the plasmon wavelength, as shown in Fig. 2 c. In Fig. 3 b the transversal force evaluated off-axis along the z-axis at $x = 0.44\lambda$ is shown. A positive force F_x indicates a repulsion from the axis, a negative one an attraction. It is important to note that the same distribution was qualitatively found for each of the wires. The transversal force acting on the wire is strongest slightly behind the waist at a wavelength shorter than the resonance wavelength and smallest at a point slightly before the waist, at a

wavelength larger than the resonance. If the imaginary part of the dielectric constant were to be zero and if the application of the dipole approximation did not introduce a small error, the change of the sign for the force would appear exactly at the resonance wavelength independent of the z-displacement of the wire. The gradient force at this point is zero[7]. The non-negligible imaginary part as well as the finite size of the wire will cause a change of sign at different z-displacements for different wavelengths.
For a comparison of the differently elongated wires, we show in Fig.4 a the longitudinal force acting on the wires in the center of the waist as a function of the wavelength. The transversal force at the resonance wavelength evaluated

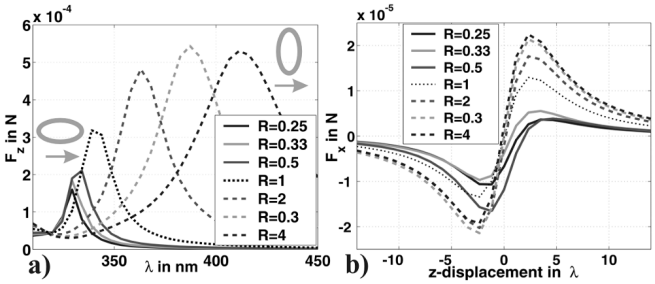

Figure 4: a) Longitudinal force in the center of the waist as a function of the wavelength and b) transversal force along the optical axis at $x = 0.44\lambda$ for the resonance wavelength.

parallel to the optical axis at $x = 0.44\lambda$ is shown in Fig.4 b. The longitudinal force becomes maximum at the plasmon wavelength. The behavior at the plasmon resonance wavelength of the transversal force is comparable for all the wires independent of the elongation direction. The wires are repelled at positions approximately after the waist and attracted for positions before the waist.
In summary, we have analyzed the force on elliptical silver cylinders as a function of the elongation and the wavelength. The longitudinal force is strongest at the plasmon wavelength. The transversal force undergoes a change of sign at the plasmon wavelength. Due to the non-negligible size of the wire as well as the imaginary part of the dielectric constant, this change of sign appears at different z-positions as a function of the wavelength. For wavelengths shorter than the plasmon wavelength, the wires are repelled from the optical axis. For wavelength larger, the wires are attracted. Such a different response to an applied focused wave-field offers a fascinating application using focused

beams for the sorting of metallic particles in accordance with their shape, orientation or perhaps material compositions using cascaded beams, where subsequent levels work at different wavelengths. Although only analyzed for a two-dimensional structure, the basic physical response will be the same for three-dimensions, such that this capability would be useful e.g. for selecting nano particles with a well defined resonance wavelength for plasmon-based waveguides or for the use of particles applied to Surface Enhanced Raman Spectroscopy. For a complete description of the flow of objects in wave-fields, the torque must be taken into account additionally, as it will cause an alignment of the object with respect to the optical axis. The analysis of the torque is currently under investigation.

This research was supported by the European Union under grant No. IST-2000-26479.

References

[1] J. P. Kottmann and O. J. F. Martin, Appl. Phys. B **73,** 299 (2001).

[2] M. Born and E. Wolf, *Principles of Optics* (Cambridge University Press, 1999).

[3] T. Sugiura, T. Okada, Y. Inouye, O. Nakamura and S. Kawata, Opt. Lett. **15**, 1663 (1997).

[4] A. Rohrbach, E.L. Florin, E.H.K. Stelzer, Proc. SPIE **4431**, 75 (2001).

[5] A. Ashkin, Phys. Rev. Lett. **24**, 156 (1970).

[6] P. Chun Ke and M. Gu, Appl. Opt. **38**, 160 (1999).

[7] J. R. Arias-Gonzáles and M. Nieto-Vesperinas, J. Opt. Soc. Am. A **20**, 1201 (2003).

[8] H. Furukawa and I. Yamaguchi, Opt. Lett. **23**, 216 (1998).

[9] M. Lester and M. Nieto-Vesperinas, Opt. Lett. **24**, 936 (1999).

[10] C. Hafner, "Post-Modern Electromagnetics.", John Wihley & Sons (1999).

[11] P. B. Johnson and R. W. Christy, Phys. Rev. B **6**, 4370 (1972).

Rigorous diffraction theory applied to the analysis of the optical force on elliptical nano- and micro-cylinders

Carsten Rockstuhl and Hans Peter Herzig

University of Neuchâtel, Institute of Microtechnology,
Rue A.-L. Breguet 2, CH-2000 Neuchâtel, Switzerland

October 15, 2004

Abstract

Illuminating nano- and micro-particles with a highly focused laser beam will exert a force on them that depends on different parameters, such as the particle size, refractive index and beam waist. In this paper rigorous diffraction theories are used to calculate the force on elliptically shaped dielectric cylinders in three different size regimes. We analyze the conditions for which the particles are attracted or repelled from the optical axis as a function of the geometry. Such a shape dependent response to optical wave-fields could be used to sort particles.

PACS: 42.25.Fx, 87.80.Cc

1 Introduction

Based on the pioneering work of Ashkin in the early seventies[1, 2], it is known that by illuminating dielectric micro - and nano-particles with laser beams a force is applied to the particles due to the exchange of momentum between the photons and the object[3]. Different interaction regimes can be distinguished, depending on the size and the shape of the particles, the parameters that characterize the illuminating beam and the contrast of the refractive index(defined as n_i/n_a, with n_i the refractive index of the object and n_a the index of the surrounding medium)[4]. It becomes possible to attract and accelerate particles along the optical axis in the propagation direction of the illuminating laser beam for particles that have a higher index of refraction than the surrounding medium[5]. The particles are repelled from the optical axis if the index contrast is smaller than unity[6]. For particles much smaller than the wavelength, it is possible to find points in space where all the forces that act on the particle are equal and the object is stably trapped in three dimensions[7]. Such optical tweezers have gained a lot of interest in the past due to their large range of possible applications, both in fundamental as well as in applied sciences. Two examples are the levitation of particles[8] or near-field scanning optical microscopy[9].

For a qualitative description of how optical tweezers work, two different approaches are usually used, which apply in different size regimes. The ray-optics model is used to explain the behavior of optical tweezers if the particle size is much larger than the wavelength. The beam is treated as a superposition of rays and the two refractions when a ray enters and exits the particle are modelled using Snell's law. Each ray undergoes a change in momentum between the incoming and outgoing ray. Due to conservation laws, the momentum in a system remains invariant, so the transfer of momentum between ray and particle can be calculated for each ray that is refracted. Summing up the momenta will result in a net force, which will accelerate the particle[6].

For particles much smaller than the wavelength, such a ray-optics model does not apply. For these particles a dipole approximation can be used for describing the light-particle interaction to characterize the scattering properties in a simplified manner. The object is considered as an emitting dipole and the force that acts on the particle can be decomposed into a scattering and a gradient force[10].

If the size of the particle is comparable to the wavelength, neither approximation can be used and instead the problem must be solved rigorously in

two steps. In the first step, the diffraction problem is solved and the field around the particle is calculated rigorously. The force acting on the particle can be determined in the second computational step by applying Maxwell's stress tensor[11]. A simple and elegant way to find the field around spherical objects is the use of the generalized Lorenz-Mie theory (GLMT)[12], which describes in its original formulation strictly the interaction of an arbitrary shaped beam with a homogenous sphere. The theory makes use of an expansion of the field components using scalar potentials and a separation of variables in the coordinate system associated with the particle[13]. Consequently, this size regime is often called the Mie domain[14]. The theory has been extended to other geometries, such as layered spheres[15], cylindrical objects[16] and elliptical cylindrical objects[17]. In the past the theory was also applied to calculate the optical force on spheres[18] and more recently by Lock[19, 20]. Force and torque calculations on other geometries such as multilayered spheres[21] have been also reported.

For non-spherical objects the diffraction problem can be solved with various methods. In the past Nieminen et al. applied the T-matrix approach to the problem and calculated the force on some non-spherical objects[11, 22]. Nieto-Vesperinas et al. demonstrated that the Coupled Dipole Method (CDM) can be used for this problem[23] and analyzed the force on circular cylinders above surfaces.

In this paper we will apply the Multiple Multipole Method[26] to analyze the force exerted on cylindrical circular and elliptical objects for different size domains and for different index contrasts as a function of the axis ratio. Such a rigorous treatment for non circular particles was mainly restricted in the past to specific calculations for a set of parameters that corresponds to an experimental situation. No comprehensive rigorous analysis of the force on particles with a non-circular geometrical cross section has been performed so far. In this paper, we will present this rigorous analysis and show explicitly the transition of the force between the different size regimes. We will restrict ourselves to two-dimensional objects that are of infinite extent in the third dimension. All of the main physical aspects are included in this model, which allows to analyze of the behavior of these particles without any approximation.

2 Calculating the force on arbitrarily shaped particles

To calculate the force that acts on arbitrarily shaped micro- and nano-particles the computational procedure consists of two steps. In the first step the electro-magnetic field distribution along the surface of the object must be solved rigorously.

For simplicity and because the force will be calculated in various positions relative to the waist of a given illuminating laser beam propagating in the positive z-direction, the most common approach is to decompose the illuminating beam into a plane wave spectrum and calculate the field distribution for each illumination direction separately. For a numerical description the spectrum is discrete, with a finite number of plane waves, which will introduce a periodicity of the illuminating beam of Λ. If the particle is positioned at a point (x, z) relative to the center of the waist of the beam, the complex amplitude of the m'th order illumination plane wave is given by[27]

$$A_m = \frac{e^{-i\sqrt{(\frac{2\pi}{\lambda})^2-(m\frac{2\pi}{\Lambda})^2}z}}{\Lambda} \int_{-\frac{\Lambda}{2}}^{\frac{\Lambda}{2}} a_{Inc}(x) e^{-im\frac{2\pi}{\Lambda}x} dx, \tag{1}$$

with $a_{Inc}(x)$ being the amplitude distribution in the waist, Λ is the assumed periodicity of the illuminating wave-field that has to be choosen large enough. m the diffraction order. $a_{Inc}(x)$ for a Gaussian beam in the waist is given by

$$a_{Inc}(x) = E_0 e^{-\left(\frac{x}{\omega}\right)^2}, \tag{2}$$

with E_0 the beam amplitude and ω the waist. However, the final beam used in the calculation for the illumination is not given by this equation, as a focused Gaussian beam does not satisfy Eqn. 2. The angular spectrum of the illuminating beam is truncated, such that only the propagating waves will interact with the sphere. The evanescent waves of the angular spectrum will not contribute. Neglecting the effects of a necessary high NA system to obtain a highly focused laser beam, the illuminating beam as described by equation 2 and 1 can be generated by a classical far-field lens system. We used $\Lambda = 20\lambda$, which will give 41 propagating orders in air. To solve the interaction of a plane wave with cylindrical objects, the Multiple Multipole Method(MMP) is used[34, 26, 33]. The MMP is a semi-analytical method, in which the description of the electromagnetic field in regions with a homogenous dielectric constant uses known analytical solutions of the wave

equation. The field is written as a superposition of multipoles emitting from different spatial positions. The multipoles are Hankel functions of the first order and 75 multipoles were used for convergence of the numerical results. The surface was sampled using 500 points. If the fields across the surface of the particle are calculated for each propagation direction, the entire field at an arbitrary point in the space is given by a superposition of the plane wave response multiplied by the appropriate amplitude coefficient A_m.
Once the field is known, the second step involves the application of Maxwell's stress tensor to find the force on the particle[28, 29]. At optical frequencies only the time average of the electromagnetic force is observed. For a particle embedded in an isotropic medium the force is calculated as [31]

$$\begin{aligned}\langle \overrightarrow{F} \rangle &= \int_S \Big\{ \frac{\epsilon}{2} Re\left[(\overrightarrow{E} \cdot \overrightarrow{n}) \overrightarrow{E}^\star \right] - \frac{\epsilon}{4} (\overrightarrow{E} \cdot \overrightarrow{E}^\star) \overrightarrow{n} \\ &\quad + \frac{\mu}{2} Re\left[(\overrightarrow{H} \cdot \overrightarrow{n}) \overrightarrow{H}^\star \right] - \frac{\mu}{4} (\overrightarrow{H} \cdot \overrightarrow{H}^\star) \overrightarrow{n} \Big\} dl' \end{aligned} \quad (3)$$

with S being the surface of the particle and $\overrightarrow{n}$ the normal to the surface pointing outward.
To ensure the correct implementation of our algorithm, we have first compared it with results published in the literature by Chaumet et al.[23]. Excellent agreement was found for both polarizations for the force acting on a $10nm$ glass cylinder. In addition we compared results for a dielectric cylinder with different radii calculated with Lorenz-Mie theory[35], with the MMP and also with the Boundary Element Method (BEM)[24, 25]. In all cases the results agree very well. As an example we show in Fig. 1 the transverse force acting on a cylinder with $r = 0.5\lambda$ and $n = 1.5$ evaluated along the z-axis at $x = -0.44\lambda$. The illuminating beam was a Gaussian one with a waist of $\omega = \lambda$. The refractive index of the surrounding medium was air. All three methods give the same result. An interpretation of the results is given in the next section, where we analyze the force exerted on dielectric cylinders in air by a Gaussian beam.

3 Large dielectric particles in air

In this section we analyze the force on elliptical particles made of glass ($n_i = 1.5$) in air as a function of the elongation if their size is comparable to the wavelength. Figure 2 shows the geometry of the particles used for

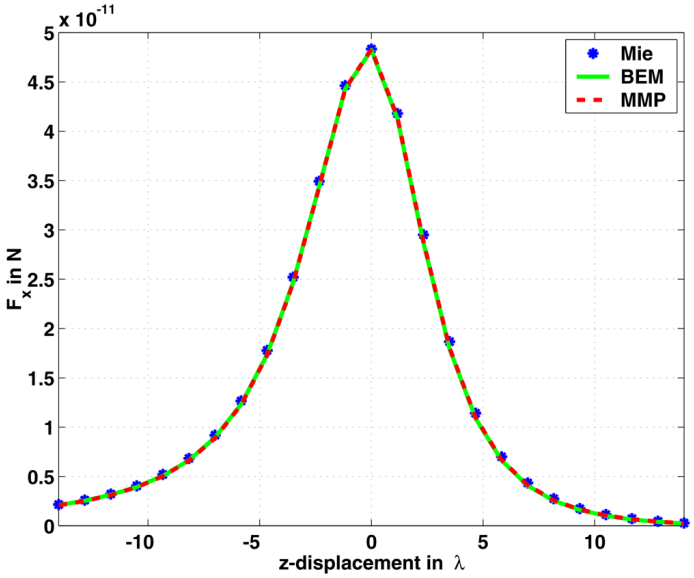

Figure 1: Transverse force on a circular cylinder calculated with three different techniques (parameters are given in the text).

the simulation as a function of the axis ratio R. The axis ratio is defined as $R = \frac{r_2}{r_1}$. The radius r_1 is the radius of the elliptical cylinder in the z-direction, the direction of propagation of the laser beam. They all have an equal area and seven different ellipticities are considered. The three elongations are chosen by multiplying the reference radius r_{Ref} by $\sqrt{2}$, $\sqrt{3}$ and $\sqrt{4}$. To keep the area constant in each case, the orthogonal radius is divided by the same factor. The two different elongation directions are transversal (perpendicular to the optical axis, with the radius r_1 being the reference radius multiplied by a factor smaller than unity) and longitudinal (parallel to the optical axis, the radius r_1 being the reference radius multiplied by a factor larger than unity).

In Fig. 3 a and 3 b the longitudinal force that acts on the particles along the optical axis is shown for a cylinder with a reference radius of $r_{Ref} = 0.5\lambda$ as a function of the elongation for TE polarization and for TM polarization. The particles are illuminated with a Gaussian beam. For all of our simulations, if not stated otherwise, we have chosen a waist ω equal to the wavelength and the amplitude of the illuminating Gaussian beam was chosen to be $6.9V/m$ that is the corresponding amplitude of the three-dimensional beam with a

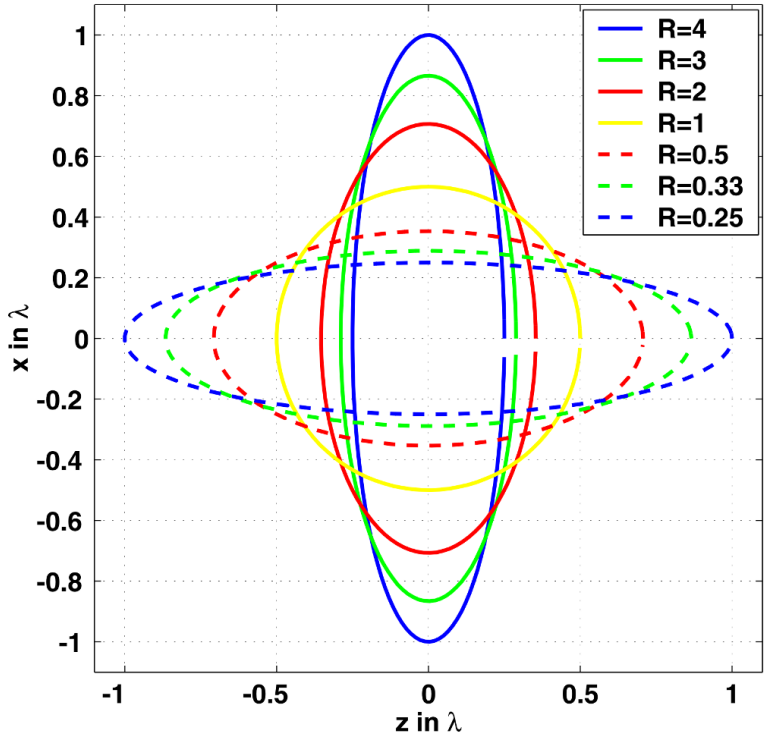

Figure 2: Geometry of the elliptical particles used in the simulation.

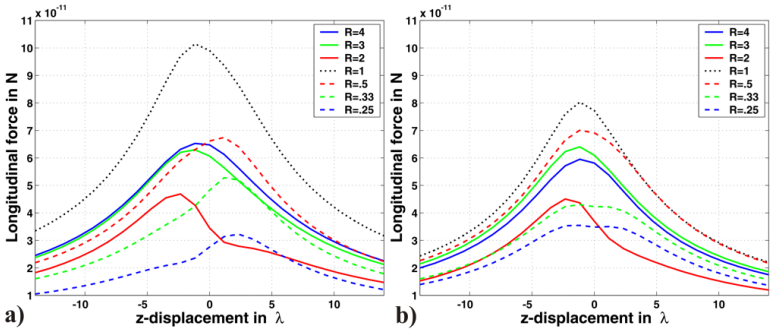

Figure 3: Longitudinal force on dielectric elliptical cylinder on the axis with $\mathbf{r_{Ref}} = \mathbf{0.5}\lambda$ assuming a) a TE-polarized and b) a TM-polarized Gaussian beam for illumination.

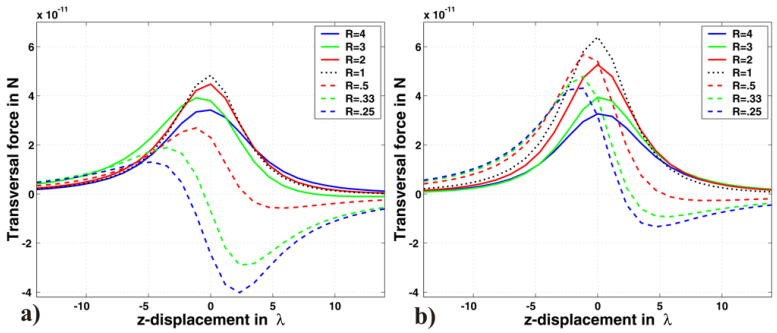

Figure 4: Transversal force along $\mathbf{x} = -\mathbf{0.44}\lambda$ on a dielectric elliptical cylinder with $\mathbf{r_{Ref}} = \mathbf{0.5}\lambda$, assuming a) a TE-polarized and b) a TM-polarized Gaussian beam for illumination.

power of $100mW$. First of all, no pronounced difference exists between TE and TM polarization. It can be seen that the force always has a maximum close to the waist of the laser beam and the force pushes the particle along the optical axis, it is always positive. The strength of the force is in the range of a tens of pico Newtons. No uniform trend can be seen in the dependence between the elongation and the strength of the force, due to multiple reflections of the light within the structure. Such a trend will appear if the particles are smaller, because the light that encounters the multiple reflections suffers from substantially smaller phase delay. For the particles with a reference radius of half of the wavelength, the force is strongest for the circular cylinder independent of the polarization.

The transversal force at a small distance from the optical axis (the value for the distance was chosen somewhat arbitrary to be $x = -0.44\lambda$) is shown for the particles in Fig. 4 a for TE and 4 b for TM polarization. Again, no pronounced difference can be seen for the two polarizations. A positive force means that the particles are attracted towards the optical axis, a negative one corresponds to a repulsion. It can be seen in both figures that particles elongated perpendicular to the optical axis are always attracted, while particles elongated in the opposite direction are attracted before and repelled approximately after the waist. The most elongated of these particles are already repelled somewhat before the waist. The effect is more pronounced using TE-polarized light.

The entire force distribution for the two most elongated particles (one transverse with $r_1 = \frac{0.5\lambda}{\sqrt{4}}$ and one longitudinal with $r_1 = 0.5\lambda\sqrt{4}$) assuming TE

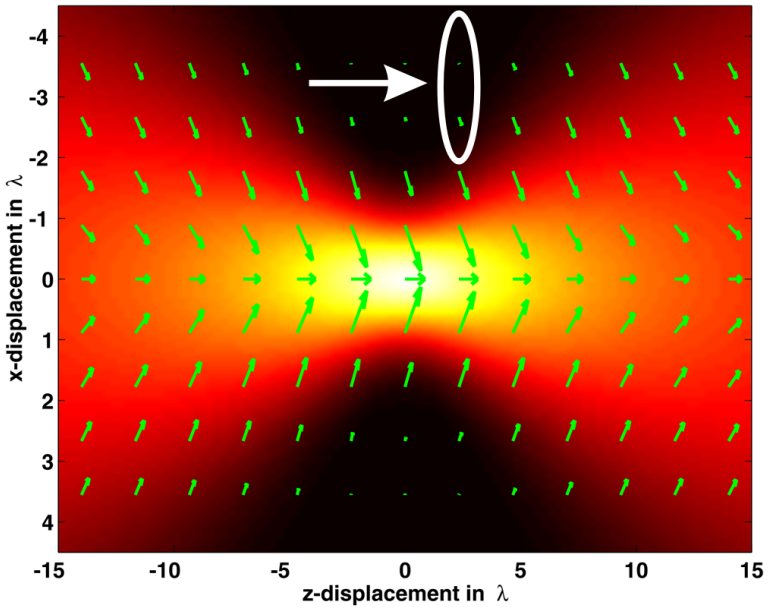

Figure 5: Force acting on a dielectric elliptical cylinder of transversal elongation ($\mathbf{r_1} = \frac{\mathbf{0.5}}{\sqrt{\mathbf{4}}}\lambda$).

polarization is shown in Fig. 5 and 6. The length of the arrows is not linearly proportional to the force in order to emphasize the direction of the force. The amplitude of the illumination beam is also shown in the figures and it propagates along the positive z-axis and in the insets of the figures the geometry of the particle with respect to the illumination direction is shown. Obviously the effect of attraction or repulsion is not restricted to a region close to the optical axis. Particles elongated parallel to the optical axis are repelled if they are located behind of the beam waist. For an explanation of this effect we have performed simulations using Finite Difference Time Domain (FDTD)[36]. Such a numerical technique is useful for the observation of a single diffraction process assuming illumination with a Gaussian beam as the computational time is smaller compared to the MMP. A spatial discretization of $\frac{\lambda}{20}$ was used for the numerical grid and the center of the particle was positioned at $x = -1\lambda$ relative to the beam axis and at $z = 4.5\lambda$ relative to the waist of the laser ($\omega = \lambda$). As boundaries of the computational domain perfectly matched layers were used[37].
Figure 7 a shows the intensity of the field when illuminating a particle elon-

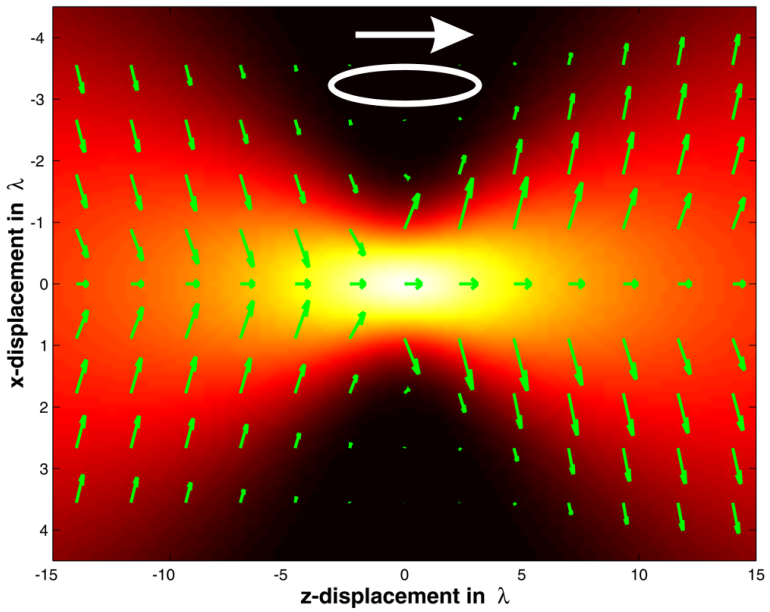

Figure 6: Force acting on a dielectric elliptical cylinder of longitudinal elongation ($\mathbf{r_1} = \mathbf{0.5}\sqrt{\mathbf{4}}\lambda$).

gated perpendicular and Fig. 7 b for a particle parallel to the optical axis. By examining the time-resolved field propagation as well as the resulting intensity distributions after the diffraction process, we see in Fig. 7 a that the light hitting the first surface of the particle is refracted and refracted once again upon exiting the other side. Because the long side of the particle is exposed to the incoming light, a large amount of light is deflected and the light which passes through the particle propagates away from the optical axis. Due to momentum conservation, as used as in the ray-optical model, momentum must be transferred to the particle and the direction of the impulse, which translates to a force and points in the opposite direction to the deflected beam. This means towards the optical axis, which explains why these elliptical objects are attracted towards this axis. In contrast, in Fig. 7 b a large amount of light is scattered at the surface due to the grazing incidence, since the intensity of the illuminating beam is higher on the side at the particle closest to the optical axis. The majority of the light is deflected by the structure towards the optical axis, thus pushing the particle away. Elliptical particles elongated along the optical axis are repelled if they are

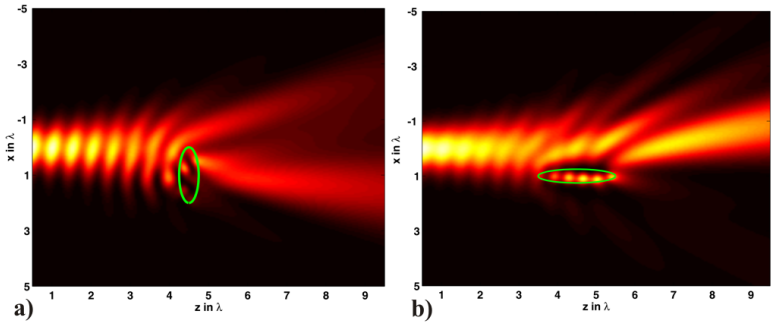

Figure 7: Intensity distribution upon illuminating an elliptical particle elongated in a) perpendicular and in b) parallel to the optical axis with a Gaussian beam.

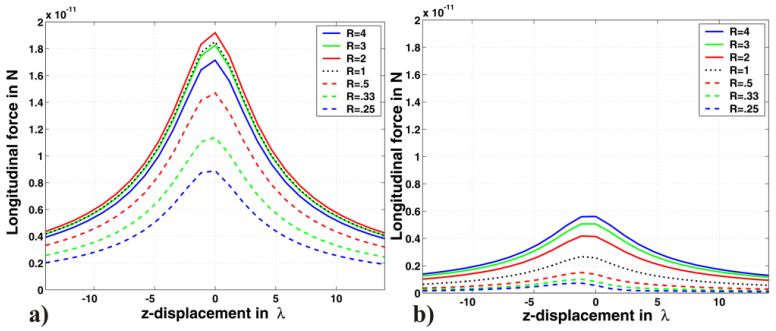

Figure 8: Longitudinal force on a dielectric elliptical cylinder on the axis with $\mathbf{r_{Ref} = 0.1\lambda}$ assuming a) a TE-polarized and b) a TM-polarized Gaussian beam for illumination.

positioned behind the waist.

4 Small dielectric particles in air

Such a pronounced difference in the response (e.g. a different sign of the transversal force) is significantly reduced if the size of the particles is smaller. The longitudinal force on the elliptical particles with the same axis ratios but now with a reference radius of $r_{Ref} = 0.1\lambda$ is shown in Fig. 8 a for TE and in Fig. 8 b for TM-polarized light. All the other parameters are the same as above.

For TE-polarized light the qualitative distribution of the force that acts on

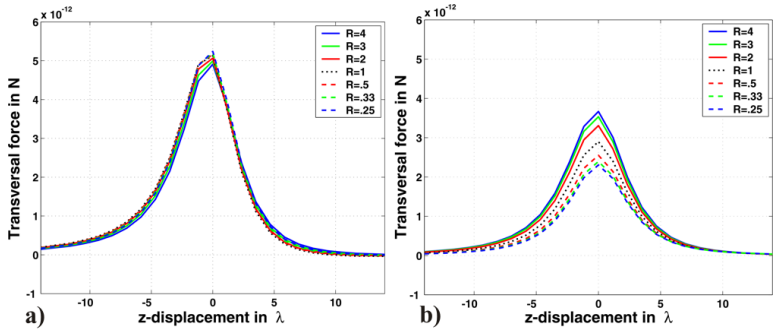

Figure 9: Transversal force along along $\mathbf{x} = -\mathbf{0.44}\lambda$ on dielectric elliptical cylinder with $\mathbf{r_{Ref}} = \mathbf{0.1}\lambda$ assuming a) a TE-polarized and b) a TM-polarized Gaussian beam for illumination.

the particles is nearly the same for the elongation directions. If one would plot the force normalized with respect to its maximum, all lines coincide to a good approximation. Only the strength varies, which has its maximum for the particle whose radius r_1 is divided by a factor of $\sqrt{2}$, having an ellipticity of 2. If the objects are illuminated with TM polarized light, the particle with the highest longitudinal force is the particle with a radius $r_1 = \frac{0.1}{\sqrt{4}}\lambda$. For a larger radius r_1, the maximum of the force is smaller. By comparing qualitatively the forces that act on the particles we see that the forces before the waist have an equal distribution independent of the particles elongation. Behind the waist, the force decreases more rapidly for an elongation in the longitudinal direction.

The reduced influence of the shape on the force can be likewise seen in Fig. 9 a for TE polarization and in Fig. 9 b for TM polarization, where the transversal force along the line $x = -0.44\lambda$ is shown. It can be seen that the force for the TE-polarized Gaussian beam illumination is the same, regardless of the elongation direction. Comparing the results for TE with those of TM polarization we see a difference, because the forces acting on the differently elongated particles are different in strength for TM polarization. This effect is attributed to the dominance of a dipole excitation within the structure and will be more pronounced for much smaller particles.

Comparing the transversal and longitudinal forces we see that the strength for the transversal force is approximately a quarter of the strength of the longitudinal force for TE polarization and only half for TM polarization. In both cases this means that the particle is pushed towards the optical axis.

A further reduction of the particle size will reduce the dominance of the scattering force component and will hence enhance the influence of the gradient force acting on the particle. As outlined in the introduction, the particles can be described by a simple dipole model and the force acting on the object can be decomposed into a gradient and scattering force. The gradient force will point towards the gradient of the square of the absolute value of the electric-field. For a spherical cylinder the z-component of the gradient force along the axis will equal at a certain radius the z-component of the scattering force. If such a condition is fulfilled, a point exists in space with a net force acting on the particle equal to zero. This is a point in which the particle can be trapped. Assuming TE-polarization, the necessary radius for the particle to be trapped is $r = 0.018\lambda$. For TM polarization the radius is nearly twice as large, $r = 0.034\lambda$. For the parameters used throughout the text the particle is stably trapped at $z = 2.9\lambda$.

5 Dielectric particles much smaller than the wavelength in air

For particles smaller than this critical radius the longitudinal force along the optical axis has two points where it is zero. But only at one point that is closer to the waist the particle can be trapped stably. The other point is an unstable.

Figure 10 a shows the longitudinal force acting on the elliptical particles with a reference radius of $r_{Ref} = 0.01\lambda$ for TE-polarized light and in Fig. 10 b for TM-polarized light. It can be seen that the longitudinal force that acts on the particle becomes independent of the elongation direction for TE polarization. For TM polarization the longitudinal force has a constant ratio, which depends on the axis ratio.

For an explanation of this different behavior, we derive the longitudinal force on an elliptical cylinder in the quasi-static limit for the two polarizations. We will restrict ourselves to plane wave illumination because this is sufficient to explain the different behavior.

In this case the longitudinal force is equal to the scattering force, because the gradient of the square of the absolute value of the electric field is zero.

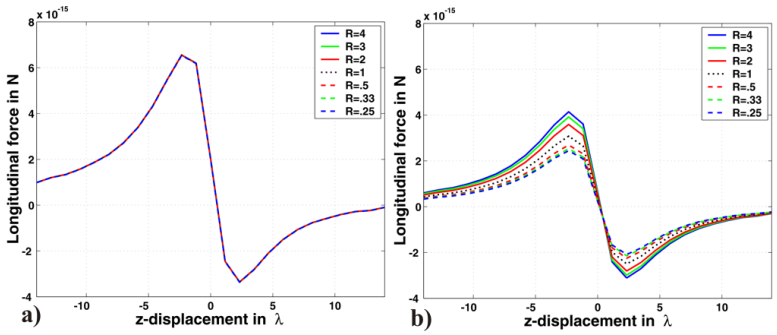

Figure 10: Longitudinal force on dielectric elliptical cylinder on the axis with $\mathbf{r_{Ref}} = \mathbf{0.01}\lambda$ assuming a) a TE-polarized and b) a TM-polarized Gaussian beam for illumination.

The scattering force is given by[7]

$$F_{scat}(\mathbf{r}) = \frac{C_{sca}\langle \mathbf{S}(\mathbf{r},t)\rangle_T}{c/n_a} = \hat{z}\left(\frac{n_a}{c}\right) C_{sca}\mathbf{I}(\mathbf{r}). \tag{4}$$

$\mathbf{I}$ is the intensity, c is the speed of light in vacuum, $\mathbf{S}$ is the Poynting vector and C_{sca} is the scattering cross section.
The scattering cross section for an ellipsoid with the semi-axes r_1, r_2 and r_3 approximation is given by in the dipole [38]

$$C_{sca} = \frac{k^4}{6\pi} \mid \alpha_i \mid^2, \tag{5}$$

with α_i being the polarizability for the axis i. It is defined as[38]

$$\alpha_i = 4\pi r_1 r_2 r_3 \frac{\epsilon_p - \epsilon_s}{3\epsilon_s + 3L_i(\epsilon_p - \epsilon_s)} \qquad i = 1, 2, 3. \tag{6}$$

ϵ_p and ϵ_s are the dielectric constants of the particle and of the surrounding medium, respectively. L_i is the so-called geometrical factor and is defined as

$$L_i = \frac{r_1 r_2 r_3}{2} \int_0^\infty \frac{ds}{(s + r_i^2) f(s)}, \tag{7}$$

with

$$f(s) = \sqrt{(s + r_1^2)(s + r_2^2)(s + r_3^2)}. \tag{8}$$

In the limit of a cylindrical structure, one of the three radii tends to infinity. In the case of TE polarization, the field oscillates parallel to this radius (the cylinder axis) and the geometrical factor becomes zero independent of the ratio of the two other axes. For TM-polarized light the electric field oscillates along the elliptical cross section of the structure. In the limit of an infinite third radius the geometrical factor L_i becomes $\frac{1}{1+R}$ for the first axis and $\frac{R}{1+R}$ for the second axis.
For TE polarization the polarizability becomes independent of the axis ratio

$$\alpha = V\frac{\epsilon_p - \epsilon_s}{\epsilon_s}, \tag{9}$$

with V being the volume. In TM polarization the polarizability becomes

$$\alpha = V\frac{(\epsilon_p - \epsilon_s)(1+R)}{R\epsilon_s + \epsilon_p}. \tag{10}$$

Figure 11 shows the normalized longitudinal force on elliptical particles with different axis ratios and different sizes. The particles have been illuminated with a TM-polarized plane wave. Additionally, the force as evaluated with the Eqn. 4 is shown. It can be seen that the force that acts on the particle for smaller sizes converges quite well to the force calculated using the dipole approximation.
For more complex wave fields the gradient force has to be taken into account. This force component in the dipole approximation can be calculated using[9] as

$$F_{grad} = \frac{1}{4}n_a\ \alpha\ grad(\mid E \mid^2). \tag{11}$$

The dependence on the polarizability indicates that the gradient force becomes independent of the elongation of the particles for TE polarization and the force will become a fixed ratio that depends on the axis ratio for TM polarization. This can be seen in the calculation of the transversal force. This force depends only on the gradient force. Figure 12 a shows the force evaluated along $x = -0.44\lambda$ for TE polarization and Fig. 12 b for TM polarization, for a reference radius of $r_{Ref} = 0.01\lambda$. All the other parameters are the same. The force is strongest at the spatial point with the highest gradient of the field, in the waist and is always positive. This means that these particles are always attracted towards the optical axis.
For completeness, Fig.13 shows the entire force that acts on a circular cylinder with a radius of $r = 0.01\lambda$ assuming TE-polarized light for the illumination.

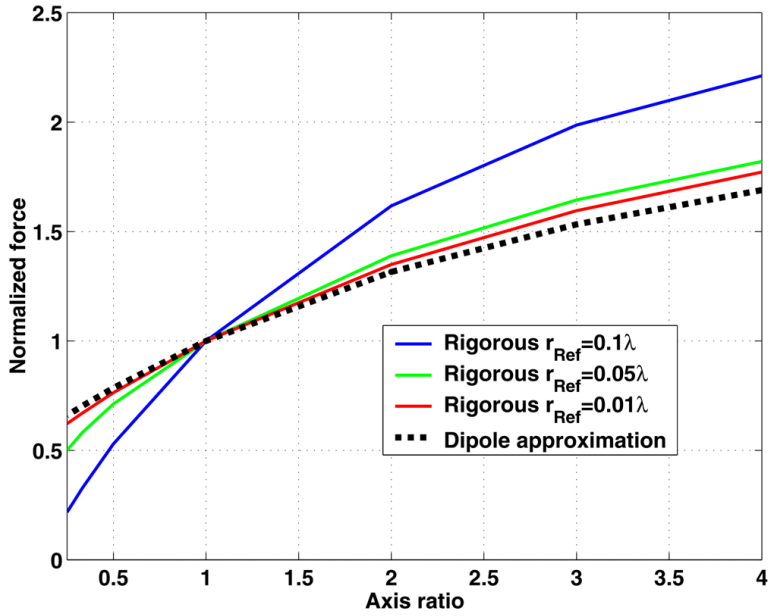

Figure 11: Normalized force on elliptical particles for plane wave illumination (TM polarization).

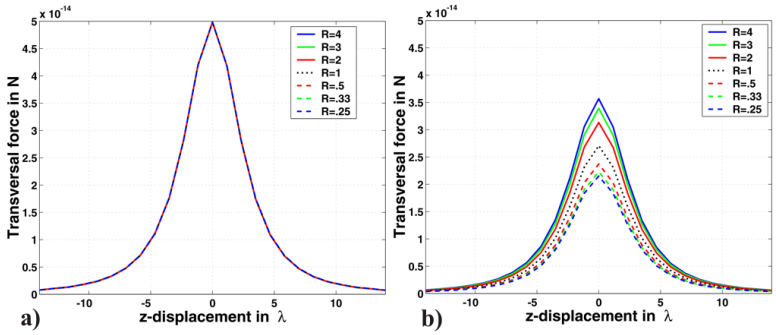

Figure 12: Transversal force along $\mathbf{x} = -\mathbf{0.44}\lambda$ on dielectric elliptical cylinder with $\mathbf{r_{Ref}} = \mathbf{0.01}\lambda$ assuming a) a TE-polarized and b) a TM-polarized Gaussian beam for illumination.

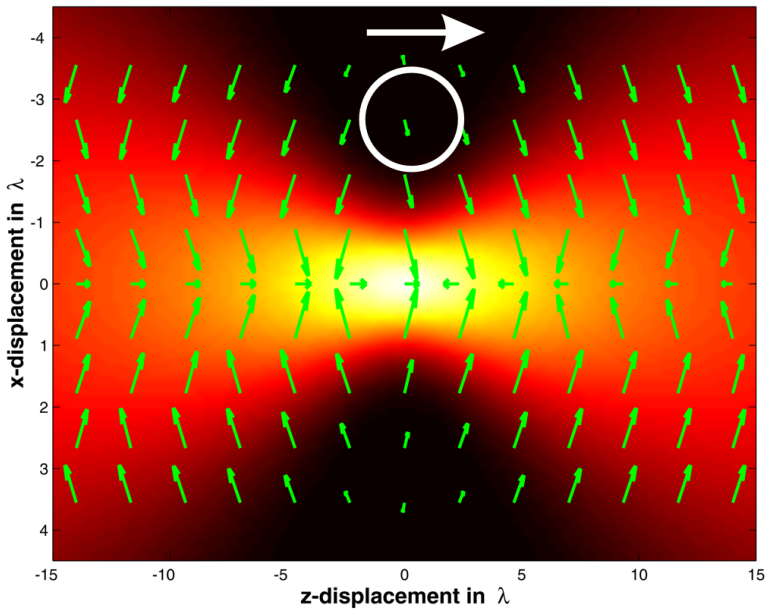

Figure 13: Force acting on a dielectric circular cylinder with $\mathbf{r} = \mathbf{0.01}\lambda$ for TE polarization.

The force is shown on a non-linear scale to emphasize the direction. The amplitude of the illuminating beam is also included as the color scale to the figure. It can be seen that in this size regime the gradient force is dominant over the scattering force. The contribution of the scattering force is negligible and the force is to a good approximation equal to the gradient of the square of the absolute value of the E-field.
Even though all the calculations have been done with a high index contrast, the basic effects and different interaction regimes remain essentially the same for a lower index contrast. The only difference at an index contrast close to unity is that the dipole approximation is valid for larger geometrical radii.
If the index contrast is lower than unity, meaning that the refractive index of the surrounding medium is larger than the index of the cylinder, a different behavior is observed. In an experiment this situation corresponds to e.g. air bubbles in a liquid. This case will be investigated in the next section.

6 Particles with an index contrast lower than unity

In this section we will assume an index of 1.5 for the surrounding medium and an index of 1 for the medium of the cylinder. All the other parameters remain the same. The waist remains equal to a single wavelength in vacuum. In Fig. 14 is shown the entire force distribution for a particle elongated perpendicular to the optical axis and whose reference radius is $r_{Ref} = 0.5\lambda$. This means $r_1 = \frac{0.5\lambda}{\sqrt{4}}$. The amplitude of the illuminating beam has been added to the figure, the polarization is TE and the force is shown on a nonlinear scale. It can be seen that the force acting on such a particle will always repel it from the axis if it is elongated transversally. The effect is well known and can be explained in a simple manner by analyzing the polarizability α in such a configuration. The terms $(\epsilon_p - \epsilon_s)$ and α take negative values. Consequently, the gradient force is negative and points away from the optical axis. For the calculation of the scattering force, the absolute value of α is taken into account and the force is consequently positive, pointing in the propagation direction of the beam.

Fig. 15 shows the entire force distribution for an elliptical particle elongated parallel to the optical axis, thus $r_1 = 0.5\lambda\sqrt{4}$. Only for such highly elongated particles in the longitudinal direction, the particles are attracted towards the optical axis when it is placed before the waist of the beam. In a similar manner to the explanation in the last section, for such a highly longitudinally elongated particle, the deflection rather than refraction of the laser beam at the elongated surface will lead to a propagation of the beam away from the optical axis. Due to conservation of momentum, the particle is pushed towards the axis. The basic behavior of these particles is exactly the same as we have analyzed already for the dielectric particles in air. The difference is the opposite sign of the transversal force and the corresponding opposite behavior of attraction and repulsion when placing it before or behind the laser beam.

A point of stable trapping in 3D for such a configuration is not possible. The on-axis longitudinal force may be negative if the particle is sufficiently small, but the transversal force will always push the particle away from the optical axis, hence there are only unstable points on the optical axis. In Fig.16 a the longitudinal force along the axis for particles with different elongations is shown for TE polarization and in Fig.16 b for TM polarization. The reference

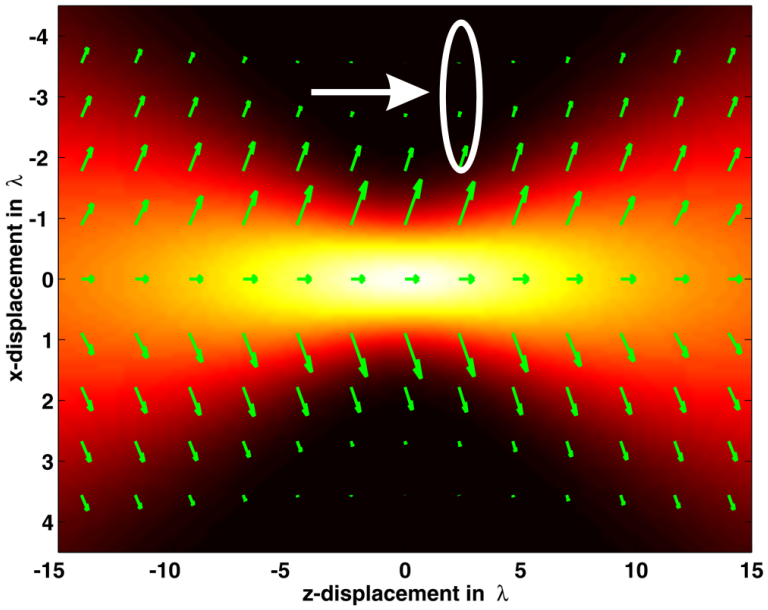

Figure 14: Force acting on a dielectric elliptical cylinder, transversally elongated ($\mathbf{r_1} = \frac{\mathbf{0.5}}{\sqrt{\mathbf{4}}}\lambda$) with $\mathbf{n_a} = \mathbf{1.5}$.

radius of the elliptical cylinder is $r_{Ref} = 0.01\lambda$. It can be seen that the force becomes independent of the elongation for TE-polarized light, as suggested by the calculated polarizability using Eqn.9. The force has its maximum at a position somewhat behind the waist.
On the other hand the force on the particle for a TM-polarized wave depends on the shape because the polarizability is shape-dependent as given by Eqn. 10. The force is strongest for particles elongated in the longitudinal direction. The radius r_1 of this particle is $r_1 = 0.01\sqrt{4}$. Such a tendency is confirmed by using the dipole model.
For completeness we show in Fig.17 a and in Fig.17 b the transversal force that acts on the particle elongated parallel to the optical axis at $x = -0.44\lambda$ for TE polarization and for TM polarization, respectively. The force is negative, which means that the particles are repelled from the optical axis. For TE polarization the force is independent of the particle elongation.
If the aim is to attract these particles towards the optical axis, it is well known that higher-order Gauss-Laguerre modes in 3D and Gauss-Hermite modes in 2D can be used[6, 39]. The decomposition of the illuminating beam into a

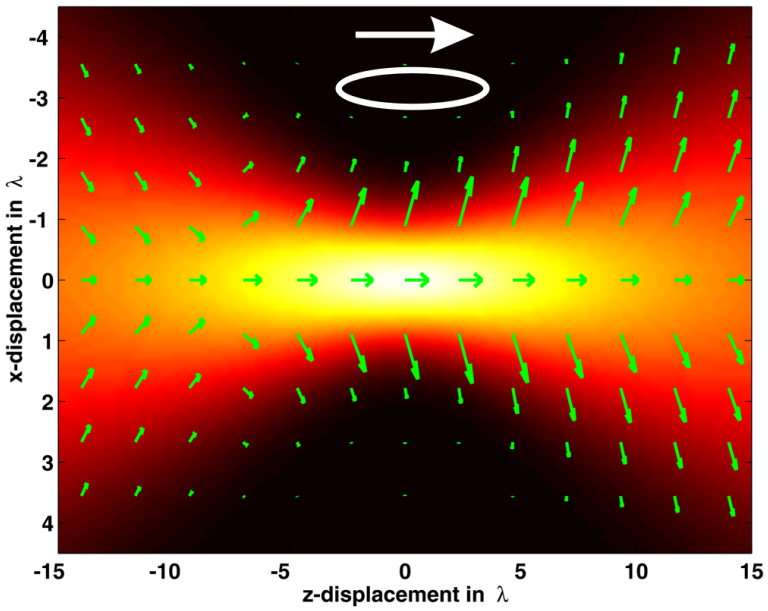

Figure 15: Force acting on a dielectric elliptical cylinder, longitudinally elongated ($\mathbf{r_1} = \mathbf{0.5}\sqrt{\mathbf{4}}\lambda$) with $\mathbf{n_a} = \mathbf{1.5}$.

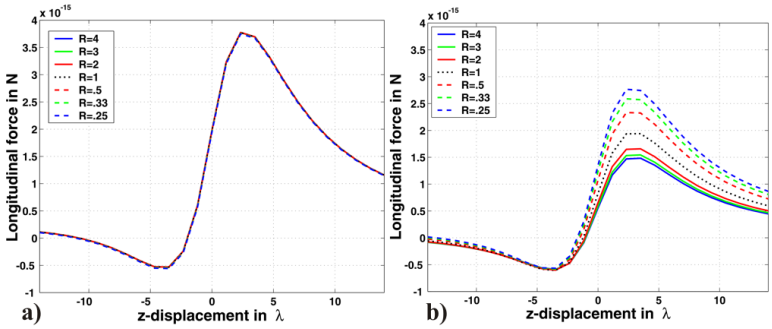

Figure 16: Longitudinal force on dielectric elliptical cylinder on the axis with $\mathbf{r_{Ref}} = \mathbf{0.01}\lambda$ assuming a) a TE-polarized and b) a TM-polarized Gaussian beam for illumination with $\mathbf{n_a} = \mathbf{1.5}$.

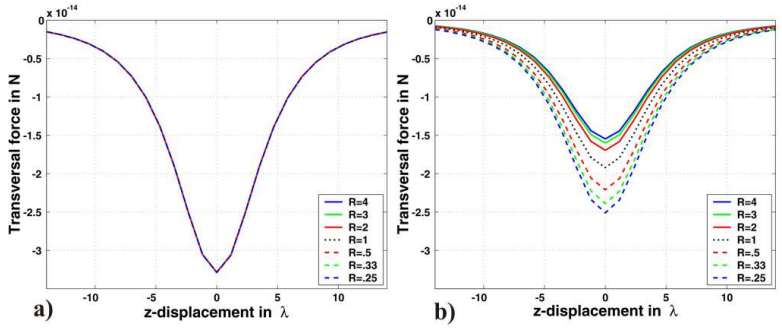

Figure 17: Transversal force along $\mathbf{x} = -\mathbf{0.44}\lambda$ on dielectric elliptical cylinder with $\mathbf{r_{Ref}} = \mathbf{0.01}\lambda$ assuming a) a TE-polarized and b) a TM-polarized Gaussian beam for illumination with $\mathbf{n_a} = \mathbf{1.5}$.

plane wave spectrum in the computational procedure, permits an efficient evaluation of the response of the structure to different illumination beams. In Fig.18 we show the force that acts on an circular cylinder with a radius of $r = 0.5\lambda$ with a Gauss-Hermite beam of order 1. The force is shown again on a non-linear scale to emphasize the direction. It can be seen that the particle will react to the local gradient of the field, which pushes the particle towards the optical axis as long as it is spatially confined to the central part of the beam.

7 Conclusions

In this paper applied rigorous methods for the investigation the force on dielectric elliptical cylinders as a function of the elongation direction within different size domains. We have analyzed the behavior for different index contrasts.

It has been shown that geometrically large elliptical particles with an index contrast larger than unity and elongated in the transversal direction are always attracted towards the optical axis, whereas particles elongated in the longitudinal direction are attracted if they are positioned before the waist of the laser beam and repelled if positioned after the waist. An explanation was given by analyzing the process of the interaction, which is dominated in the different regimes by either refraction or reflection, depending on the

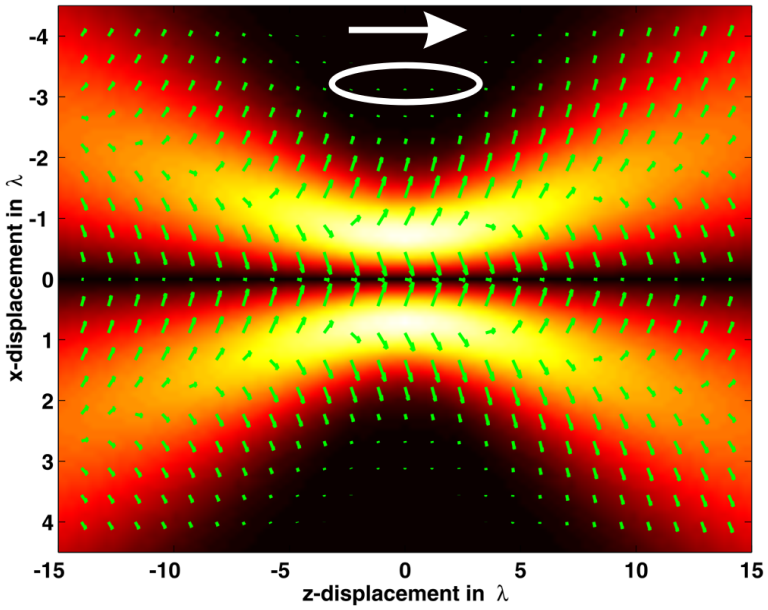

Figure 18: Force acting on a longitudinally elongated dielectric elliptical cylinder ($\mathbf{r_1} = \mathbf{0.5}\sqrt{\mathbf{4}}\lambda$) with $\mathbf{n_a} = \mathbf{1.5}$, illuminated with a GH1 beam.

elongation direction of the particle relative to the optical axis.
If the particles are much smaller than the wavelength, the force can be decomposed assuming a dipole model into a scattering component which points in the propagation direction of the laser beam and a gradient force. The gradient force points towards the gradient of the square of the absolute value of the electric field. For a Gaussian beam this force will point towards the waist. If the z-component of the gradient force equals the scattering force, stable trapping in three dimensions becomes possible. By using the dipole model as well as our rigorous simulations, it was shown that for TE-polarized light the force becomes independent of the elongation. In contrast, for the TM polarization the force will converge towards a fixed ratio that depends on the axis ratio.
Similar investigations have been made for systems with an index contrast lower than unity. In these systems the sign of the gradient force is negative. The gradient force hence will point in the opposite direction to the gradient of the field. This results in a repulsion from the optical axis for large transversal elongated particles independent of their position relative to the

waist. Longitudinally elongated particles can be attracted if they are positioned before the waist, otherwise their are likewise repelled. For particles much smaller than the wavelength the same dependence of the response as a function of the polarization was found as for dielectric particles in air. For TE-polarized light the force does not depend on the elongation, whereas for TM polarization it does. These particles cannot be stably trapped because the gradient force will always point away from the optical axis. For an on-axis trapping it is necessary to use higher order Gauss-Hermite laser modes, as we have shown numerically.
The differing response of particles with different ellipticities, allows the potential application to sort particles as a function of their shape. For example it is still problematic to fabricate particles with a controlled axis ratio, while statistical approaches such as irradiation with pulsed laser beams to deform particles yield a mixture of particles with different shapes. In this situation, the application of a sorting mechanism with optical tweezers could be a promising technique to obtain particles with a well controlled shape[40].

8 Acknowledgments

This research was supported by the European Union within the framework of the Future and Emerging Technologies-SLAM program under grant No. IST-2000-26479.

References

[1] Ashkin A 1970 *Phys. Rev. Lett.*, **24** 156

[2] Ashkin A and Dziedzic J M 1971 *Appl. Phys. Lett.*, **19** 283

[3] Grier D G 2003 *Nature*, **424** 810

[4] Ashkin A 1997 *Proc. Natl. Acad. Sci. USA*, **94** 4853

[5] Ashkin A, Dziedzic J M, Bjorkholm J E and Chu S 1986 *Opt. Lett.*, **11** 288

[6] Gahagan K T and Swartzlander Jr. G A 1998 *J. Opt. Soc. Am. B*, **15** 524

[7] Harada Y and Asakura T 1996 *Opt. Commun.*, **124** 529

[8] Lewittes M, Arnold S and Oster G 1982 *Appl. Phys. Lett.*, **40** 455

[9] Kawata S, Inouye Y and Sugiura T 1994 *Jpn. J. Appl. Phys.*, **33** L 1725

[10] Arias-Gonzáles J R and Nieto-Vesperinas M 2003 *J. Opt. Soc. Am. A*, **20** 1201

[11] Nieminen T A, Rubinsztein-Dunlop H, Heckenberg N R and Bishop A I 2001 *Computer Physics Communications*, **142** 468

[12] Gouesbet G and Gréhan G 2000 *Atomization and Sprays*, **10** 277

[13] Gouesbet G, Maheu B and Gréhan G 1980 *J. Opt. Soc. Am. A*, **5** 1427

[14] Barton J P, Alexander D R and Schaub S A 1989 *J. Appl. Phys.* **66** 4594

[15] Onofri F, Grehan G and Gouesbet G 1980 *J. Opt. Soc. Am. A*, **34** 7113

[16] Mees L, Ren K F, Gréhan G and Gouesbet G 1999 *Appl. Opt.*, **38** 1867

[17] Gouesbet G and Mees L 1999 *J. Opt. Soc. Am. A*, **16** 1333

[18] Ren K F, Gréhan G and Gouesbet G 1999 *Opt. Comm.*, **108** 343

[19] Lock J A 2004 *Appl. Opt.*, **43** 2532

[20] Lock J A 2004 *Appl. Opt.*, **43** 2544

[21] Polaert H, Gréhan G and Gouesbet G 1998 *Opt. Comm.*, **155** 169

[22] Bayoudh S, Nieminen T A, Heckenberg N R and Rubinsztein-Dunlop H 2003 *Journal of Modern Optics*, **50** 1581

[23] Chaumet P C and Nieto-Vesperinas M 2000 *Phys. Rev. B*, **61** 14119

[24] Prather D W, Mirotznik M S and Mait J N 1997 *J. Opt. Soc. Am. A*, **14** 34

[25] Rockstuhl C, Salt M and Herzig H P 2003 *J. Opt. Soc. Am. A*, **20** 1969

[26] Hafner C 1999 *Post-Modern Electromagnetics*, (John Wiley & Sons)

[27] Saleh B and Teich M 1991 *Fundamentals of Photonics*, (John Wiley & Sons)

[28] Jackson J D 1975 *Classical Electrodynamics*, (John Wiley & Sons)

[29] Wang X, Wang X B and Cascoyne P R C 1997 *Journal of Electrostatics*, **39** 277

[30] Arias-Gonzáles J R, Nieto-Vesperinas M and Lester M 2002 *Phys. Rev. B*, **65** 115402

[31] Lester M and Nieto-Vesperinas M 1999 *Opt. Lett.*, **24** 936

[32] Rockstuhl C, Salt M and Herzig H P submitted to *J. Opt. Soc. Am. B*

[33] Moreno E, Erni D E, Hafner C and Vahldieck R 2002 *J. Opt. Soc. Am. A*, **19** 101

[34] Hafner C 1990 *The Generalized Multipole Technique for Computational Electromagnetics*, (Artech House Books)

[35] Mie G 1908 *Ann. Physik*, **25** 377

[36] Taflove A and Hagness S C 2000 *Computational Electrodynamics*, (Artech House Publishers)

[37] Berenger J P 1994 *J. Comput. Phys.*, **114** 185

[38] Wang D, Guo S, Ren H and Yin S 2002 *Opt. Lett.*, **27** 992

[39] He H, Heckenberg N R and Rubinsztein-Dunlop H 1995 *J. of Mod. Opt.*, **42** 217

[40] MacDonald M P, Spalding G C and Dholakia K 2003 *Nature*, **426** 421

Calculation of the torque on dielectric elliptical cylinders

Carsten Rockstuhl and Hans Peter Herzig

University of Neuchâtel, Institute of Microtechnology,
Rue Abraham-Louis Breguet 2, CH-2000 Neuchâtel, Switzerland

July 16, 2004

Abstract

We present our investigation of the torque exerted on dielectric elliptical cylinders by highly focused laser beams. The calculations are done using rigorous diffraction theory and the size-dependent torque is analyzed as a function of the axis ratio. It is found that highly elongated particles will experience a reversal of the torque for a radius that is approximately one third of the wavelength. This effect is attributed to interference effects inside the structure due to multiple reflections of the incoming wave. The evolution from a perfectly sinusoidal angular dependency of the torque to a more complicated pattern for increasing particle size is presented in detail.
OSICS codes: 290.5850, 260.2110

1 Introduction

Since the pioneering work of Ashkin in the seventies[1, 2, 3], the optical force and torque exerted on particles by optical wave-fields became a subject of intensive research due to the fascinating physics and interesting potential applications. The force on dielectric particles basically leads to an acceleration of the particles in the propagation direction of the beam and to an attraction towards the optical axis if the particles are sufficiently large compared to the wavelength[4]. Numerical computation of the behavior in this size regime can be done efficiently by using a technique based on geometrical optics[5]. A characterization of the force on particles that are much smaller than the wavelength can be done by using a dipole approximation[6]. Within the approach, the entire force is decomposed into a scattering and a gradient component. The scattering component points in the propagation direction of the incoming beam and the gradient force in the direction of the gradient of the square of the absolute value of the electric field. For highly focused laser beams, this component of the force will point correspondingly to the waist of the beam. If the z-component of the gradient force equals the scattering force, a stable trapping of particles in three dimensions is possible. Such an optical tweezer can be used for applications such as scanning near-field optical microscopy, in which a trapped particle serves as a highly localized near-field probe[7] or for photonic force microscopy[8].
Another interesting possibility is to rotate the particles by exploiting the torque applied to them, using various mechanisms[9]. One approach is to use directly the properties of the illuminating wave field, such as the orbital angular momentum of the beam[10] (associated with helical phase fronts) or its spin angular momentum[11] (associated with circular polarization).
Another mechanism for the rotation of a particle is its non-spherical geometry, causing an alignment of the particle relative to the laser beam, as was demonstrated in some recent experiments[12, 13, 14]. The fascinating exploitations of the torque exerted on micro-particles in applications such as the construction of micro-machines driven by light[15, 16] or as a possible micro-rheometer[17] motivated some researchers to analyze the torsion of particles not only experimentally but also theoretically[5, 12, 18]. However, due to the complex calculations required, only the specific experimental configurations were normally treated numerically, in order to compare theory and experiment. In most cases, particles with a size significantly smaller than the optical wavelength have been analyzed, meaning effects that appear if

the size of the particles is comparable to the wavelength were not discussed. In this article we present a detailed analysis of the torque on dielectric cylinders with an elliptical cross-section for different size domains. The structures are essentially two-dimensional, and thus invariant in the third dimension. We have analyzed such a geometry because the necessary solution of the three-dimensional scattering problem would exceed a reasonable computation time, as well as memory size. However, the main effects that appear in a two-dimensional simulation will be qualitatively comparable to the three-dimensional case.
The particles positioned in the x-z-plane are illuminated with a highly focused Gaussian beam. As given by the dipole model, for very small elliptical particles the exerted torque shows a perfectly sinusoidal dependence on the angle between the optical axis and the axis of the particle. In this size domain the torque has a different sign for the different polarizations. For TM polarization (the magnetic field oscillates parallel to the infinite cylinder axis in the y-direction) the particles will be aligned along the major axis, whereas for TE polarization (the electric field oscillates parallel to the infinite cylinder axis in the y-direction) along the minor axis. For increasing the size, an inversion of the sign appears for highly elongated particles. For particles having a size comparable to the wavelength, the torque response becomes quite complex and different angles exists for which the particles are rotationally stably trapped, having zero net torque.

2 Computational procedure

The computational procedure basically consists of two steps. First, the complex field distribution along the surface of the particle is calculated using rigorous diffraction theory. In the special case of a sphere in 3D or a circular cylinder in 2D, Mie-theory can be used as a quasi analytical solution for the problem[19]. For deviating geometries Nieminen et al. used the T-Matrix method to calculate the torque on the particles[20]. We will use the Multiple Multipole Method (MMP) for the solution of the diffraction process[21], which is comparable to the T-Matrix method. The Multiple Multipole Method was used in the past by Novotny and co-workers to model the near-field interaction of very small particles with the tip of a scanning near-field microscope that was used as an optical tweezer on a nanometric

length scale[22]. They also presented a calculation of the torque on a very small elliptical particle. However, these calculations were done only for a single specific example.

In the MMP the field in regions with a homogenous dielectric constant is expanded in modes, which are an analytical solution of the wave equation. The amplitude of the modes are optimized in a least-square sense such that the boundary conditions, the continuity of the field and its derivative across the boundary between two regions with a homogenous dielectric constant, are fulfilled. In the present work we have used Hankel functions of the first order with 5 expansion terms as the basis for the mode expansion and overall 75 multipoles[23]. The surface was sampled using 500 points. The multipoles that describe the field inside the particles are positioned somewhat behind the boundary, in the surrounding medium, and the multipoles describing the scattered field are positioned within the particle. This is done in order to avoid the singularities of the field associated with the origins of the multipoles.

The illuminating beam was decomposed into 41 plane waves. This allows the calculation of the field across the particle at an arbitrary point in space by a subsequent superposition of the plane wave response, multiplied by the amplitude of the Fourier transform of the illuminating wave field. This will lead to a reduction in computation time and the possibility of analyzing the force and torque on particles for different illuminating wave fields. If the particle is positioned at a point (x, z) relative to the center of the waist of the beam, the complex amplitude of the m-th order illumination plane wave is given by

$$A_m = \frac{e^{-i\sqrt{\frac{2\pi}{\lambda}-m\frac{2\pi}{\lambda}}z}}{\Lambda} \int_{-\frac{\Lambda}{2}}^{\frac{\Lambda}{2}} a_{Inc}(x) e^{-im\frac{2\pi}{\Lambda}x} dx, \tag{1}$$

with $a_{Inc}(x)$ being the amplitude distribution in the waist. The discretization will introduce a period of Λ in the illuminating beam. Usually, we have used a period of 20λ. This number was chosen to be sufficiently high such that interference of the illumination beam between adjacent periods is negligible. As the illumination field we have used a Gaussian beam given by

$$a_{Inc}(x) = E_0 \; exp\left(-\left(\frac{x}{\omega}\right)^2\right), \tag{2}$$

with E_0 being the beam amplitude. The amplitude was chosen to be $6.9V/m$, which corresponds to the amplitude of a three-dimensional beam with a

power of $100mW$. ω is the waist of the beam. Unless otherwise stated, we have chosen the beam waist to be equal to the wavelength.
In the second step of the calculation once the field across the surface of the particle is known, Maxwell's stress tensor $\widetilde{T}$ is then applied to calculate the force that acts on the particle, by integrating over the surface of the particle [24]

$$\mathbf{F} = \oint (\widetilde{T} \cdot \mathbf{n}) dA, \tag{3}$$

where $\mathbf{n}$ is the unit vector normal to the surface. At optical frequencies, only the time average of the electromagnetic force $\langle \mathbf{F} \rangle$ is observed. For a particle embedded in an isotropic medium the force is calculated as [25]

$$\begin{aligned} \langle \mathbf{F} \rangle &= \left\langle \oint (\widetilde{T} \cdot \mathbf{n}) dA \right\rangle \\ &= \int_S \left\{ \frac{\epsilon}{2} Re\left[(\mathbf{E} \cdot \mathbf{n}) \mathbf{E}^\star \right] - \frac{\epsilon}{4} (\mathbf{E} \cdot \mathbf{E}^\star) \mathbf{n} \right. \\ &\quad \left. + \frac{\mu}{2} Re\left[(\mathbf{H} \cdot \mathbf{n}) \mathbf{H}^\star \right] - \frac{\mu}{4} (\mathbf{H} \cdot \mathbf{H}^\star) \mathbf{n} \right\} dl', \end{aligned} \tag{4}$$

with ϵ being the dielectric constant of the surrounding medium, μ its permittivity and dl' the length of a line segment of the surface. The net radiation torque on the particle is calculated subsequently by[24]

$$\langle \tau \rangle = \left\langle \oint \mathbf{r} \times (\widetilde{T} \cdot \mathbf{n}) dA \right\rangle. \tag{5}$$

$\mathbf{r}$ is the vector between the element of integration on the surface and a reference point within the particle that is assumed to be the point around which the particle rotates. In the calculations we have used the center of the particle as the reference point. However, the exact point is not important as the calculated torque will be the same, regardless of the choice of position.
The particles used in the simulations have an elliptical cross section. The size of the major axis with the radius r_1, is the reference radius r_{Ref} multiplied by three different factors: $\sqrt{4}$, $\sqrt{3}$ and $\sqrt{2}$. The major axis is parallel to the propagation direction of the laser beam for an orientation of $\theta = 0^o$. For the other radius r_2, which is perpendicular to the optical axis, the reference radius r_{Ref} is divided by the same elongation factors in order to maintain a constant area for all of the particles. The classical mathematical sign convention is used throughout the text (e.g. a positive angle θ indicates a counterclockwise rotation of the particle). In the same way, a positive torque

will cause a rotational acceleration of the particle in the counterclockwise direction, a negative torque will cause a clockwise rotational acceleration of the particle. The refractive index was chosen to be 1.5 for the particles and they are embedded in air.
In the next section we will first present the size-dependent torque for a rotation angle of the particles of 45^o, to give an overall indication about the evolution of the torque. Subsequently we will discuss in detail the characteristics of the torque at different sizes. We analyze the difference in the behavior for particles with a size much smaller than the wavelength, intermediate sizes and particles with a size comparable to the wavelength.

3 Numerical results and discussion

3.1 Size dependence

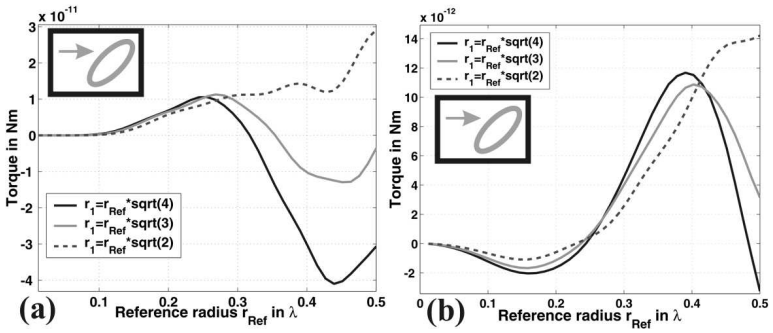

Figure 1: Torque on elliptical cylinders located at the center of the beam waist oriented at 45^o for (a) TE polarization and (b) TM polarization as a function of the size.

In Fig. 1a the torque on an elliptical cylinder for the three different elongations as a function of r_{Ref} is shown. The rotation angle θ is 45^o and we have assumed a TE-polarized beam for the illumination. The inset shows the particle orientation with respect to the propagation direction of the illuminating wave field. The particle is positioned at the center of the beam waist ($x = 0, z = 0$). The results for the same configuration but with a TM-polarized beam are shown in Fig. 1b.
The torque for TE polarization has a positive sign for very small particles, which will cause an alignment of the minor axis parallel to the propagation

direction of the beam. Increasing the size will cause a steady increase in the induced torque up to a particle radius of $r_{Ref} \approx 0.25\lambda$. For the two most elongated particles, increasing the size will cause a decrease in the strength of the torque. For these two particles this leads ultimately to a reversal of the torque direction. The torque exerted on the particle with an elongation factor of $\sqrt{2}$ continues on an upward trend. For a further increase of the size, the torque will increase again for all three particles, leading again to a change of sign for the two most elongated particles. As will be shown in the section on particles with a size comparable to the wavelength, an exact designation of the alignment direction for these larger particle sizes is not possible, because different rotation angles exist for which the net torque becomes zero.
For TM polarization, the overall behavior is comparable, except for a change in the sign of the torque. For particles much smaller than the wavelength, the torque is negative, which will cause an alignment of the particle with the major axis parallel to the propagation direction of the illuminating wave field. This is the orientation that one would expect from a simple dipole model. By increasing the size of the particles slightly, the torque becomes larger in magnitude with the same size, independent of the elongation. At a certain size of the particle, the strength of the torque becomes lower and a change of sign occurs at a size of $r_{Ref} \approx 0.25\lambda$. A further increase in the particle size will first cause an increase of the torque and then from a certain particle size the torque diminishes. The maximum of the torque for the two most elongated particles is at approximately a radius of $r_{Ref} = 0.4\lambda$ The change in the sign of the torque is attributed to the change in the polarization direction, as the electric field component has a dominant influence on the torque. For TE polarization the electric field will oscillate parallel to the cylinder axis and will have no component in the plane of rotation, such that it does not contribute to the torque in the dipole approximation.
In the following three subsections the torque for different size domains is analyzed as a function of the orientation as well as the spatial position of the particle within the illuminating wave field. In each of these domains the resulting torque shows different characteristic features. The size domains to be investigated are: particles much smaller than the wavelength, particles with a size comparable to the wavelength and particles with a size between the two (called the intermediate region).

3.2 Particles much smaller than the wavelength

The influence of the electric field can be seen by comparing the strength of the torque exerted on the particles for the two linear polarizations, if the particles are very small compared to the wavelength. In this size domain the field scattered of the particle is basically given by the field of a dipole. In Fig.

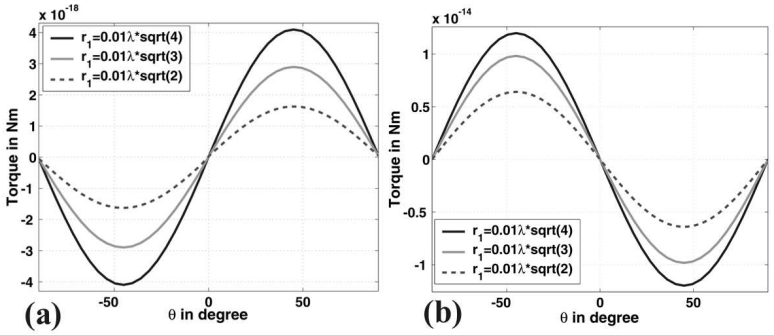

Figure 2: Torque on elliptical cylinders much smaller than the wavelength ($r_1 = 0.01\lambda$) as a function of the orientation for (a) TE polarization and (b) TM polarization.

2a for the TE polarization and in 2b for the TM polarization the torque on differently elongated particles as a function of the rotation angle θ is shown. The radius for the particles is $r_{Ref} = 0.01\lambda$. The torque shows a sinusoidal dependence on the angle between the optical axis and the major axis of the particle. The strength of the torque for the TE polarization is smaller by four orders of magnitude.
In contrast, the forces applied on the particles by the illuminating wave field are slightly higher for the TE- than for TM-polarized light[26]. By using rigorous diffraction theory or the dipole approximation, it can be shown that for TE polarization the force will not depend on the particle elongation or the particle orientation in the quasi-static approximation[26]. The polarizability of the particles is independent of the axis ratio. Consequently the torque becomes zero, because the particle behaves effectively like a circular cylinder, whose torque is always zero at the center of the waist. The remaining non-zero torque, even for very small particles, is the result of the rigorous solution of the problem, which takes higher multipoles and the influence of the magnetic field fully into account. The torque using the TE polarization is smaller by four orders of magnitude compared to the torque exerted on

geometrically identical particles with TM-polarized light. The torque can hence be regarded as effectively equal to zero. For a pure electric dipole, the polarization vector and the electric field vector will have the same direction, such that the torque, defined as $\tau = \mathbf{p} \times \mathbf{E}$ is zero.
The dependence on the rotation angle for both polarizations is nearly perfectly sinusoidal. The spatial distribution can be seen in Fig. 3a at $\theta = 0^o$

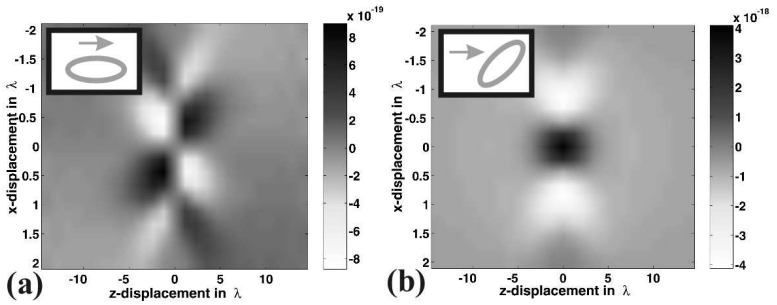

Figure 3: Spatial distribution of the torque for an elliptical cylinder much smaller than the wavelength ($r_1 = 0.01\lambda\sqrt{4}$) oriented at (a) $\theta = 0^o$ and (b) $\theta = 45^o$ for TE polarization.

and in 3b at $\theta = 45^o$ for TE polarization. The torque is shown as a function of the displacement of the particle from the waist of the laser beam. The illuminating beam propagates in the positive z-direction, meaning from the left to the right side of the figure. For the TE polarization, a significant non-zero torque is concentrated only around the region of the waist. If the orientation of the particle is with the major axis parallel to the optical axis ($\theta = 0^o$), a change of sign appears for positions of the particle behind the waist as well as for positions on the different sides of the optical axis. By rotating the particle, the force distributions before and after the waist adopt a similar form. At an orientation of 45^o, the distribution is nearly symmetric with respect to the waist of the laser.
In Fig. 4a at a particle orientation $\theta = 0^o$ and in 4b at $\theta = 45^o$, the same force distributions are shown assuming TM polarization. The basic behavior, like the change of sign in the torque along the different axes at $\theta = 0^o$, is the same as for the TE polarization, but the strength is much higher. The torque distribution for a particle rotation of 45^o is proportional to the square of the amplitude of the illuminating Gaussian beam.
The qualitative force distributions for the different elongated particles will not depend on the axis ratio, but the strength of the torque will scale with

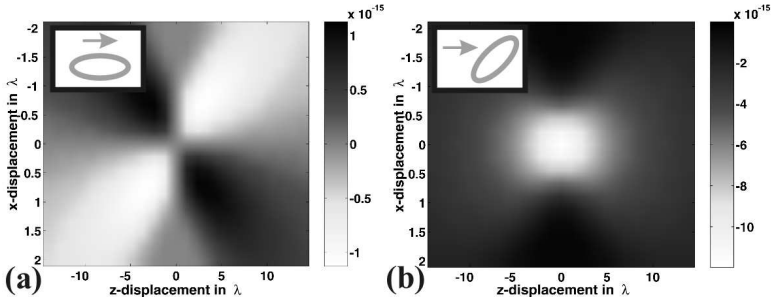

Figure 4: Spatial distribution of the torque for an elliptical cylinder much smaller than the wavelength ($r_1 = 0.01\lambda\sqrt{4}$) oriented at (a) $\theta = 0^o$ and (b) $\theta = 45^o$ for TM polarization.

the axis ratio of the particle. The strength and the axis ratio have the same ratio everywhere in space.
For an increase in the particle size, the sinusoidal dependence of the torque will be reduced and the distribution becomes slightly asymmetric. Figure 5a

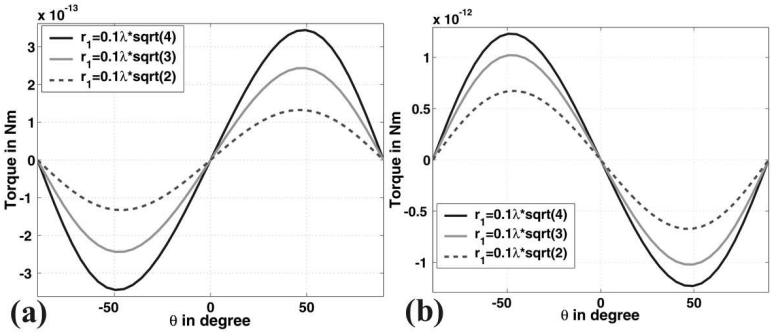

Figure 5: Torque on elliptical cylinders smaller than wavelength ($r_{Ref} = 0.1\lambda$) as a function of the orientation for (a) TE polarization and (b) TM polarization.

for TE polarization and 5b for TM polarization show the torque in the center of the waist for the three axis ratios as a function of the rotation angle. The radius of the particles is $r_{Ref} = 0.1\lambda$. The strength of the torque for TE-polarized light is still smaller but now only by a single order of magnitude. The sinusoid is somewhat stretched towards the larger rotation angle and the maximum of the torque is now at approximately $\pm 50^o$ for both polarizations. The difference in the sign of the torque still exists.

Overall the torque in this size domain shows a sinusoidal dependence on the angle between the particle and the optical axis. For smaller particles, which more closely satisfy the dipole approximation, the response is closer to a sinusoid. For a slightly increased size, the maximum of the torque is shifted to slightly larger angles and the response becomes asymmetric.

3.3 Particles with an intermediate size

With a further increase in the particle size the dipole approximation is no longer valid and effects can be observed which can only be explained by taking into account multiple reflections of the light inside the particles. The analysis of these intermediate-sized particles will be done in this section.
In this size domain the asymmetry of the torque on the orientation increases but the maximum of the torque tends to smaller rotation angles. This is

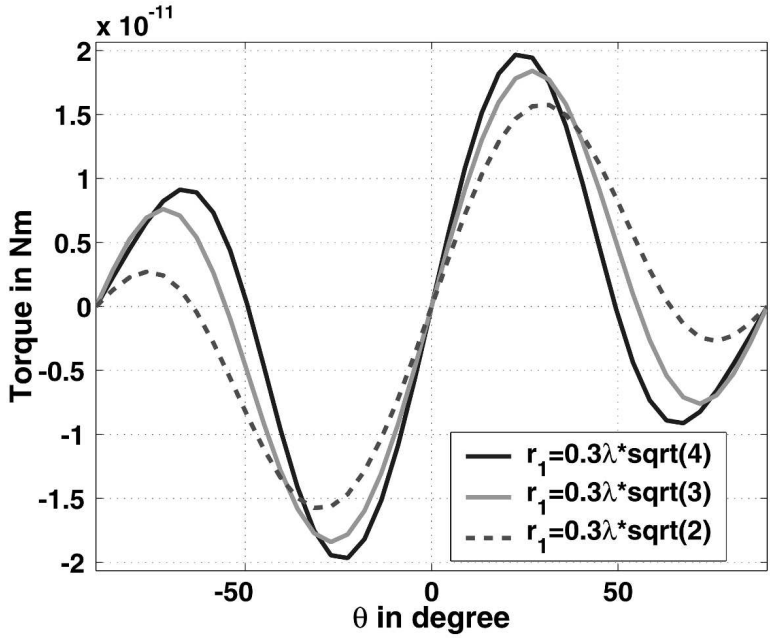

Figure 6: Torque on elliptical cylinders of an intermediate size ($r_{Ref} = 0.3\lambda$) as a function of the orientation for TE polarization.

shown in Fig. 6 for particles with a radius of $r_{Ref} = 0.3\lambda$ with TE polarization. The orientation for which the particle can be held at a stable rotational position now deviates from 90^o. In this case, the angles for which the particle

is held stable are between 50^o and 60^o. As the orientation of $\theta = 90^o$ indicates an alignment with the minor axis parallel to the propagation direction of the beam, the smaller angle corresponds to an orientation with a certain deviation from this cardinal direction. Additional points with a net torque of zero exist, but these points are unstable. This behavior can only be explained by the complicated diffraction process, in which multiple reflections inside the particle appear. As the radius of the particle is now approximately a quarter of the wavelength, the reflections will accumulate a phase delay close to π, such that constructive and destructive interference will play a dominant role. A similar behavior can be observed for TM polarization.

The size of the particle for which the sign of the torque inverts at rotation angle of 45^o is smaller for the TM than for the TE polarization. An additional difference is the orientation at which the particle can be held stable. For the TM polarization, the particle is stably trapped along the minor as well as the major axis of the elliptical particle. A third orientation between these two also has a net-torque equal to zero, but the point is unstable. For the TE polarization, it is the opposite: the particle is held stable at this intermediate position and the particle is unstable for the orientations along the two principal axes.

In addition, for the TM polarization despite the change of sign, the resulting torque as a function of the orientational angle for a slightly increased particle size will show a smooth and close to sinusoidal dependency. This can be seen in Fig.7. The particle has a radius of $r_{Ref} = 0.3\lambda$. Now there will be only a single orientation for which the particle is stable. This is with the minor axis parallel to the propagation direction of the illumination. The entire spatial torque distribution will suffer from this change in the sign. Figure 8a shows the torque as a function of the displacement of the particle at a rotation angle of 0^o and Fig. 8b shows the torque for a particle oriented at 45^o. In the distribution for the torque on the particle oriented at 0^o, the torque is maximum at positions somewhat after the waist. A significant asymmetry in the torque for the particle oriented at 45^o can be seen, which is due to the comparable size of the particle and the beam waist.

Summarizing the results of this section, we can state that for intermediate size particles, the angle-dependent torque becomes more asymmetric. In TM polarization the particles are stably trapped along the major axis as well as along the minor axis. A third point exists with a zero net-torque but the point is unstable. For TE polarization it is the opposite case, as the particle is stably trapped at this angle and unstable along the major and minor axis.

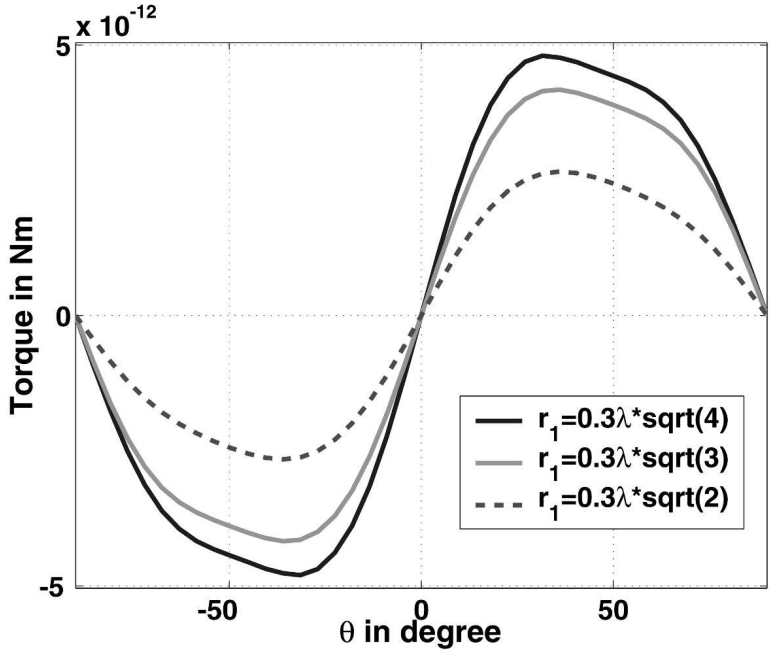

Figure 7: Torque on elliptical cylinders of an intermediate size ($r_{Ref} = 0.3\lambda$) as a function of the orientation for TM polarization.

3.4 Particles with a large size

For a further increase in the particle size with a radius significantly above a third of a wavelength, the response becomes more complex and different orientations exist for which the particles are rotationally stable.

For this size regime, a simple relation between the torque and the particle geometry is not possible. Figure 9a shows the torque at the center of the waist for particles with a radius of $r_{Ref} = 0.5\lambda$ for the TE polarization and Fig. 9b shows the torque for the TM polarization. It can be seen that for some of the particles, different orientations exist at which the particle is stable and the net torque is zero. For the TE polarization, the particle with a radius of $r_1 = 0.5\lambda\sqrt{3}$ can be held at an angle θ of $\pm 71^o$ and $\pm 28^o$. The strength of the torque for the two polarizations is comparable and is even slightly larger for TE-polarized light.

Nevertheless, the spatial distribution of the torque will show similarities for all the particles. The distributions for the two particles oriented at $\theta = 0^o$ and $\theta = 45^o$ are shown for TE polarization in Figs. 10a and 10b. The spatial

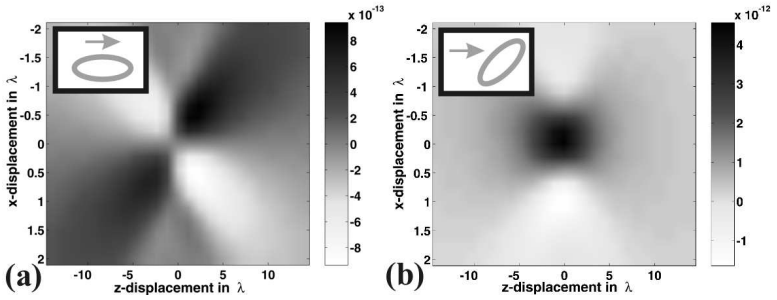

Figure 8: Spatial distribution of the torque for an elliptical cylinder of an intermediate size ($r_1 = 0.3\lambda\sqrt{4}$) oriented at (a) $\theta = 0^o$ and (b) $\theta = 45^o$ for TM polarization.

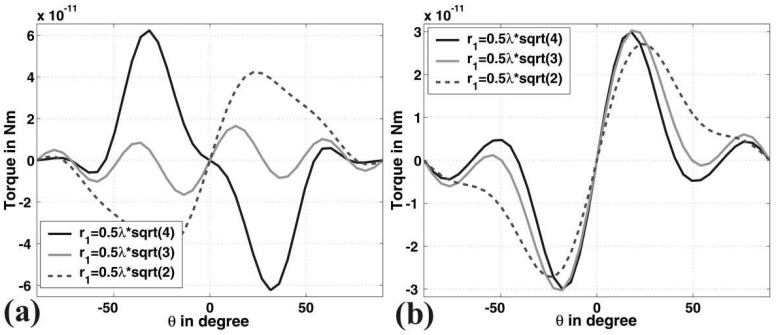

Figure 9: Torque on elliptical cylinders of a size comparable to the wavelength ($r_{Ref} = 0.5\lambda$) as a function of the orientation for (a) TE polarization and (b) TM polarization.

distribution for the same particle but illuminated with TM polarized light is qualitatively the same as for the TE polarization. They differ only slightly in strength. For the particle aligned with the major axis parallel to the optical axis, the torque above the optical axis ($x > 0$) is always negative and below the axis positive for the two polarizations. The particles oriented at 45^o will exhibit a maximum torque for a position above the optical axis. The torque is nearly zero at positions below the optical axis.

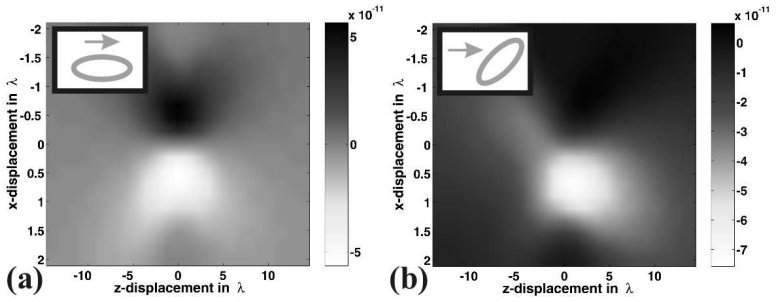

Figure 10: Spatial distribution of the torque for an elliptical cylinder of a size comparable to the wavelength ($r_1 = 0.5\lambda\sqrt{4}$) oriented at (a) $\theta = 0^o$ and (b) $\theta = 45^o$ for TE polarization.

4 Conclusion

In this article we have analyzed the torque exerted on dielectric elliptical cylinders by a highly focused Gaussian beam. Basically three different size domains have been identified, which show various characteristics in their torque response as a function of the orientation of the particle with respect to the illuminating beam as well as in their spatial behavior with respect to position within the wave field.

It was found that for particles much smaller than the wavelength, the torque depends perfectly sinusoidally on the angle between the particle orientation and the illumination direction of the laser beam. The torque will cause an orientation for the TM polarization of the major axis parallel to the optical axis and for the TE polarization with the minor axis parallel to the optical axis. Increasing the size causes deviations of the angle-dependent torque from the sinusoidal angle-dependency and an additional orientation exists at which the torque is zero. For the TM polarization this is an unstable orientation. In the TE polarization this orientation is the only stable and for an orientation along the minor axis or the major axis the torque is zero but the orientations are unstable. For a further increase of the size various orientation exists for which the particle is rotational stable. The overall orientational dependence of the torque shows a complex pattern. Such a behavior can only be analyzed by using rigorous diffraction theory.

The strength of the torque for particles much smaller than the wavelength is significant smaller for the TE than for the TM polarization. We have attributed this significant difference to the dominant influence of the electric

field component, which oscillates for TE polarization parallel to the infinite cylinder axis. In TM polarization the electric field oscillate perpendicular to the cylindrical axis and will cause a strong rotational acceleration of the particle. For particles with a size comparable to the wavelength the strength of the torque is comparable for the two polarizations.

The possibility of self alignment of particles upon illumination offers an interesting application for the precise writing of nano-optical devices that make use of elliptical particles. One example could be a plasmonic waveguide made of metallic nano-particles. As the wavelength for which a surface plasmon is excited in the particle depends strongly on the geometry, wave guides with different operating wavelengths could be fabricated by using particles with the appropriate shape. To create the waveguide, that is a chain of particles, optical tweezers could be used. The particles are aligned by choosing the proper illumination parameters. By using a parallelized optical tweezer generated e.g. by a diffractive fan-out element or just by a standing pattern of plane waves propagating in different directions, it would be possible to write photonic crystals based on elliptical particles with a high precision as the particles trapped at the appropriate periodic points will be aligned to form a perfect symmetric pattern in all directions.

Another field of research that has promising applications and is currently under investigation, is the self-alignment of particles by interaction with neighboring objects. In a system e.g. proposed by Stockman et al., a chain of metallic particles with descending size is used as a novel type of plasmonic lens that concentrates a huge amount of energy into a small spatial region to yield a highly confined light source[27]. By choosing an appropriate illuminating field, the particles could attract as well as orient each other in such a way that the efficiency of the proposed nano-lens is maximized.

This research was supported by the European Union within the framework of the Future and Emerging Technologies program “Super Laser Array Memory” under grant No. IST-2000-26479.

References

[1] A. Ashkin, "Acceleration and trapping of particles by radiation pressure.", Phys. Rev. Lett. **24**, 156–159 (1970).

[2] A. Ashkin and J. M. Dziedzic, "Optical levitation by radiation pressure.", Appl. Phys. Lett. **19**, 283–285 (1971).

[3] D. G. Grier, "A revolution in optical manipulation.", Nature **424**, 810–816 (2003).

[4] A. Ashkin, "Optical trapping and manipulation of neutral particles using lasers.", Proc. Natl. Acad. Sci. USA **94**, 4853–4860 (1997).

[5] R. C. Gauthier and A. Frangioudakis, "Theoretical investigation of the optical trapping properties of a micro-cubic glass structure.", Appl. Opt. **39**, 3060–3070 (2000).

[6] Y. Harada and T. Asakura, "Radiation forces on a dielectric particle in the Rayleigh scattering regime.", Opt. Commun. **124**, 529–541 (1996).

[7] S. Kawata, Y. Inouye and T. Sugiura, "Near-field Scanning Optical Microscope with a Laser Trapped Particle.", Jpn. J. Appl. Phys., **33**, L 1725–L 1727 (1994).

[8] A. Rohrbach, E. L. Florin, E. H. K. Stelzer, "Photonic Force Microscopy: simulation of principles and applications.", Proc. SPIE **4431**, 75–86 (2001).

[9] P. L. Marston and J. H. Crichton, "Radiation torque on a sphere caused by a circularly-polarized electromagnetic wave.", Phys. Rev. A **30**, 2508–2516 (1984).

[10] A. T. O'Neil and M. J. Padgett, "Three-dimensional optical confinement of micron-sized metal particles and the decoupling of the spin and orbital angular momentum with an optical spanner.", Opt. Commun. **185**, 139–143 (2000).

[11] M. E. J. Friese, T. A. Nieminen, N. R. Heckenberg and H. Rubinsztein-Dunlop, "Optical torque controlled by elliptical polarization.", Opt. Lett. **23**, 1–3 (1998).

[12] S.Bayoudh, T. A. Nieminen, N. R. Heckenberg and H. Rubinsztein-Dunlop, "Orientation of biological cells using plane-polarized Gaussian beam optical tweezers.", J. Mod. Opt. **50**, 1581–1590 (2003).

[13] A. I. Bishop, T. A. Nieminen, N. R. Heckenberg and H. Rubinsztein-Dunlop, "Optical application and measurement of torque on microparticles of isotropic nonabsorbing material.", Phys. Rev. A **68**, 033802 (2003).

[14] P. Galadja and P. Ormos, "Orientation of flat particles in optical tweezers by linearly polarized light.", Opt. Express **11**, 446–451 (2003).

[15] P. Galajda and P. Ormos, "Complex micromachines produced and driven by light.", Appl. Phys. Lett. **78**, 249–251 (2001).

[16] M. E. J. Friese, H. Rubinsztein-Dunlop, J. Gold, P. Hagberg and D. Hanstorp, "Optically driven micromachine elements.", Appl. Phys. Lett. **78**, 547–549 (2001).

[17] T. A. Nieminen, N. R. Heckenberg and H. Rubinsztein-Dunlop, "Optical measurement of microscopic torques.", J. Mod. Opt. **48**, 405–413 (2001).

[18] H. Polaert, G. Gréhan and G. Gousbet, "Forces and torques exerted on a multilayered spherical particle by a focused Gaussian beam.", Opt. Comm. **155**, 169–179 (1998).

[19] J. P. Barton, D. R. Alexander and S. A. Schaub, "Theoretical determination of net radiation force and torque for a spherical particle illuminated by a focused laser beam.", J. Appl. Phys. **66**, 4594–4602 (1989).

[20] T. A. Nieminen, H. Rubinsztein-Dunlop, N. R. Heckenberg and A. I. Bishop, "Numerical Modelling of Optical Trapping.", Computer Physics Communications **142**, 468–471 (2001).

[21] C. Hafner, "Post-Modern Electromagnetics.", John Wiley & Sons (1999).

[22] L. Novotny, R.X. Bian and X.S. Xie, "Theory of nanometric optical tweezers.", Phys. Rev. Lett. **79,** 645–648 (1997).

[23] C. Hafner, "The Generalized Multipole Technique for Computational Electromagnetics.", Artech House Books, (1990).

[24] X. Wang, X.-B. Wang and P.R.C. Cascoyne, "General expressions for dielectrophoretic force and electrostational torque derived using the Maxwell stress tensor.", Journal of Electrostatics **39**, 277–295 (1997).

[25] M. Lester and M. Nieto-Vesperinas, "Optical forces on microparticles in an evanescent laser field.", Opt. Lett. **24**, 936–938 (1999).

[26] C. Rockstuhl and H. P. Herzig, "Rigorous diffraction theory applied to the analysis of the optical force on elliptical nano- and micro-cylinders.", submitted to J. Opt. A: Pure Appl. Opt.

[27] K. Li, M. I. Stockman and D. J. Bergman, "Self-Similar Chain of Metal Nanospheres as an Efficient Nanolens.", Phys. Rev. Lett. **91,** 227402 (2003).

Theoretical and experimental investigation of phase singularities generated by optical micro- and nano-structures

Carsten Rockstuhl, Martin Guy Salt, Hans Peter Herzig

University of Neuchâtel, Institute of Microtechnology,
Rue A.-L. Breguet 2, CH-2000 Neuchâtel, Switzerland

July 16, 2004

Abstract

Phase singularities appear in the diffracted far-field of an optical micro-structure if the object is of a sufficient lateral size to induce an appropriate phase delay. We present results that determine the critical dimension of a single phase bar for the generation of dislocations in the far-field. Using scalar theory, an analytical equality is derived that must be met by the structure. Because the size of the object is comparable to the wavelength, rigorous diffraction theory is used to find this feature size for a true object. Once the dislocations appear, their position is related strongly to the geometry of the object. We show theoretically and experimentally by using an interference microscope, that for a single phase bar the distance between pairwise generated dislocations depends to a good approximation linearly on the width of the structure.

Keywords: phase singularities, high-resolution microscopy, diffraction

1 Introduction

Phase singularities are points in space where the real as well as the imaginary part of an electromagnetic field becomes zero and consequently the phase cannot be determined [1]. The phase jumps always by π while scanning through a dislocation, independent of the scan direction. The gradient of the phase becomes infinite at this position and the phase variation along a closed loop around such a point is always an integer multiple of 2π, the topological charge of the vortex [2]. Illuminating optical micro- and nanostructures with an arbitrary wave-field might induce a scattered field that interferes entirely destructively with the illuminating wave-field, thus creating a phase singularity at this point[3, 4, 5]. The position and consequently the relative distance between these pairwise generated dislocations can be linked to the geometry of the structure[6]. Because the accuracy of the determination of the position for dislocations is not restricted by the classical diffraction limit, the geometry of the object can be determined with a high accuracy by using a priori information about the object, which offers a valuable tool for metrological applications[7, 8]. As an example of this is the semiconductor industry, where it is necessary to measure the lateral dimensions of structures using non-destructive techniques, the distances between phase singularities providing a high precision quality factor for the fabricated objects. A more general application is the calibration of length standards on a sub-micron length scale.
The instrument we are using for the interferometric measurements functions in transmission, hence we will restrict our investigations to the case where the object that generates the scattered field works likewise in transmission and has a refractive index that is comparable to most glasses and polymers. Additionally, the instrument is in principle a classical microscope and has no access to the evanescent part of the angular spectrum of the transmitted wave field, due to the numerical aperture being equal to or smaller than one. This low-pass filtering property will be taken into account for all the calculations to compare theory with measurement. The field that is measurable in the High Resolution Interference Microscope (HRIM) is essentially a paraxial field that has no longitudinal component. We will discriminate in this two-dimensional problem the two cases where the field is TE-polarized (the vector of the electric field oscillates parallel to the space-invariant direction of the structure) and TM-polarized (the vector of the magnetic field oscillates parallel to the space-invariant direction of the structure) and analyze the po-

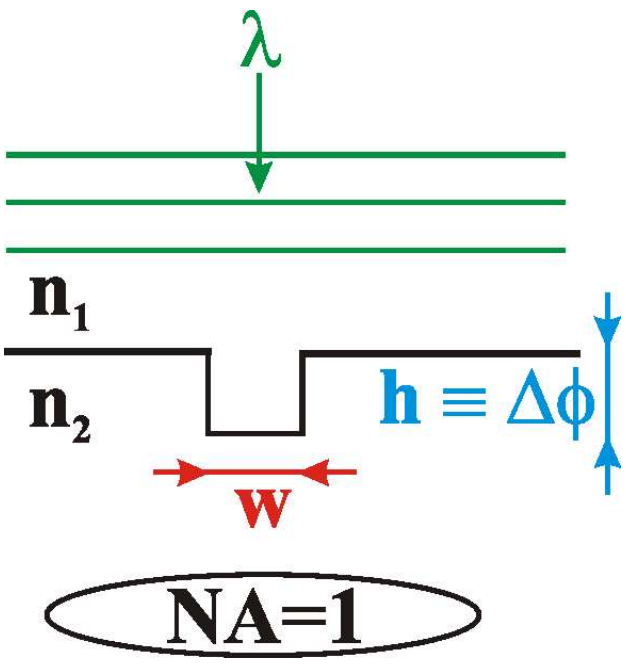

Figure 1: Basic setup of the problem under investigation.

sition of the phase singularity in the electric field for TE polarization and the position of the phase singularity in the magnetic field for TM polarization. Nevertheless, both coincide in the paraxial approximation that holds for the measurements.

Figure 1 shows the basic geometry of the problem considered in this paper. Two half-spaces with different refractive indices n_1 and n_2 are separated by a planar surface. The illuminating wave field with wavelength λ is a planar wave. The half-spaces are perturbed by a phase bar that is a trench within the plane surface. The parameters of the trench are its width w and its geometrical height h. The optical height is given by $\Delta\phi = k(n_2 - n_1)h$ with k being the wavenumber. If the phase bar is much smaller than the wavelength, it will not interact with the incoming wave front efficiently and in consequence the transmitted field is comparable to a plane wave. Increasing the dimension of the object will lead to a more pronounced scattered field and from a certain dimension on the scattered field will interfere with the incident wave field such that complete destructive interference gives a point in the second half-space where a phase dislocation appears.

In this paper we will investigate the object conditions necessary for the gen-

eration of phase singularities in the far-field and the subsequent spatial dependence as a function of the geometry of the object.
In the second section we will determine the smallest size of an object that can generate a phase singularity in the far-field. This will be done using scalar theory as well as by using an exact rigorous diffraction theory. The choice of a proper polarization for the illuminating wave-field as well as the variation of the distance between singularities by changing the object width is discussed. In the third section we analyze experimentally the variation of this distance as a function of the width of the object. For this purpose we present the experimental set-up of the HRIM and analyze its accuracy for the measurement of the distance between phase singularities.

2 Conditions for the generation of singularities

2.1 Scalar approximation

For the derivation of the condition for the appearance of a phase singularity in the diffracted far-field of an optical microstructure, we will start for simplicity at the condition for a grating. The far-field of such an object is written as a superposition of a discrete number of plane waves, which have an amplitude a_m. A phase singularity appears only if the sum over all propagating amplitudes except the highest amplitude is equal to the highest amplitude. Otherwise a complete destructive interference is not possible. This condition reads as [9]

$$\sum_{m \neq n} \mid a_m \mid \geq \mid a_n \mid \qquad \forall n, \tag{1}$$

where the sum is taken over all the amplitudes that propagate. The proof of equation 1 is given in appendix A. For the problem of finding the dimensions of a perturbation such that a phase singularity is generated, we assume that the highest amplitude is always the amplitude of the zero-order because in the unperturbed case this is the only order that has a value which differs from zero. Introducing a perturbation will couple light into other orders but the order with the highest amplitude will be always the zero order before a phase singularity is generated, hence $a_n = a_0$. In the paraxial approximation the strength of the diffracting amplitudes is calculated by doing a Fourier

Transformation of the transmission function $T(x)$ of the object [10] that relates the field behind the structure $U_{Trans}(x)$ to the illuminating field $U_{Inc}(x)$ by a simple multiplication $U_{Trans}(x) = T(x)U_{Inc}(x)$. For the treatment of single objects we calculate the amplitude for the limit of an infinite period. The summation over the discrete spectrum of plane waves in Eq. (1) will become an integration over a continuous spectrum of the propagating part of the spectrum. This reads as

$$\int_{\nu} \mid a(\nu) \mid (1 - \delta(\nu - \nu_0))d\nu \geq \int_{\nu} \mid a(\nu) \mid \delta(\nu - \nu_0)d\nu \quad \Lambda \rightarrow \infty. \tag{2}$$

Using the transmission function of a single phase bar

$$T(x) = \begin{cases} e^{i\frac{2\pi h}{\lambda}(n-1)} & \mid x \mid \leq \frac{w}{2} \\ 1 & \mid x \mid > \frac{w}{2} \end{cases} \tag{3}$$

and calculating the Fourier transformation we derive the equality

$$0 = 1 - \frac{4}{\pi}\sin(\frac{\Delta\phi}{2}) \int_0^{\pi w} \frac{\left|sin\left(\frac{t}{\lambda}\right)\right|}{t} dt \tag{4}$$

that must be fulfilled by the structure in order to generate a phase singularity in the far-field. The equation is derived in appendix A. The integral cannot be solved analytically and further simplification is not possible. Figure 2 shows the numerically evaluated difference between the right and left hand side of Eq. (4) as a function of the width of the phase bar in units of the wavelength for three different induced phase delays. For a cooperative scatterer, that is an object which induces the maximum possible phase delay of π, the smallest width of a phase bar that generates a phase singularity in the far-field is $\lambda/4$. Smaller structures will not induce a sufficiently strong scattered field. If the induced phase delay is smaller than π, the width of the structure has to be consequently larger for the generation of a phase singularity. If the phase delay is e.g. $\frac{2}{3}\ \pi$, the width must be approximately 0.3 λ, and in the case of an induced phase delay of $\frac{1}{3}\ \pi$ the width must be 0.6 λ. The condition for the appearance of dislocations generated by arbitrary objects can be found using Eq. 2 and applying the same procedure as described in Appendix A for the phase bar. In cases where the transmission spectrum cannot be found analytically, simple numerical routines can be used to evaluate the integrals. As a second example for the application of the proposed criteria in equation 2, we show in Fig. 3 the smallest width of two phase bars as a function of

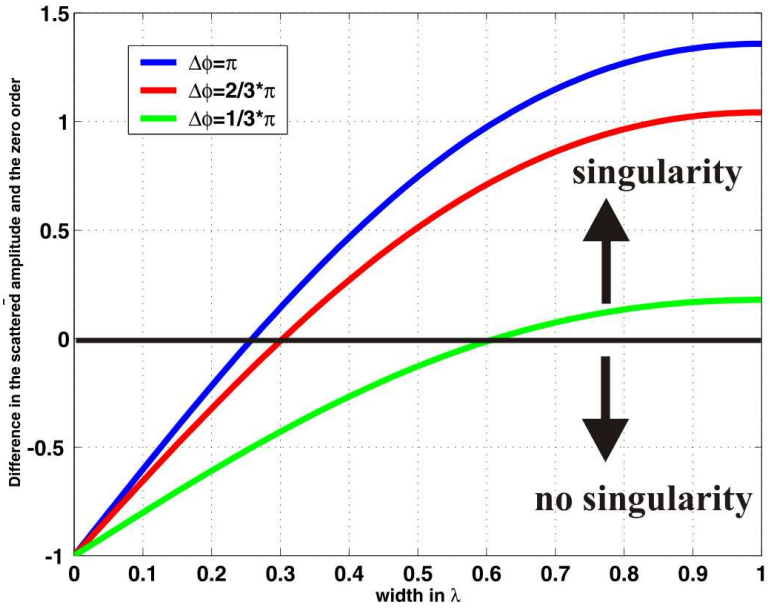

Figure 2: Evaluation of Eq. (4) for three different phase values.

the separation such that they generate a dislocation in the far-field. The induced phase delay of both bars is π. If they are not separated, the width corresponds to half of the width of the single bar that generates a dislocation. Increasing the distance will decouple them. For separation distances larger than the wavelength, the bars behave like a Fabry-Perot resonator and an oscillating behavior can be seen, which is attributed to scattered field that suffers from back and forth reflections between the structures.

All the feature sizes for the objects which can generate a phase singularity in the far-field are comparable to the wavelength. In this region, the scalar and paraxial approximation no longer holds and one has to use a rigorous diffraction theory to describe properly the interaction of a light wave with such a structure. Consequently we will use a grating theory[11] to predict the smallest size of a real object that can generate a phase singularity in the far-field without any approximation. Such a grating theory can be used for the modelling of single objects by choosing a sufficiently large period in the calculation, which is additionally not an integer multiple of the period.

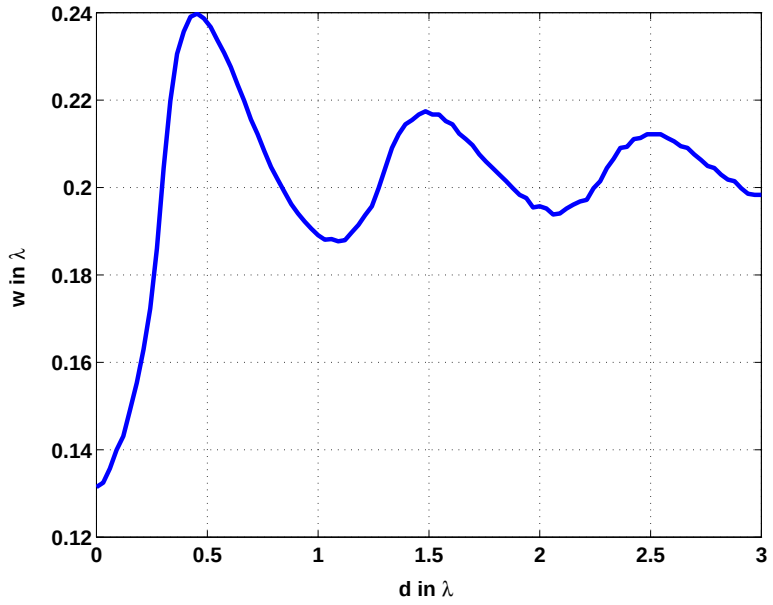

Figure 3: Width of two π-phase bars for which a dislocation appears as a function of the distance between the two bars.

2.2 Rigorous treatment

By using rigorous diffraction theory, we have to choose the polarization of the illuminating wave-field. We will use a TM-polarized wave because it is known that for the current structure a phase singularity appears at smaller feature sizes for this polarization. The trench can be regarded as a waveguide. If the material would be a perfect conductor, a cut off width would exist for TE polarization. For structures smaller than this width no mode is excited and the field cannot penetrate the structure. On the other hand, for TM polarization a mode can always be excited. For the present geometry the same arguments can be applied. For TE polarization no mode is efficiently excited and hence the field scattered by the defect will not be strong enough to perturb the transmitted plane wave sufficiently. For TM polarization such a mode is excited and will generate a sufficiently strong scattered field, which can interfere completely destructively with the transmitted plane wave to create a phase singularity. Hence we use a TM-polarized plane wave to generate a phase singularity at a feature size that is as small as possible[12].

Figure 4 shows the distance between a pair of generated singularities di-

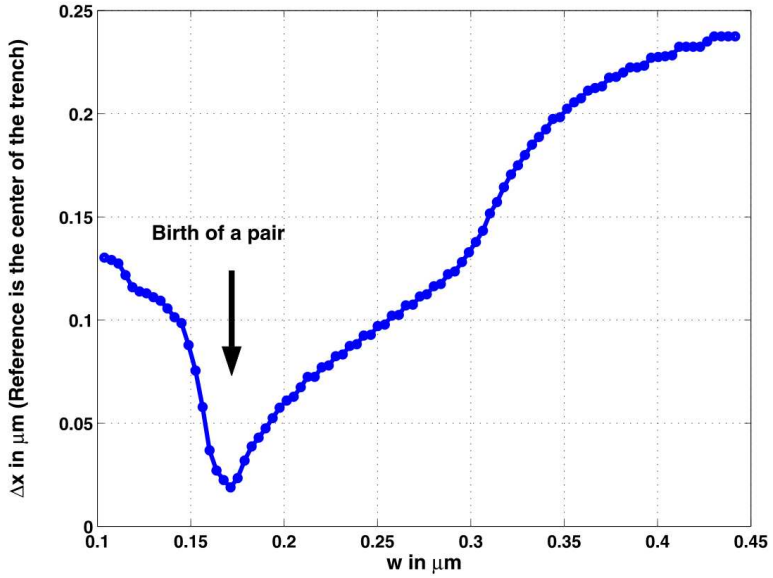

Figure 4: Distance between singularities generated behind a trench as a function of its width.

rectly behind the structure as a function of the width of the object if the induced geometrical phase delay is π. As illuminating wavelength we have used 488 nm, the refractive index of the medium in the first half space was 1, the refractive index of the medium in the second half space was 1.5 and the geometrical height was chosen consequently equal to the wavelength.
For the determination of the distance between the phase singularities, we have calculated first the complex field distribution directly behind the trench for each width using the Rigorous Coupled Wave Analysis (RCWA) [11]. RCWA is a grating theory that can be applied to the description of single objects by choosing a period much larger than the wavelength and not an integer multiple of the wavelength. We have used a period of $20.2\mu m$ in the calculation and the number of diffraction orders that were retained in the plane wave expansion was sufficiently large such that the position of the singularities converges to a fixed value.
Before determining the position of the phase singularity we have low-pass filtered the field distributions assuming a numerical aperture equal to unity. For the determination of the position of the dislocations we have calculated the gradient of the locally unwrapped phase distribution. The gradient of the phase in a phase singularity is infinity. Describing the fields numerically

will not give infinite values for the gradient, but finding the maximum of the gradient and applying a simple threshold criteria, determines the position of the dislocations automatically without ambiguity and with a sufficiently high precision. To find out whether the point in the field with the highest phase gradient corresponds to a phase singularity or not, we have used an algorithm for the detection of a phase singularity described in the literature [13].

From Fig. 4 and from the corresponding field distributions that were calculated, we deduce a phase bar with a width of 180 nm as the smallest width of an object that generates a phase singularity in the far-field. The points in Fig. 4 for phase bars with a smaller width are not the distance between the singularities but rather the distance between the points with the highest phase gradient. The width of 180 nm is higher than the predicted scalar value of 122 nm. This is not a surprise because by treating the problem rigorously we see that light is already diffracted inside the structure, which will lead to transport of energy away from the trench while passing through the structure. The field is somewhat smeared out and the sharp character of the field distribution assumed in the thin element approach is lost. Additionally, the phase delay induced by such a structure is for the same reason always weaker and hence smaller than π[14]. Consequently the phase singularity for real objects will appear at feature sizes bigger than the predicted scalar value. Nevertheless, increasing the contrast in the refractive index between the first and the second half space allows the appearance of phase singularities for smaller objects.

Additionally, it can be see from Fig. 4 that the distance between the singularities scales, to a good approximation, linearly with the width of the trench. Because the phase singularities can be measured with a very high precision, topological features of the structure can be similarly determined with a high resolution, assuming that a priori knowledge about the object is available. In the next section we will show experimental results on the behavior of phase singularities generated by a trench written in photoresist using an electron beam.

3 Measurements with the HRIM

Figure 5 shows the experimental set-up of the HRIM. An Argon laser ($\lambda = 488nm$) is used as a light source and the interference microscope consists of

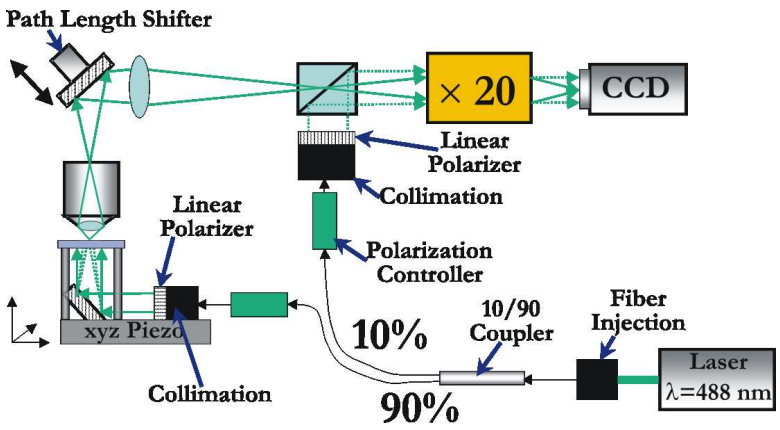

Figure 5: Geometrical setup of the High Resolution Interference Microscope.

a reference arm and an signal arm. Two essentially telescopic magnification stages lead to a magnification of approximately 1000 that gives access to the relevant nanometrique lateral scale. A pixel of the CCD camera corresponds, after calibration with a grating, to $20nm$ in the object plane. The object is located on a x-y-z piezo stage. The z-axis allows a successive movement in the third dimension that makes it possible to measure the field along the propagation direction. The phase distribution is determined by a classical 5-frame interference algorithm in each z-plane and a subsequent phase reconstruction algorithm that assumes a plane wave distribution far away from the scatterer gives the relative phase along the z-direction. Because the trenches are grooves running in the y-direction, the field is invariant along this direction too. For a reduction of the noise the measured fields are averaged in the y-direction. The numerical aperture of the system is 0.85. Figure 6 shows the measured intensity and phase (isophases) distribution behind a trench and in Fig. 7 the rigorously simulated intensity and phase distribution is shown.

Please note that the transition goes from photoresist (top) to air (bottom) and in the figure the illumination direction is along the z-direction from the top. As the refractive index we have assumed 1.5, the width was 450 nm and the height was 450 nm. As the illumination wave field was TM-polarized. An overall excellent agreement between calculation and measurement can be seen. The two characteristic singularities appear directly behind the structure and are indicated by circles. These are the singularities that can be related to the width of the object. Four additional singularities appear in the measured as well as in the simulated virtual field in front of the structure.

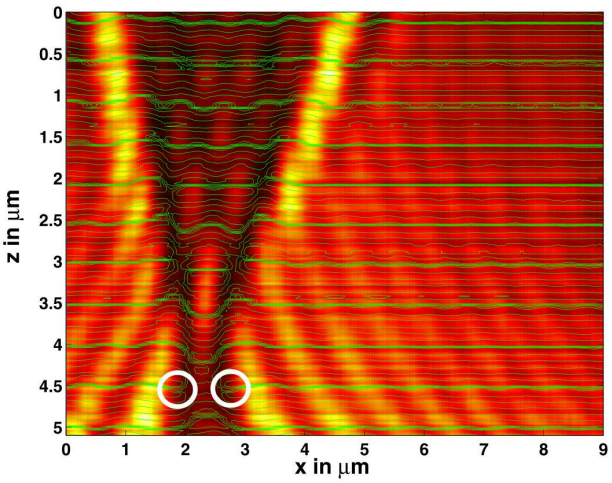

Figure 6: Measured intensity and phase distribution in the far-field of a single trench in photoresist ($w \approx 0.5\mu m$).

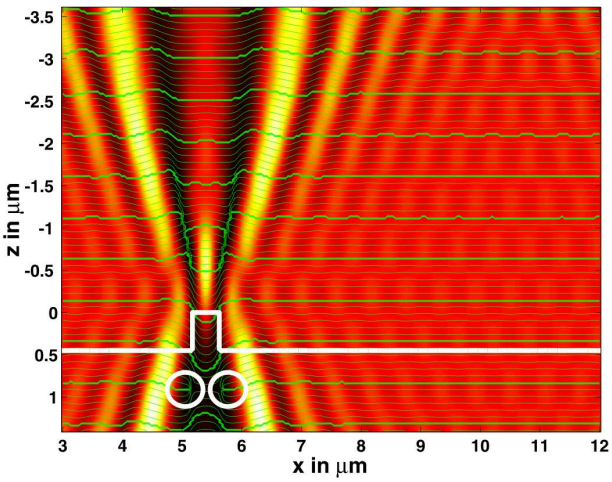

Figure 7: Calculated intensity and phase distribution in the far-field of a single trench in photoresist ($w = 0.45\mu m, h = 0.45\mu m$).

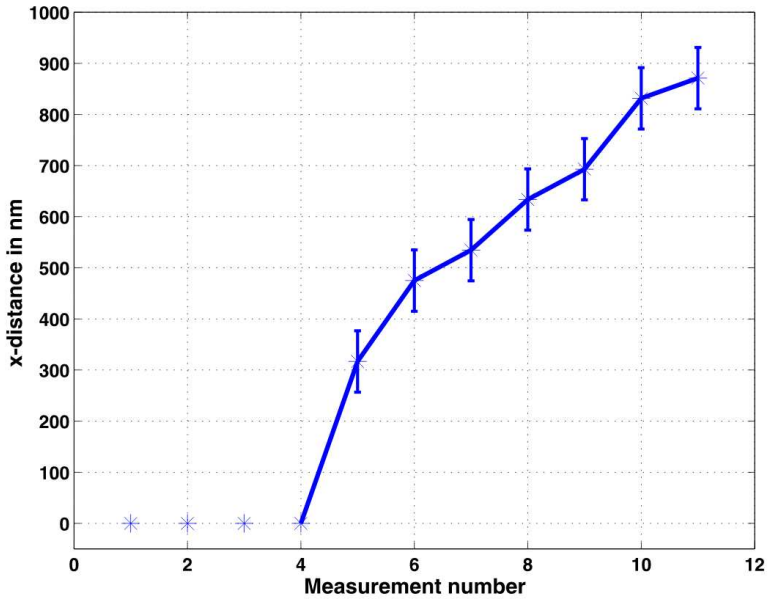

Figure 8: Measured x-distances between dislocations generated by a trench with increasing width.

This is a virtual field because it results actually from the back propagated transmitted field distribution in the first half space. To determine the reproducibility of our instrument we determined the distance between dislocations of the same structure several times. We found an accuracy of 3 pixels for the CCD camera that corresponds to a resolution of 60 nm.
To verify experimentally the linear behavior of the distance between singularities and the width of the phase bar, we fabricated a series of trenches with an increasing line width. Figure 8 shows the results. The trench width difference between 2 measurements alternates between 20 nm and 30 nm and the largest trench was 500 nm. The theoretically predicted linear behavior can be seen. In our measurements the smallest structure that can generate a phase singularity in the far-field is a trench width of 360 nm. The field distribution of smaller trenches were measured but no phase singularity appears in the diffracted far-field. This width is higher than the predicted value in section two due to the smaller numerical aperture. An additional source for the deviation from the optimum value is the non-optimal height which cannot be controlled with the desired precision. Additionally, the refractive index of the photoresist is subject to ambiguities. Nonetheless, the principal

behavior is comparable to the theoretically predicted one.

4 Conclusions

We have shown theoretically and experimentally that there is a minimum lateral feature size for an object for the generation of a phase singularity in the far-field of the structure. In the scalar approximation this smallest feature size is $\lambda/4$ and thus comparable to the diffraction limit. For the class of objects in the present investigation the real size for the object using a rigorous calculation is somewhat higher. Once the phase singularity pairs appear, their separation is to a good approximation linear with the width of the object. The linear dependence has been proved experimentally using a HRIM, with a spatial resolution for the distance determination of approximately $60nm$.

Acknowledgements

The authors would like to thank Arthur van de Nes from the TU Delft for providing us with the sample.
The research was supported by the European Union within the framework of the Future and Emerging Technologies-SLAM program.

Appendix A

The field behind a grating, written as a superposition of plane waves is given by

$$U(\mathbf{r}) = \sum_m a_m e^{i\mathbf{k}_m\mathbf{r}}. \tag{5}$$

A phase singularity appears if the field is zero, hence

$$\sum_m a_m e^{i\mathbf{k}_m\mathbf{r}} = 0. \tag{6}$$

Subtracting an arbitrary order a_n from both sides of equation 5 gives [9]

$$\sum_{m\neq n} a_m e^{i\mathbf{k}_m\mathbf{r}} = -a_n e^{i\mathbf{k}_n\mathbf{r}}. \tag{7}$$

Taking the absolute value

$$|\sum_{m\neq n} a_m e^{i\mathbf{k}_m\mathbf{r}}| = |-a_n e^{i\mathbf{k}_n\mathbf{r}}| = \mid a_n \mid \tag{8}$$

and applying the triangular inequality finally leads to

$$\sum_{m\neq n} \mid a_m \mid \geq \mid a_n \mid , \tag{9}$$

which is equation 1[9].
For the binary phase grating whose transmission function is given by

$$T(x) = \begin{cases} e^{i\frac{2\pi h}{\lambda}(n_1-n_2)} & 0 \leq x < w \\ 1 & w \leq x < \Lambda \end{cases} \tag{10}$$

the amplitude of the m'th order upon plane wave illumination is given by [10]

$$a_m = \frac{1}{\Lambda}\left[\int_0^w e^{i\Delta\phi} e^{-im\frac{2\pi}{\Lambda}x} dx + \int_w^\Lambda e^{-im\frac{2\pi}{\Lambda}x} dx\right] \tag{11}$$

with $\Delta\phi = \frac{2\pi}{\lambda}(n_2 - n_1)h$. By solving the integral we find the absolute value of the m'th amplitude as

$$|a_m| = \frac{2}{\pi}\sin\left(\frac{\Delta\phi}{2}\right)\frac{\left|sin\left(\frac{m\pi w}{\Lambda}\right)\right|}{|m|} \tag{12}$$

To sum of all propagating orders is

$$\sum_m |a_m| = \frac{4}{\pi} sin\left(\frac{\Delta\phi}{2}\right)\sum_{m=1}^{\frac{\Lambda}{\lambda}} \frac{|\sin\left(m\frac{\pi}{\Lambda}w\right)|}{m} \tag{13}$$

In the limit of an infinite period the amplitude of the zero order is unity and the scattered field equals

$$\int_\nu \mid a(\nu) \mid (1-\delta(\nu-\nu_0))d\nu = \frac{4}{\pi}\sin\left(\frac{\Delta\phi}{2}\right)\int_0^{\pi w} \frac{\left|sin\left(\frac{t}{\lambda}\right)\right|}{t} dt \tag{14}$$

A phase singularity appears if the integral over the scattered amplitudes equals the zero amplitude which is equation 4.

References

[1] Nye J F and Berry M V 1979 *Proc. R. Soc. London A*, **336** 165

[2] Basistiy I V, Soskin M S and Vasnetsov M V 1994 *Opt. Commun.*, **119** 604

[3] Totzeck M and Tiziani H J 1997 *Opt. Commun.* **136** 61

[4] Krumbügel M A and Totzeck M 1993 *Opt. Commun.* **98** 47

[5] Drauschke A 2001 *J. Opt. A: Pure Appl. Opt.* **3** 500

[6] Eberler M, Dorn R, Münzer B, Quabis S and Leuchs G 2001 *Proceedings of the World Conference on Systematics, Cybernetics and Informatics, Orlando*

[7] Tychinsky V P 1989 *Opt. Commun.* **74** 41

[8] Tychinsky V P and Velzel C H F 1994 *Current Trends in Optics* (Academic Press London) p 255

[9] Blattner P 1999 *Light fields emerging from periodic optical microstructures* (PhD Thesis University of Neuchâtel, Switzerland) p 61

[10] Born M and Wolf E 1999 *Principles of Optics*, (Cambridge University Press) p 401

[11] Moharam M G and Gaylord T K 1981 *J. Opt. Soc. Am.* **71** 811

[12] Totzeck M, Jacobsen H and Tiziani H J 1999 *Advanced Photonic Sensors and Applications* (SPIE Proc) **3897** p 424

[13] Totzeck M and Tiziani H J 1997 *Opt. Commun.* **138** 365

[14] Mecca C M J, Li Y and Wolf E 2000 *Opt. Commun.* **182** 265

Investigation of the basic properties of phase singularities generated by a phase bar or trench

Carsten Rockstuhl, Martin Guy Salt, Hans Peter Herzig

University of Neuchâtel, Institute of Microtechnology,
Rue A.-L. Breguet 2, CH-2000 Neuchâtel, Switzerland

July 16, 2004

Abstract

In the present paper we determine the conditions necessary for the generation of phase singularities in the far-field by a phase bar or a trench. The ultimate goal of our work is to link object parameters to a topological distribution of pairs of singularities. We apply scalar theory and show that objects smaller than the diffraction limit are not capable of generating singularities. Supplementary rigorous electromagnetic theory is applied to determine this feature size for a real structure. Topological behavior by changing a typical object parameter and stability of the position of phase singularities in the presence of neighbouring scatterers are analyzed.

PACS: 61.46; 68.10

Keywords: Phase singularities, High-Resolution Microscopy, Diffraction

1 Introduction

Phase singularities are points in space where the real and imaginary parts of an electromagnetic field are equal to zero, meaning the intensity is always zero and consequently the phase becomes undetermined. A description of their basic properties and a resulting classification were given by Nye and Berry in the mid seventies[1]. Basically, one distinguishes between edge, screw and mixed dislocations. They appear in various optical schemes. A perspicuous example for an edge dislocation, a line along which a phase jump of π occurs is e.g. a simple Gauss-Hermite laser mode with the mode parameter 01. That laser mode has an intensity equal to zero along a certain axis (e.g. y-axis) and the phase difference in the waist between the field in space with $y > 0$ and in $y < 0$ is equal to π. The phase at $y = 0$ cannot be defined. Screw dislocations are a common feature in wave fields that contain speckles. Their randomly distributed points with zero intensity are intimately related to screw dislocations[2]. Phase variation on a closed circle around a screw dislocation is always an integer multiple n_i of 2π, which offers the possibility of measuring the location of the phase dislocation quite precisely by means of interferometric techniques. Tychinsky and co-workers proposed in a pioneering work at the end of the eighties[3, 4] the use of structural features within a phase-field to reconstruct unknown object properties with the ultimate target of overcoming the classical resolution limit. The classical resolution limit, as we will understand it, is the smallest distance between two scattering objects such that they can be resolved in the far-field. The two objects in the present work are the two edges of the phase structure and for the resolution limit in the course of time different criteria have been derived. One of the most commonly used criteria for optical systems is the two-point resolution limit. By using this criterion, the minimum resolvable distance between two points for an incoherent system reads as $\Delta x = 0.61\frac{\lambda}{NA}$, with NA being the numerical aperture of the system[5]. If the imaging system is aberration-free, the smallest resolvable distance for a given wavelength scales with the numerical aperture, which limits the diffracted spatial frequency transmitted by the system. If the optical system is aberration free, it is also called diffraction limited. Nonetheless, the conclusions of Tychinsky et. al. about the potential to exceed that limit in lateral dimensions were somewhat contradictory and the answer to the question whether it is possible to reach superresolution using phase singularities is still open. They outlined the problem of necessary *a priori* knowledge about the structure, which permits the correct

interpretation of measured phase distributions. Other fundamental problems in using phase information for object reconstruction are the non-trivial response of the object, especially if its feature sizes are comparable to the wavelength. Unfortunately, to the best of the authors' knowledge, no inverse rigorous interaction calculation exists that would permit reconstruction of the object parameters from measured wave-fields and the overall availability of phase contrast. Phase contrast describes the introduced difference in the optical path between the scatterer and its surrounding. The best resolution in terms of phase contrast within the scalar approximation is obtained for π-phase shifting objects. Subsequent investigations by Totzeck and Krumbügel [6] lead to comparable results. Additionally, they applied rigorous diffraction theory in order to compare theory and experiment exactly. In a more recent publication [7] Eberler, Dorn and co-workers investigated the topological behavior of phase-singularities generated by high-permittivity scatterers in reflection. In their conclusion they outlined likewise the necessity of applying rigorous interaction theory in order to enable inference of structural features from measurements. Phase singularities that appear in the transmitted region of a sub-wavelength slit in a silver film have been investigated by Schouten et.al.[8]. In their work the authors analyzed topological events like creation and annihilation by changing the size of the slit.

The present work addresses the derivation of necessary conditions for the appearance of phase singularities generated by a phase bar or phase trench and the topological behavior of these phase singularities after changing object as well as system parameters. We try to find an answer to whether it is possible to resolve objects with feature sizes below the classical diffraction limit (superresolution). We limit our investigation to topological information transported in the far-field, because features below the diffraction limit can be resolved by taking evanescent waves into account [9]. The paper is structured as follows.

In section 2 the basic geometry of the structure under investigation is presented and the numerical tools used are outlined. In section 3 we apply scalar theory to find analytically an inequality which determines the smallest width of a phase bar, introducing a given phase delay, that is capable of generating phase singularities in the far-field. It is shown that a cooperative scatterer (a scatterer which introduces a maximum phase shift of π) must have at least a width of approximately $\frac{\lambda}{4}$, in order to generate phase singularities in the far-field. In section 4 we will investigate the interaction problem rigorously and derive a set of requirements on the object as well as on the system,

in order to generate phase singularities in the far-field with a feature size of the scatterer being as small as possible. This feature size is determined. In section 5 the topological behavior of phase singularities is investigated, by changing a typical object parameter, i.e. its width. In the last section, stability of the position of phase singularities in the presence of neighboring scatterers is discussed.

2 Description of the basic problem and its numerical treatment

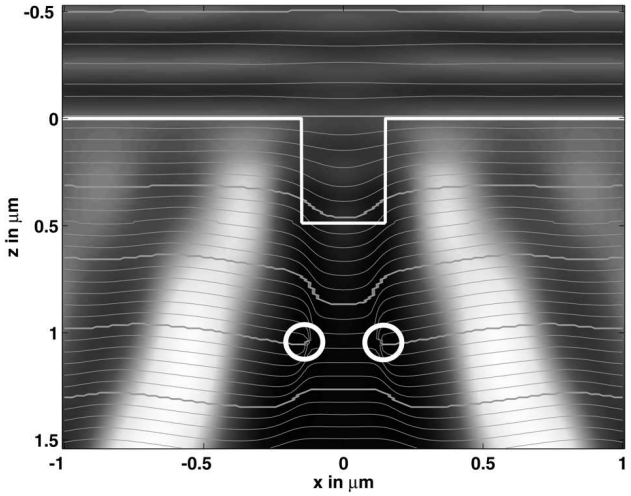

Figure 1: Basic geometry of the problem under investigation: a wave-field illuminates a trench in glass from above. Within the transmitted wave-field phase singularities appear (the relevant ones are marked with small circles). Intensity and isophases are shown, the parameters are given in the text.

Figure 1 depicts an example of the basic setup under investigation. It shows the resulting intensity and phase (isophase) distribution upon interaction of a plane wave with a phase bar. For all the figures the intensity is defined for TE polarization as $EE^\star$ and for TM polarization as $HH^\star$. To simulate realistic objects, the phase bar has been chosen in our investigation not as a free-standing object, but rather as a feature on the surface of a substrate (trench or real bar, we have assumed the typical refractive index

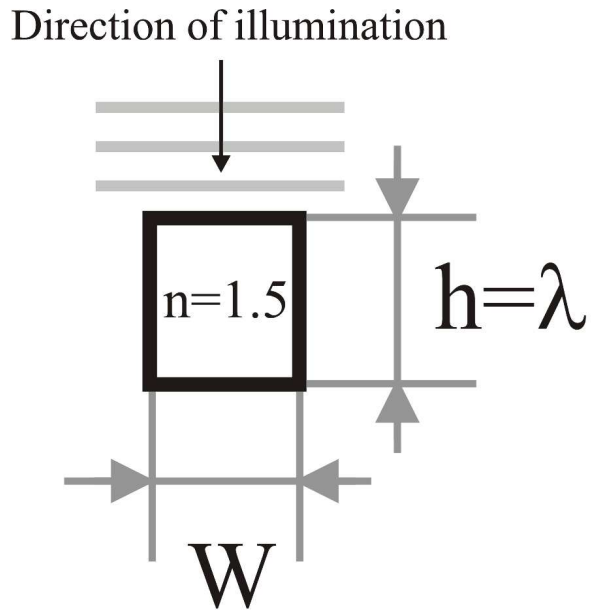

Figure 2: Geometrical setup for calculating the field distribution of a pure single element.

for glass and some plastics of $n = 1.5$). The problem is treated only for two-dimensional objects. They are invariant in the third direction. The trench in the surface (height $h = 0.488\mu m$, width $w = 0.3\mu m$) is illuminated from air along the z-axis by a plane wave (TM polarization). Turbulences appear in the wave-field, introduced by the perturbation. Two small circles mark the two edge-type phase singularities, which are directly related to the perturbation. Comparison of intensity and phase distribution makes it evident that the dislocations are intimately associated with an intensity equal to zero. The entire field distribution is low-pass filtered, assuming a numerical aperture equal to unity. The field in the transmitted region ($z > h$) is therefore in principle accessible by a far-field lens system (such as a high resolution interference microscope working in transmission [10, 11]) and can be measured. In practical applications the absolute position of phase singularities relative to the structure under investigation for measurements in the far-field is the subject of ambiguity, because identification of the reference plane with the desired accuracy is not possible in a simple set-up. Consequently we will investigate the relative distance between dislocations. That procedure is supported by nature, because phase singularities generated by the analyzed

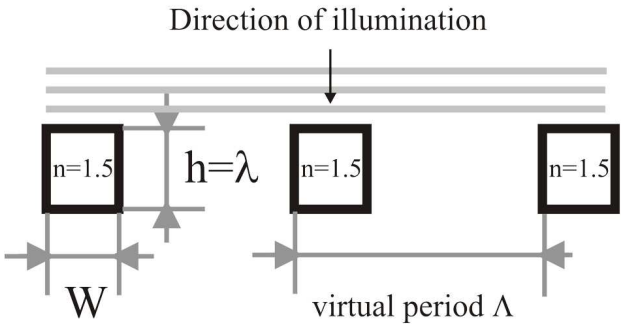

Figure 3: Geometrical setup for calculating the field distribution of a single element with periodic boundary conditions.

structure appear in pairs. It has to be pointed out that edge dislocations can also be generated using holographic optical elements without appearing pair wise[12].

For the numerical simulation of the interaction problem, various techniques have been implemented and tested. Nonetheless, most of the calculations have been made using rigorous grating theories. Details about Rigorous Coupled Wave Analysis (RCWA) and the Fourier Modal Method (FMM) can be found in the literature [13, 14]. They are omitted for reasons of brevity. These theories make use of periodic boundaries, meaning that the structure is considered to extend periodically (the virtual boundary) for an infinite distance outside the region to be calculated. In preliminary computer experiments we have investigated the necessary conditions for the calculation of aperiodic objects. A critical parameter is the virtual period for the object used in the calculation. For the sake of clarity a sketch of the two geometries under consideration is shown. Figure 2 shows the geometry for calculating the field distribution for a pure single element and in Fig. 3 the geometry with periodic boundary conditions. To estimate the influence, least square differences (defined as coupling coefficient $\chi = \frac{1}{w}\int_{-\frac{w}{2}}^{\frac{w}{2}}(u(x,h)_{RCWA} - u(x,h)_{MoM})^2 dx$) between the field of a single element and the field calculated with periodic boundary conditions were specified directly behind the structure as a function of the period. $u(x,h)$ is the E_y component of the field for TE polarization and H_y for TM polarization. The field of the single element (no periodicity) was calculated using the Moment Method [15]. In Fig. 4 the coupling coefficient for a dielectric bar (n=1.5) is shown. It has a height of λ and a width

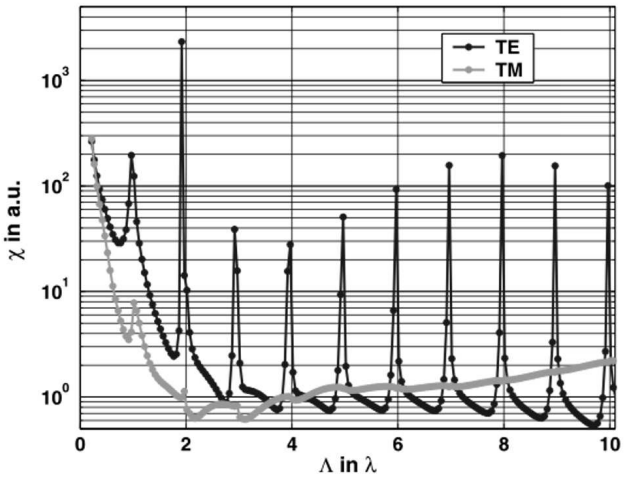

Figure 4: Coupling coefficient of the field behind a rectangular object with $h = \lambda$, $n = 1.5$ and $w = \frac{\lambda}{6}$.

of $\frac{\lambda}{6}$. The bar is illuminated with a plane wave. Figure 5 shows results of the same calculation for a bar having a width of $\frac{\lambda}{2}$. For both figures, the lower the value of χ, the better the periodic simulation matches the single element simulation. It is evident from the calculation that two conditions have to be fulfilled in order to use grating theories for the calculation of single elements. Firstly, one has to choose a period larger than three times the wavelength. Only by using such a period, can near-field coupling among different scatterers be neglected. By violating this condition, the coupling leads to intense and rapid alterations of the wave field as compared with the single element theory. Secondly one has to choose a period in the calculation that is not an integer multiple of the wavelength. That period is critical because a diffraction order will propagate parallel to the grating vector and the resulting field suffers from multiple reflections from neighbouring virtual objects[16].

3 Scalar prediction of smallest feature size capable of generating phase singularities

In this section we will derive analytically the scalar prediction of the smallest width of a phase bar capable of generating phase singularities in the far-field as a function of its phase delay. The derivation starts for simplicity at the

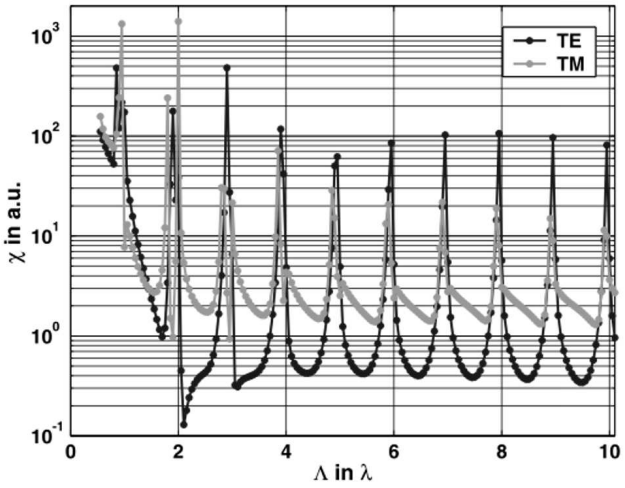

Figure 5: Coupling coefficient of the field behind a rectangular object with $h = \lambda$, $n = 1.5$ and $w = \frac{\lambda}{2}$.

necessary condition for a grating to generate phase singularities. The field of such an object consists of a discrete number of plane waves. As mentioned in the introduction, a phase singularity appears if the field amplitude is equal to zero. This is only possible if the highest amplitude a_n of the diffraction order n is smaller or equal to the sum of all the other amplitudes a_m. This condition reads as [17]

$$\sum_{m \neq n} \mid a_m \mid \geq \mid a_n \mid \qquad \forall n. \tag{1}$$

The highest amplitude in our setup a_n, is always the zero-order. In the absence of any structure, the zero-order is of course the only amplitude with a value different from zero. Introducing a perturbation will couple light into other diffraction orders and the strength of the zero-order will decrease. But it remains the order with the highest amplitude. Once the coupling into other amplitudes suffices to equal the zero-order, condition 1 is fulfilled and a singularity appears. Consequently a_n is always a_0.
To extend the approach to single objects, we calculate the limit of Eq. 1 if the period tends to infinity. The summation becomes an integration and reads as

$$\int_\nu \mid a(\nu) \mid (1 - \delta(\nu - \nu_0))d\nu \geq \int_\nu \mid a(\nu) \mid \delta(\nu - \nu_0)d\nu \qquad \Lambda \to \infty. \tag{2}$$

We will apply the thin element approach for the calculation of the amplitudes of the spatial frequencies. The basic idea of the thin element approach is that the transmitted field is given by a simple multiplication of the incoming wavefield and the transfer function of the structure, thus $F_{Trans}(x) = T(x)F_{Inc}(x)$ The transfer function of the phase bar is

$$T(x) = \begin{cases} e^{i\frac{2\pi h}{\lambda}(n-1)} & \mid x \mid \leq \frac{w}{2} \\ 1 & \mid x \mid > \frac{w}{2} \end{cases} \tag{3}$$

with h the geometrical height. To calculate the far-field response of the structure the amplitudes of evanescent waves are excluded in the summation[18]. By using the thin element approach and equation 2 we derive a condition that determines the smallest width w of a phase bar for a given phase delay $\Delta\phi$, in order to generate a phase singularity. It reads as

$$0 = 1 - \frac{4}{\pi}\sin(\frac{\Delta\phi}{2})\int_0^{\pi w}\frac{\left|sin\left(\frac{t}{\lambda}\right)\right|}{t}dt. \tag{4}$$

Numerical evaluation for the right hand side of Eq. 4 for three different values of an introduced phase delay $\Delta\phi$ are shown in Fig. 6. One can deduce

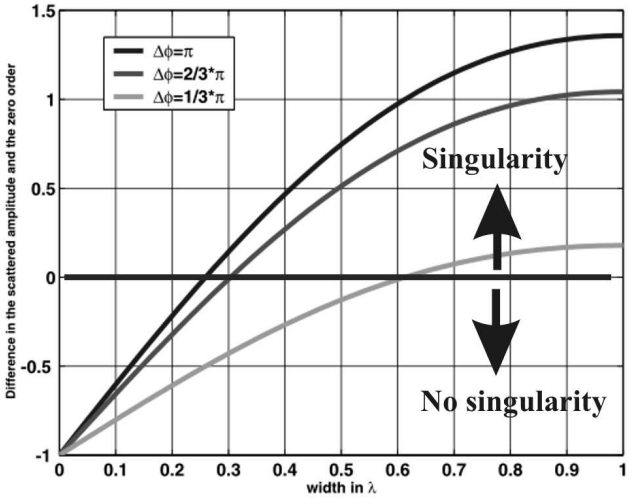

Figure 6: Determination of the smallest width of phase bar which generates phase singularities in the far-field for three different phase delays.

from Fig. 6 that the smallest feature size for a cooperative scatterer $\Delta\phi = \pi$

capable of generating phase singularities in the far field is $\approx \frac{\lambda}{4}$. This is comparable to the diffraction limit. If the introduced phase delay is smaller, a larger width is needed to have a phase singularity in the transmitted field. For further clarification of our analysis, the smallest amplitude in the transmitted field has been calculated for a π-scatterer as a function of its width. The value is shown in Fig. 7 together with the result of Eq. 4. It can be seen

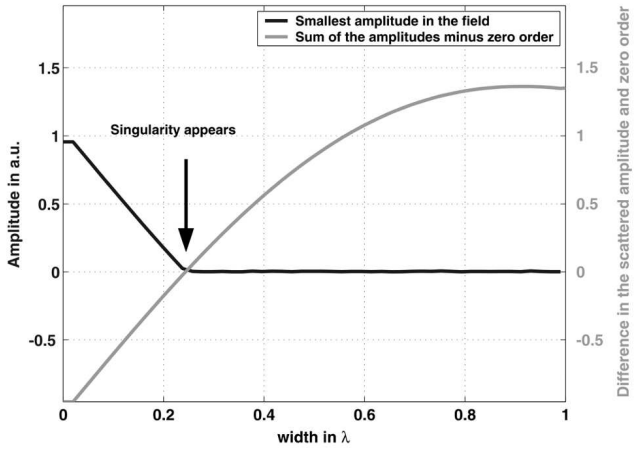

Figure 7: Smallest field-value in the transmission region and difference between the sum of the diffracted amplitudes and the zero amplitude as a function of the width of a trench.

that the width where the field becomes zero coincides with the fulfillment of the condition for the appearance of singularities. Phase singularities are, as mentioned in the introduction, intimately related to a zero amplitude.
In conclusion from the analysis via scalar theory, we have to state that the promise of super resolution using phase singularities as information carriers at least with a single phase bar cannot hold up. They are only generated if the scatterer has a minimum width which is comparable to the diffraction limit. Smaller structures are not capable of doing so.
To treat the problem exactly, we apply in the following section rigorous electromagnetic theory and determine a set of parameters which are beneficial for generating singularities in the far-field with the smallest possible feature size.

4 Rigorous calculation of singularity appearance

4.1 Selection of polarization to illuminate a trench

The main question concerns the sensitivity to different kinds of structures using a wave of either TE (E-field oscillates along the space invariant y-direction) or TM (H-field oscillates along the space invariant y-direction) polarization as the illuminating beam. Sensitivity is for our purpose the possibility that a given object-system configuration can introduce turbulences in the phase distribution of a wave field, which leads to measurable phase singularities in the far-field. Two structures are distinguished. A positive one (trench) and a negative one (bar). Intensity and phase of the field distribution around a trench ($w = 0.2\mu m, h = 0.488\mu m, n_1 = 1, n_2 = 1.5, \Delta\phi = \pi$) illuminated with a TE-polarized plane wave are shown in Fig. 8 a and for TM polarization in Fig. 8 b. Intensity for TE polarization is always defined

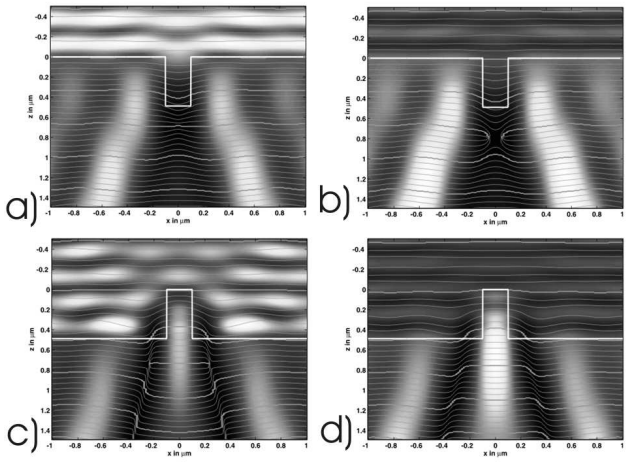

Figure 8: Intensity and phase distribution upon illuminating a trench ($w = 0.2\mu m$) with a TE-polarized plane wave in a, with a TM-polarized wave in b. A bar of the same width is illuminated in c with a TE wave and in d with a TM-polarized wave.

as $I = EE^\star$ and for TM polarization as $I = HH^\star$. Field distributions are low pass filtered assuming again a numerical aperture of one. The wavelength is $\lambda = 0.488\mu m$. Black is equal to an intensity of zero, white is the maximum,

which differs from figure to figure. Comparing the phase distributions after the trench shows that the TM polarization generates singularities, but in TE polarization the transmitted wave field remains plane. No pronounced turbulences appear for TE polarization. Note that the width of the trench in this example is larger than $\frac{\lambda}{4}$.
Explanation for this difference in the response is normally given by using waveguide theory [19]. A trench illuminated with a plane wave can be regarded as a resonator or as a small waveguide consisting of air, which acts differently for TE and TM polarization. If the surrounding material would be a perfect conductor, a TE mode would not be able to propagate within the trench if its width is smaller than $\frac{\lambda}{2}$ (cut-off wavelength). For the TM mode no cut-off wavelength exists, the fundamental mode is always confined. A similar argumentation is true for high index dielectric materials and can be qualitatively applied to the present case. A TM mode excited within the structure receives a certain phase difference upon propagation relative to the field that propagates outside the structure. Interference leads to turbulences and hence to the generation of dislocations. A TE mode is not confined within the trench and hence no significant phase delays are introduced, the phase distribution remains plane. As a consequence, it is preferable to use TM-polarized light to create phase singularities in the far-field generated by a narrow trench.

4.2 Selection of polarization to illuminate a bar

Figures 8 c and 8 d show the resulting field distribution from a bar of width $w = 0.2\mu m$ and height $h = 0.488\mu m, \Delta\phi = \pi$ with a plane TE-polarized (Fig. 8 c) and TM-polarized (Fig. 8 d) wave ($\lambda = 0.488\mu m$) from air to glass. Phase singularities appear if the structure is illuminated with a TE-polarized wave, while for TM polarization the transmitted wave field remains plane and no singularity can be seen. This behavior is opposite to that observed for a trench (Fig. 8 a and b). The explanation is likewise given by using arguments from waveguide theory. In the case of a high permittivity waveguide surrounded by air, a mode is always excited for both polarizations. The difference between the two polarizations is the propagation constant within the structure. The propagation constant is a function of the width and always higher for TE than for TM polarization. Consequently, the excited mode in TE polarization can accumulate a sufficient phase delay faster in order to interfere destructively with the transmitted plane wave in the outer region

for smaller widths. Hence phase singularities are generated earlier in terms of feature size for TE polarization in the case of a bar.
An additional remark about the usefulness of detecting phase singularities, rather than measuring just intensity distributions in the far-field, can be made by comparing intensity and phase in figure 8. The intensity is smeared out over a relatively large area and small variations of object parameters would result in a small change of the intensity distribution, most likely inadequate to determine the variation of the width. On the other hand, the position of a phase singularity as an exact point in the wave field that can be measured with high precision[11] and a small alteration of the objects leads to remarkable changes in the position of dislocations. This question will be discussed in the next section.

5 Smallest feature size that generates phase singularities

We have carefully evaluated the position of phase singularities, which can be directly related to the object under investigation as a function of its characteristic feature size. The case we are mainly investigating is the single trench illuminated with a TM wave. Calculations of absolute values, like distance of the dislocation relative to the structure (taking e.g. $z = 0$ as reference) are not useful, because measurements in the far-field make it impossible to establish the reference plane precisely. Instead, we have used the fact that dislocations appear in pairs with opposite sign and their relative distance in the x-direction is a sufficient criteria, which can also be measured in the far-field without ambiguities. Because their appearance is symmetric, the x-distance between the center of the structure and the dislocation has been calculated. Figure 9 shows the variation as a function of the width of a trench, illuminated with a plane TM-polarized wave. The fields have been low passed filtered using a numerical aperture of unity. The geometrical depth of the structure corresponds to one wavelength, which gives a π-phase shift for $n = 1.5$. Within the scalar approximation this would introduce the strongest phase turbulences. The arrow indicates the birth of the singularities. Values before that point are just distances between the points with highest phase gradient. It can be deduced from the figure that two points in the wave field exist with a highest phase contrast. If the structural feature

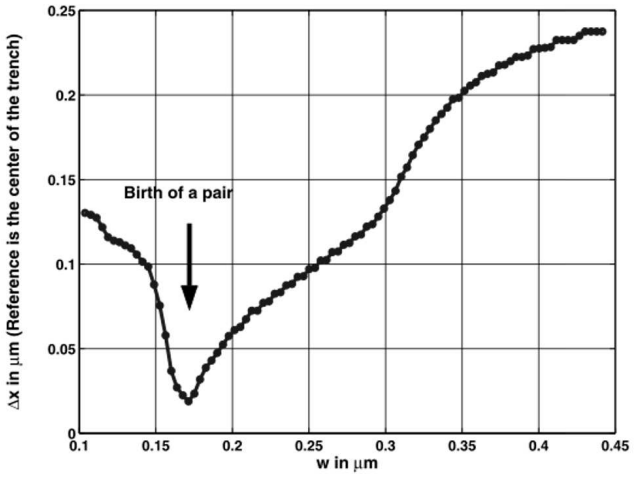

Figure 9: Variation of the x-distance for phase singularities generated by a trench as a function of the width, TM polarization.

reaches a value where the scatterer is capable of generating phase singularities in the far-field, these two points converge geometrically to the same position and the birth of a pair of dislocations takes place. The first phase singularity pair appears for the trench at a width of $0.17\mu m$. This width is larger than $\frac{\lambda}{4} = \frac{0.488\mu m}{4} = 0.12\mu m$. With increasing width, the distance between the dislocations increases quite linearly. It would be possible to deduce the characteristic object parameter by measuring the distance between the dislocations and using *a priori* knowledge about the structure. Such supplementary information on the structures are e.g. the index of refraction of the material or the height of the object, because they have a significant influence on the distance between the dislocations. This information can be obtained from separate measurements or is known from the fabrication process and will hence simplify the precise determination of the unknown parameter. Additionally, it is in principle possible that different basic geometrical structures might generate the same pair of dislocations. To decide which geometry is the correct one, we have to know something about the geometry to exclude the implausible objects.

We deduce as the smallest feature size capable of generating phase singularities an object with a characteristic width of larger than $\frac{\lambda}{4}$, the predicted value of the scalar theory. This is due to the fact that the induced phase delay is not exactly π and the entire field distribution is smeared out while passing

through the structure[20]. Smaller objects will not give strong gradients in the phase field.
Similar investigations have been made for a phase bar illuminated with a TE-polarized plane wave. All the other parameters remain constant. The behavior is different, as can be seen from Fig. 10 a where a field distribution shortly after the birth of the singularity is shown. The width of the bar is

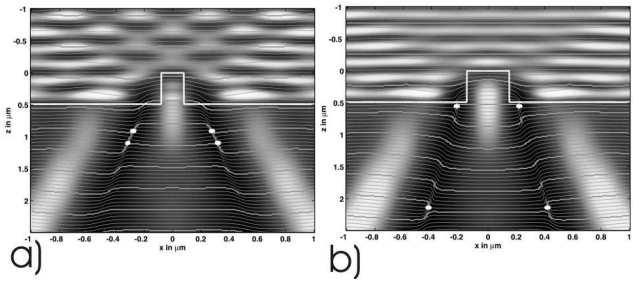

Figure 10: Intensity and phase after illuminating a bar ($w = 0.16\mu m$ in a and $w = 0.3\mu m$ in b, $h = 0.488\mu m$) with a TE plane wave ($\lambda = 0.488\mu m$).

$w = 0.16\mu m$. Surprisingly, we found the same value for the smallest feature size capable of generating phase singularities in the far-field. But there is not a single pair but two pairs as for trenches. One can be found left of the structure, the other on the right. Figure 10 b shows the topological alteration of the wave field if the width is changed to $w = 0.3\mu m$. The x-position of the singularities will change only negligibly. The main alteration takes place in the z-position. For completeness, Fig. 11 shows the z-distance between the two singularities as a function of the width of the bar. A TE-polarized plane wave was assumed for the illumination. In a way comparable to Fig. 9, it can be seen again that shortly after the birth the distance between the two singularities grows rapidly and will increase for somewhat larger phase bars to a good approximation linearly with the width. Measurement of these z-distances with high resolution is more time consuming, because a large space has to be scanned, but it is in principle possible [11].
It has to be stressed that all the values found are correct only for a refractive index equal to 1.5. If stronger scatterers are used, the non linearities appearing in the interaction are more pronounced and objects with a geometrical feature size smaller than $\frac{\lambda}{4}$ can generate phase singularities[21]. For optical systems having a numerical aperture smaller than unity, the lateral feature size for which a singularity appears in the diffracted field will be larger, but

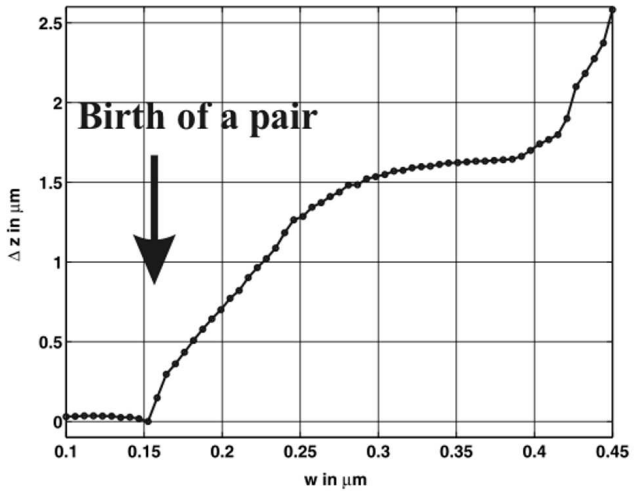

Figure 11: Variation of the z-distance for phase singularities generated by a bar as a function of the width, TE polarization.

the subsequent linear relation between the width of the structure and the distance between the pair of singularities will remain[10].
To establish a relation between the distance of dislocations and unknown object parameters a second problem has to be investigated. This problem is the influence on the local position of the singularity if the system consists of more than one defect that serves as a scatterer in the closer surroundings. Simulation and discussions about the local stability of a phase singularity as a function of neighboring scatterers will be treated in the next section.

6 Stability of phase singularities in the presence of additional structures

First of all, in order to reduce the influence of scatterers in the closer surroundings, a Gaussian-distributed TE-polarized beam ($\sigma = 0.488\mu m = \lambda$, waist at $z = 0$) has been used for illumination. We restrict ourselves to diffraction at a trench with neighbouring trenches. The principal conclusions hold likewise for bars. TE polarization was used in the calculation because we can take advantage of faster computational procedure. A slightly larger width of the trench than the one necessary for the appearance of dislocations has been chosen. In Fig. 12 the change in the x-distance between the relevant

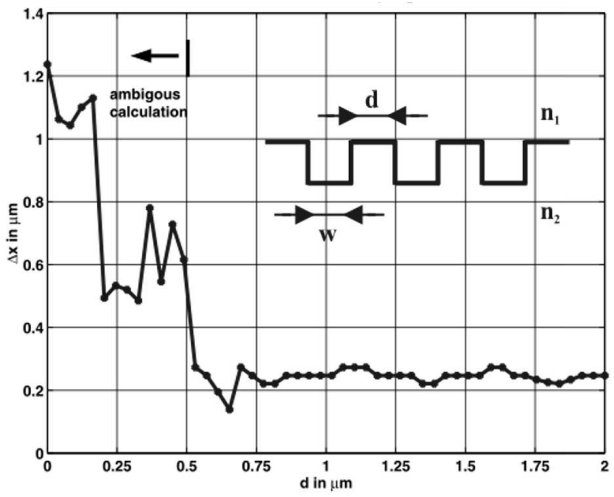

Figure 12: Variation of the distance Δx between two dislocations generated by a trench of width $w = 0.35\mu m$ as a function of the separation d for two additional equal trenches.

phase singularities as a function of the distance d between the central and the two neighbouring trenches is shown (the geometry is shown explicitly in the inset of Fig. 12). The width of the trenches is $0.35\mu m$, the height of the structure is $0.488\mu m$ and the direction of the illumination goes from air ($n_1 = 1$) to glass ($n_2 = 1.5$). Ambiguous calculation, as indicated in the figure, means that the dislocation vanished either completely or its position can be just located outside the computational window. In both cases, identification of gradients in the phase distribution relative to the structure turns out to be cumbersome. We see that as long as the distance between the trenches is larger than the waist of the laser their position remains fairly stable. If the trenches are too close, coupling effects have a major impact on the resulting phase distribution and the position of the dislocation can no longer be linked in a simple manner to the structural feature. A re-calculation with increased resolution for distances far from the coupling region is shown in Fig. 13. From that and similar calculation we have found that the distance Δx between the perturbed dislocations oscillates more or less sinusoidally around the distance one would see for the unperturbed case. With increased distance the amplitude of the oscillation will be reduced. This behavior is attributed to components of the wave field that are reflected back and forth by

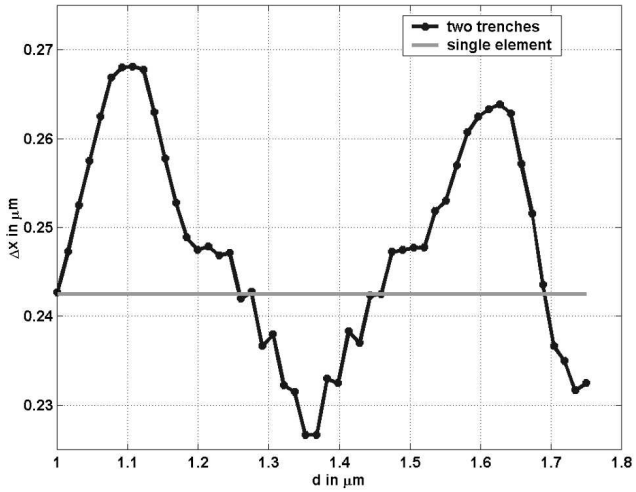

Figure 13: Magnified distance variation from the example of Fig. 12 for a separation larger than a micron.

the structures. Alteration of the distance between the trenches will change the optical path. Resulting variations between constructive and destructive interference of the diffracted wave will lead to the observed sinusoidal changes in the distance between dislocations.
If the optical system has a numerical aperture smaller than unity, the distance between the singularities for a given geometrical configuration is smaller. The influence of neighboring scatterers will be likewise negligible as long as the distance is larger than the waist of the laser. An excessive decrease will lead to the annihilation of the singularities. In each case one has to compare the measurements with a calculation, assuming the specific set-up that was used in the experiment.

7 Summary

In the present work we have derived conditions for the appearance of phase singularities as a function of object and system parameters for a phase bar and trench in transmission. By applying scalar theory to the problem we have shown that the smallest width of a scatterer capable of generating singularities is somewhat wider than $\frac{\lambda}{4}$. This is comparable to the diffraction limit. We have applied rigorous electromagnetic theory to demonstrate the differ-

ence between a phase bar and a trench, both having the same phase delay. Likewise, we have shown that the smallest feature size capable of generating phase singularities in a rigorous calculation is comparable to the classical resolution limit, but larger than the predicted scalar value. If the structures are too small, no turbulences in the phase distribution can be generated. To have a singularity in the field, a point with zero intensity is required. Only relatively strong scatterers are capable of doing so. The explanation of the overall behavior has been given using arguments from waveguide theory. Nonetheless, once phase singularities appear, they will change their position quite rapidly by changing an object parameter. For the bar, the change in position is mainly in the z-direction, for the trench mainly in the x-direction. Illuminating the object under investigation with a focused gaussian beam suppresses the influence on the position of generated phase singularities by neighboring objects. Only a resulting slightly sinusoidal variation of the position by changing the distance between neighboring scatterers remains. This is attributed to waves which are reflected back and forth by the structures.

8 Acknowledgments

The research was supported by the European Union within the framework of the Future and Emerging Technologies-SLAM program under grant No. IST-2000-26479.

References

[1] J.F. Nye and M.V. Berry, Proc. R. Soc. London A, **336**, 165, (1979)

[2] N.B. Baranova, A.V. Mamaev, N.F. Polopetsky, V.V. Shkunov and B.Y. Zel'dovich, J. Opt. Soc. Am., **73**, 525, (1983)

[3] V.P. Tychinsky, Opt. Commun., **74**, 41, (1989)

[4] V.P. Tychinsky, I.N. Masalov, V.P. Pankov and D.V. Ublinsky, Opt. Commun., **74**, 37, (1989)

[5] J. W. Goodman, *"Introduction to Fourier Optics"*, 2nd edition, McGraw-Hill (1996)

[6] M. Totzeck and M.A. Krumbügel, Opt. Commun., **112**, 189, (1994)

[7] M. Eberler, R. Dorn, B.Münzer, S. Quabis and G. Leuchs, Proceedings of the World Conference on Systematics, Cybernetics and Informatics, Orlando (2000)

[8] H.F. Schouten, G. Gbur, T.D. Visser, D. Lenstra and H. Blok, Opt. Express, **11**, 371, (2003)

[9] J.P. Fillard, *Near Filed Optics and Nanoscopy*, 1st edition, World Scientific (1997)

[10] R. Dändliker, P. Blattner, C. Rockstuhl and H.P. Herzig, *Singular optics (optical vortices): fundamentals and applications*, SPIE Proc. **4403**, 257, (2000)

[11] C. Rockstuhl, M. Salt, H.P. Herzig, *Theoretical and experimental investigation of phase singularities generated by optical micro- and nanostructures*, accepted for publication in J. Opt. A: Pure Appl. Opt.

[12] I. V. Basistiy, M. S. Soskin and M. V. Vasnetsov, Opt. Commun., **119**, 604, (1995)

[13] J. Turunen. *"Micro-Optics: Elements, Systems and Applications"*, chapter Diffraction Theory of Microrelief Gratings, H.P. Herzig, ed., Taylor & Francis (1997)

[14] M.G. Moharam and T.K. Gaylord, J. Opt. Soc. Am., Vol., **71**, 811, (1981)

[15] M. Totzeck and H.J. Tiziani, Opt. Commun., **136**, 61, (1997)

[16] P. Blattner and H.P. Herzig, J. of Mod. Opt., **45**, 1395, (1998)

[17] P. Blattner, *"Light field emerging from periodic optical microstructures"* PhD Thesis, Ch. 5, University of Neuchâtel, Switzerland, (1999)

[18] M. Born and E. Wolf, *"Principles of Optics"*, 6th edition, Cambridge University Press (1999)

[19] M. Totzeck, H. Jacobsen and H.J. Tiziani, *Advanced Photonic Sensors and Applications*, SPIE Proc. **3897**, 424, (1999)

[20] C.M.J. Mecca, Y. Li and E. Wold, Opt. Commun., **182**, 265, (1996)

[21] R. Dorn, M. Eberler, M. Piringer, S. Quabis and G. Leuchs, Technisches Messen **67**, 421, (2000)

High-resolution measurement of phase singularities produced by computer-generated holograms

Carsten Rockstuhl[1], Andrey Albert Ivanovskyy[2], Marat Samuil Soskin[3], Martin Guy Salt[1], Hans Peter Herzig[1] and Rene Dändliker[1]

[1]University of Neuchâtel, Institute of Microtechnology, Rue A.-L. Breguet 2, CH-2000 Neuchâtel, Switzerland

[2]Physical & engineering education & scientific center of the National Academy of Sciences of Ukraine, 36 Academika Vernadskogo Avenue, 03142, Kiev, Ukraine

[3] Institute of Physics of the National Academy of Sciences of Ukraine, 46 Prospect Nauki, 03680, Kiev, Ukraine

October 15, 2004

Abstract

We present measurements of the intensity as well as the phase distribution in the various diffraction orders of computer generated holograms designed to generate a higher order Gauss-Laguerre beam. For the direct measurement of the phase distribution in the diffraction orders a high resolution interferometer is used, which allows access to a lateral length scale for the localization of phase singularities below the wavelength. It is experimentally shown that in beams that carry multiple singularities, the dislocations do not degenerate. This effect cannot be seen by analyzing only the intensity distribution of the laser beam.

PACS: 42.40.J, 42.87.B

Keywords: Computer generated holograms, Phase singularities, High-Resolution Microscopy

1 Introduction

Phase singularities are points in space where the real and imaginary parts of a scalar component of the electromagnetic field vanishes: the amplitude is zero, the phase is not determined and its gradient becomes infinite[1]. Basically, one distinguishes between edge dislocations and screw dislocations. An edge dislocation is a line singularity perpendicular to the propagation direction along which the phase has a discontinuity and jumps by π. They appear in nature, e.g. in Gauss-Hermite laser modes, for which the field is zero along discrete lines. Along these lines the phase is not defined.
Screw dislocations are line singularities parallel to the propagation direction[2], which appears as a point if the phase is measured in a plane perpendicular to the propagation direction. The phase on a closed circle around this point will change by a multiple m of 2π, with m being the strength of the dislocation, also called the charge[3]. In nature they appear in speckle fields for example[4]. Laser beams that carry screw dislocations can be generated in a controlled manner within laser resonators[5], by appropriate phase plates[6, 7], by combining the two method[8], or by computer generated holograms(CGH)[9], amongst other methods. Beams with this kind of singularity find manifold applications, e.g. for the trapping of particles[10] or atoms[11].
The measurement of the generated phase distribution is normally deduced from intensity recordings of the interference patterns between the beam that carries the dislocations and a tilted reference plane wave, a technique called fork interferometry[3]. The straight lines of constructive and destructive interference are disordered at the point of the singularity and m lines either appear or vanish. The position of the singularities can be found with a resolution that depends basically on the angle between object and reference beam. However, the angular difference between the two beams is fairly usually low and a resolution in the order of tens of micrometers is typically achieved.
We use a high-resolution interference microscope to measure the phase distribution in the different diffraction orders of a CGH designed to generate Gauss-Laguerre beams in the first order[1]. Such a type of interferometer has been used in the past to analyze with high precision the amplitude and phase distribution around single micro-structures[12, 13], periodic objects[14] and

[1]A brief mathematical description of Gauss-Hermite and Gauss-Laguerre laser beams can be found in appendix II.

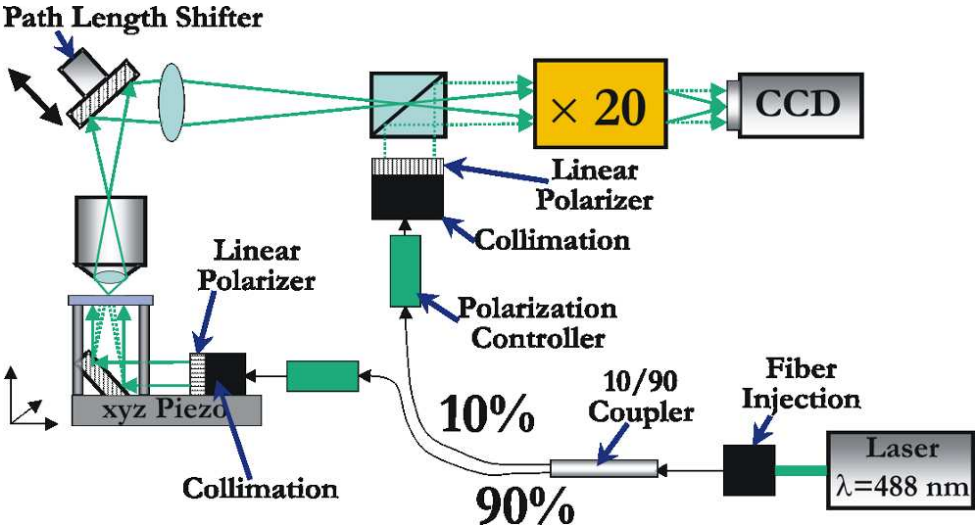

Figure 1: Experimental setup of the Mach-Zehnder interferometer.

in the focal region of microlenses[15] in which phase singularities of the edge type appear. We will understand the resolution of the microscope to be its capability to determine the position of the phase singularities. Such a definition of the resolution will not violate that classical resolution limit(e.g. the two-point resolution criteria), as we intend to analyze the phase distribution in a wave-field that has no physical counterpart in the object plane. This resolution is limited by technological constrains that correspond in the present case to a few pixels of the CCD-Camera. A pixel corresponds approximately to 100 nm in the object plane[16].

2 Experimental setup

The experimental setup of the Mach-Zehnder interferometer is shown in Fig. 1. As a coherent light source for the microscope we have used an Argon laser that emits at $\lambda = 488\ nm$. For practical reasons the beam is coupled into a mono-mode fiber. The object and reference beam are split at an integrated beam splitter by a ratio of 90/10 and the polarization of both beams can be adjusted at the exit of the fiber for optimizing the contrast of the resulting interference fringes. The sample is placed on a piezo-stage that permits the local positioning of the CGH in all three spatial directions.

Collimating optics are placed at the exit of the fibers in the object and in the reference arm. In the object arm, the beam is focused on the sample such that ideally the waist of the Gaussian beam is in the object plane. The optics in the reference arm can be used to minimize the difference in the curvature between the reference and object wave. The microscope consists of two stages: The first is a telescopic system with a $10\times$ objective and a 250 mm lens. At an intermediate plane an aperture is positioned that allows selection of a single diffraction order for analysis. We have chosen such a weak objective in order to avoid interference between neighboring diffraction orders that would appear if the first magnification were stronger. After superposition with the reference wave, a similar optical system with a $20\times$ objective magnifies the intermediate image in a second step. The measured interference images in the waist of the magnified laser beam are recorded with an 8-bit CCD camera and the phase distributions are calculated using a five-step phase algorithm[17]. The two combined telescopic systems allow a magnification such that a CCD-pixel corresponds to 100 nm in the object plane.

We have investigated two different computer-generated holograms (CGHs) that have been designed to produce as off-axis holograms Gauss-Laguerre beams with the orders $(p = 0, m = 1)$ and $(p = 0, m = 2)$, respectively[18], p being the radial mode parameter and m the azimuthal mode parameter. The second parameter m corresponds to the strength of the singularity[19]. The patterns of the binary computer-generated hologram have been deduced from the calculated lines of constructive interference between the laser modes to be generated and the plane reference wave propagating under a design angle relative to the laser mode of $\tan\theta = \lambda/\Lambda$[3]. The period of the resulting grating is Λ and the first diffraction order will propagate at an angle of θ with respect to the optical axis. The holograms were printed using a photocomposer and subsequently reduced in a photolithographic process by a factor of ten and then imaged on a substrate covered with photoresist. After developing the samples, the CGHs can be used as phase-only objects in transmission. The period of the samples used for the measurement was 10 μm and the depth was approximately 600 nm, as deduced by measurements with an atomic force microscope (AFM).

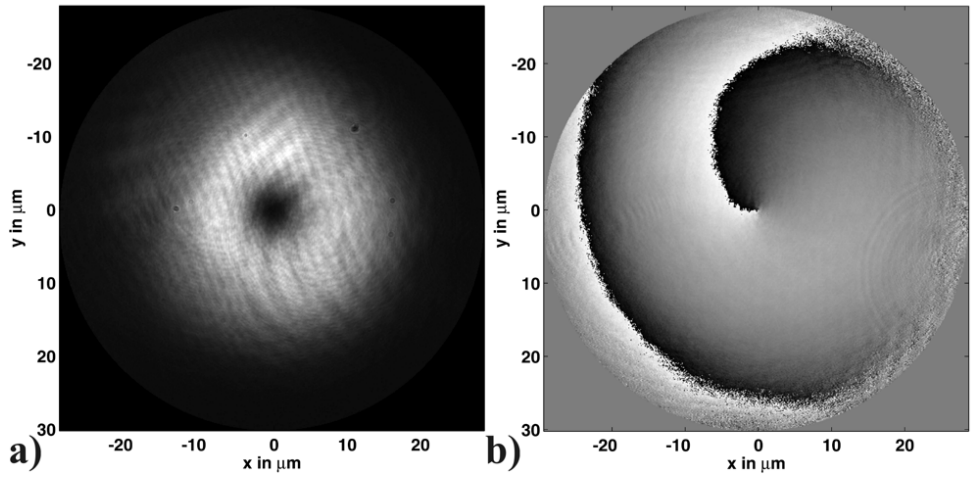

Figure 2: Measured (a) intensity and (b) phase distribution in the +1 diffraction order of the GL01-CGH.

3 Results

3.1 Gauss-Laguerre mode 01

Figure 2 a) shows the measured intensity distribution in the +1 diffraction order of the hologram that generates a Gauss-Laguerre 01 beam. The ring-shaped intensity distribution of the doughnut laser mode can be seen, with an intensity zero in the center of the beam[2]. The measured corresponding phase distribution is shown in Fig.2 b). In all the figures, which show a phase distribution, black corresponds to a phase value of $-\pi$ and white to π. A difference in the radius of curvature between the wave in the object and in the reference arm will cause the slightly spiral-like distortion of the phase distribution. Without such a misalignment, the iso-phases would be straight radial lines, originating from the center of the beam, where the dislocation is situated. The strength of the dislocation for the generated laser mode is -1. We use a positive sign for the dislocations if the singularity produces a right screw, and a negative sign for the opposite case. However, due to conservation of the sum of charges in a wave-field, in the negative diffraction order a similar beam is generated that has for a perfect binary

[2]The theoretical predicted intensity and phase distributions of the measured laser beams are shown in appendix II for comparison with the experimental results.

grating the same intensity distribution but the strength of the singularity in the beam center has the opposite sign. This will be shown in the following measurements. The position of the origin for the dislocation can be determined with a precision of a few pixels of the CCD-camera ($< 3Pixel$) and is limited by the optical noise in the measurements and the number of discretization levels of the CCD-camera. In the case where we want to record the entire intensity distribution of the beam, saturation of the CCD-camera is avoided by the adjustment of the gain factor. This limits the resolution, because all intensity values below a half discretization step are clipped to zero intensity. The size of the corresponding region can be regarded as the resolution limit for the position of the singularity. The advantage of measuring the phase distribution, instead of only the intensity distribution, is the elimination of incoherent background. This contribution smears out the otherwise well-defined minimum intensity and an exact determination of the position of the singularity is not possible. If one limits the observation to the singularity and its neighborhood, the gain of the CCD-camera and the power of the laser illumination can be increased, such that the ultimate limit for the resolution is given by a single pixel of the CCD-camera.

3.2 Gauss-Laguerre mode 02

Figure 3 a) shows the measured intensity distribution in the -2 order of the CGH, and Fig. 3 b) shows the corresponding measured phase distribution. The intensity distribution has again a doughnut-like shape. By comparing the intensity distribution in the second order with the intensity from the first order (Fig. 2 a), it can be seen that the dark core is somewhat broader and the bright ring is thinner, which corresponds to the intensity signature of a Gauss-Laguerre mode of a higher azimuthal mode parameter. In the phase distribution, two easily distinguishable phase singularities appear with the same strength, which proves the excitation of a GL02 mode. The strength for each of the two dislocations is +1 and they are separated by approximately 2.5 μm.

The appearance of such a beam having two dislocations can be explained as follows. The phase difference between two subsequent diffraction orders is exactly equal to one wavelength. This means that the screw-like phase distribution produced by the CGH has an additional 2π phase shift. This will lead to a beam in the second order which carries a singularity that has twice the

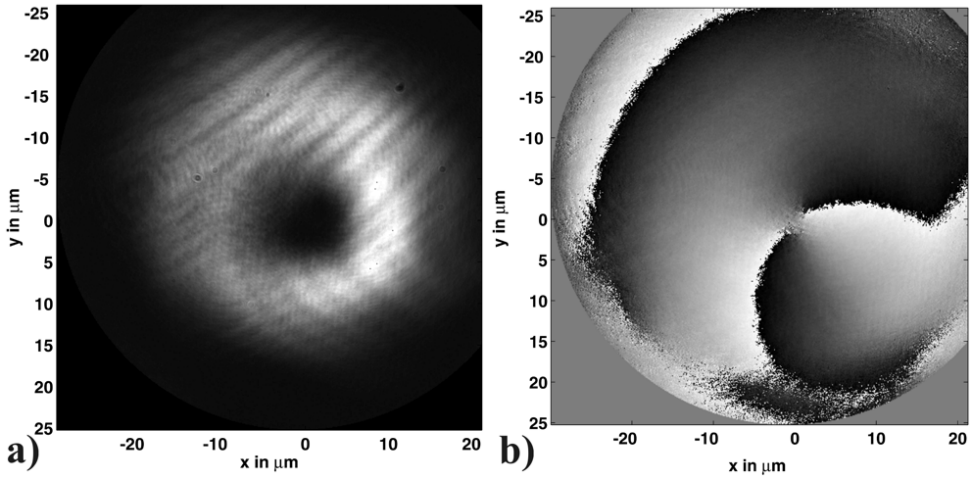

Figure 3: Measured (a) intensity and (b) phase distribution in the -2 diffraction order of the GL01-CGH.

strength of the singularity generated in the first diffraction order. The generated beam can be regarded principally as a superposition of propagation invariant modes. Assuming Gauss-Laguerre modes as the basis for the mode expansion, the mode which corresponds to the induced phase distribution in the present case is a GL02 mode(the second diffraction order of a hologram designed to produce a GL01 mode in the first order). Correspondingly it will be the laser mode with the strongest fractional power. But the mode conversion is incomplete, for two reasons. The first is the non-optimized height of the structure, which will not induce a perfect screw into the phase distribution. Additional modes are excited and interfere with the dominant mode. The second reason for a non-perfect generation of the GL02 mode is the mismatch between the amplitude distribution of the illuminating mode and the GL02 mode. This will lead additionally to the excitation of other modes. Both effects will cause the GL02 to be perturbed and the dislocation, which originally has a charge of +2, will be split into the observed two dislocations. Both singularities have a charge of +1.
By plotting the logarithm of the intensity and the iso-phases on the same figure, as shown in Fig. 4, it can be seen that the positions of the singularity and the minimum of the beam can be located at the same position. The thick line corresponds to the change of 2π in the phase. It must been mentioned that the region with the intensity minimum is smeared out and the absolute

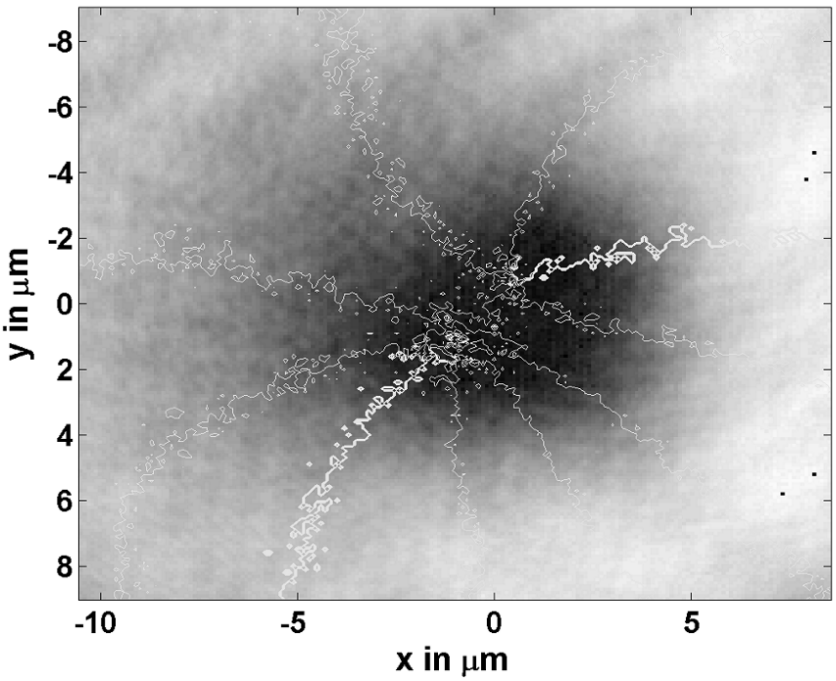

Figure 4: Logarithm of the intensity and iso-phases for the measured field distribution in the -2 diffraction order of the GL01-CGH.

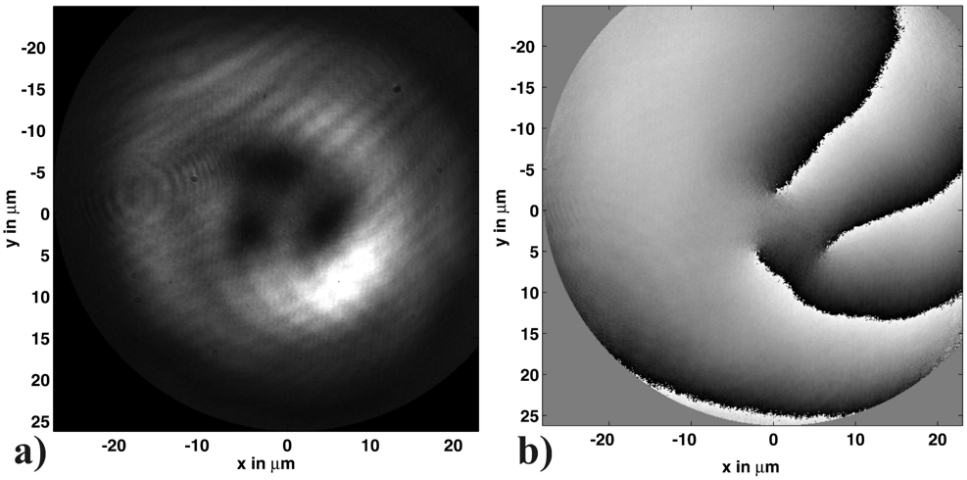

Figure 5: Measured (a) intensity and (b) phase distribution in the -3 diffraction order of the GL01-CGH.

minimum cannot be determined. In the phase distribution, however, the position of the two singularities can be distinguished clearly, even for a spacing as small as $2.5\mu m$.

3.3 Gauss-Laguerre mode 03

The intensity and phase distribution in the -3 diffraction order is shown in Fig. 5. The generated beam contains three singularities with a charge of 1 each. The separation of the dislocations is increased compared with the measurements in the second order and is between 6 μm and 8 μm. The beam is dominated by the contribution from a GL03 mode, but the distribution is perturbed by significant contributions from other modes. This can be also seen in the intensity, where the ring-shaped distribution is broken and the dark core of the beam shows three well-defined local minima. The points with the lowest intensity coincide perfectly with the position of the dislocations, determined more precisely from the phase distribution. The distribution can be regarded as a superposition of a GL03 mode with a GL00 mode as explained before. The coherent superposition of the laser beams will cause a deviation from the radially symmetric intensity distribution due to constructive and destructive interference.

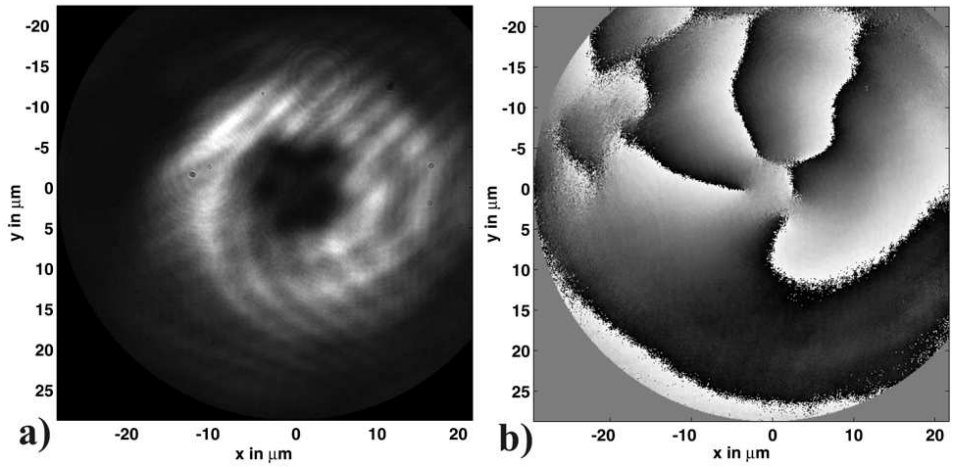

Figure 6: Measured (a) intensity and (b) phase distribution in the +2 diffraction order of the GL02-CGH.

3.4 Gauss-Laguerre mode 04

Modes with a still higher number of dislocations have been generated by using a CGH that was designed to transform a Gaussian beam into a Gauss-Laguerre 02 mode for the first diffraction order. Measuring the field-distribution in the second diffraction order, a dominant GL04 mode is seen. The mechanism for the excitation is comparable to the described mode excitation in the second order of the previous hologram (GL01-CGH). The induced phase delay for the second order is twice that of the first order. Therefore, the screw-like phase delay transferred to this beam is $2 \times 4\pi$. Correspondingly, such a mode carries four dislocations. In Fig. 6, the measured intensity and phase distribution of such a beam are shown. The low contrast fringes in the intensity distribution originate from interference of the primary beam with scattered light of other diffraction orders. The origin of the scattered light is insufficient filtering of the diffraction order by the aperture. In the experiments, the higher diffraction orders are not clearly distinguishable and rather elongated. If the aperture is adjusted to a diameter that is too small, this unwanted scattered light is blocked but a significant portion of the laser beam is also lost.

In the phase distribution, the four singularities can be distinguished clearly and correspond to local intensity minima in Fig. 6 a).

4 Conclusions

In this paper we have presented direct measurements of the intensity and phase distribution in the different diffraction orders of computer-generated holograms. They have been intentionally designed to work off-axis as mode transformers in first diffraction. It has been shown that in the higher diffraction orders, beams can be observed with an integer multiple of the singularity of the first diffraction order beam. The sign of the strength in the negative diffraction orders is the opposite of the strength from the singularities in the positive diffraction orders. The phase singularities of higher orders are not observed clearly. Due to excitation of other beam modes in the system, the singularity is split into a number of closely spaced singularities, each with a strength of unity. Using a high resolution interference microscope, they can be well discriminated.
These findings helps to understand the limitations for practical applications of higher-order singularities. Such a higher order Gauss-Laguerre beam is for example applied as an optical tweezer for the trapping of particles with an index lower than the refractive index of the surrounding. These particles can be stably trapped in the dark core of the laser beam. For higher order modes the trapping efficiency is better because the gradient of the absolute value of the electric field is higher. However, if the singularities do not coincide, different points of stable trapping might exist in the beam. This will cause an instability in the particle position, which is undesired in high-precision applications.

5 Acknowledgments

The research was supported by the European Union within the framework of the Future and Emerging Technologies-SLAM program under grant No. IST-2000-26479.

References

[1] J.F. Nye and M.V. Berry, Proc. R. Soc. London, **A 336**, 165, 1974

[2] I.V. Basisty, V.Yu. Bazhenov, M.S. Soskin and M.V. Vasnetsov, Opt. Commun., **103**, 422, (1993)

[3] I.V. Basisty, M.S. Soskin and M.V. Vasnetsov, Opt. Commun., **119**, 604, (1995)

[4] N.B. Baranova, A.V. Mamaev, N.-F. Philipetsky,V.V. Shkunov, B.Ya. Zel'dovich, JOSA, **73**, 525, (1983)

[5] M. Harris, C. A. Hill and J. M. Vaughan, Opt. Commun., **106**, 161, (1994)

[6] M. W. Beijersbergen, R. P. C. Coerwinkel, M. Kristensen and J. P. Woerdman, Opt. Commun., **112**, 321, (1994)

[7] G. Machavariani, N. Davidson, E. Hasman, S. Blit, A. A. Ishaaya and A. A. Friesem, Opt. Commun., **209**, 265, (2002)

[8] R. Oron, N. Davidson, A. A. Friesem and E. Hasman, Opt. Commun., **182**, 205, (2000)

[9] D. Rozas, Z. S. Sacks, and G. A. Swartzlander, Jr., Phys. Rev. Lett., **79**, 3399, (1997)

[10] D. G. Grier, Nature, **424**, 810, (2003)

[11] T. Kuga, Y. Torii, N. Shiokawa and T. Hirano, Phys. Rev. Lett., **78**, 4713, (1997)

[12] M. Totzeck and H. J. Tiziani, Opt. Commun., **136**, 61, (1997)

[13] M. Eberler, R. Dorn, B.Münzer, S. Quabis and G. Leuchs, *Proceedings of the World Conference on Systematics, Cybernetics and Informatics, Orlando*, 138, (2001).

[14] R. Dändliker, P. Blattner, C. Rockstuhl and H.P. Herzig, *Singular optics (optical vortices): fundamentals and applications*, SPIE Proc., **4403**, 257, (2000)

[15] R. Dändliker, I. Märki, M. Salt and A. Nesci, J. Opt. A: Pure Appl. Opt., **6**, S189, (2004)

[16] C. Rockstuhl, M. Salt and H.P. Herzig, J. Opt. A: Pure Appl. Opt., **6**, S271, (2004)

[17] J. Schwider, R. Burow, K. E. Elssner, J. Grzanna, R. Spolaczyk, and K. Merkel, Appl. Opt., **22**, 3421 (1983)

[18] A. E. Siegman, *"Lasers."*, University Science Books, Mill Valey, California, (1986)

[19] A. A. Ivanovskyy, I. V. Basistiy and M. S. Soskin, Semiconductor Physics and Quantum Electronics Journal 2, **6**, 246, (2003)

Appendix I

The Boundary Element Method

The basic two-dimensional scattering problem is depicted in Fig. 1. The structure is invariant in the third dimension. A homogenous scatter having a relative permittivity of $_I$ is described by its contour C and is illuminated by an incident wave-field $u^{inc}(\ )$ from a region with a homogenous permittivity $_0$. (x, y) is an observation point. If the incoming field is TE-polarized, the field component $u(\ )$ denotes the $E_z(\ )$ component of the electric field. If the field is TM-polarized, $u(\ )$ denotes the magnetic field component $H_z(\ )$. For both cases the total field, $u^{tot}(\ )$, is the sum of the incoming field $u^{inc}(\ )$ and the scattered field $u^{sc}(\ )$. It is assumed that the materials are non-magnetic, i.e. $_r = 1$.

The total field in the interior region has to be a solution of a homogeneous wave equation, in the exterior region a solution of an inhomogeneous wave equation. This is due to the presence of an additional source term, which is defined on a circle in infinity. The wave equations read as

$$\begin{aligned} 0 &= \nabla^2 u_I^{tot}(\ ) + k_I^2 u_I^{tot}(\ ) \quad \text{for} \quad \in I \\ f(\ ) &= \nabla^2 u_O^{tot}(\ ) + k_O^2 u_O^{tot}(\ ) \quad \text{for} \quad \in O, \end{aligned} \tag{1}$$

with $k_{I,O} = \frac{2\sqrt{\ _{I,O}}}{\overset{0}{O}}$ being the wave number in the interior (I) and respectively exterior (O) region. Applying Greens Second Identity [1], the equations can be written as the boundary integral equations

$$\begin{aligned} u_I^{tot}(\ ) &= \int_C \ G_I(\ ,\ ')v_I^{tot}(\ ') \quad u_I^{tot}(\ ')\frac{\partial G_I(\ ,\ ')}{\partial \hat{n}_I}\Bigg) dl' \quad \text{for} \quad \in I \\ u_O^{tot}(\ ) &= u_O^{inc}(\ ) + \ \int_C + \int_{C\infty} \\ &\qquad G_O(\ ,\ ')v_O^{tot}(\ ') \quad u_O^{tot}(\ ')\frac{\partial G_O(\ ,\ ')}{\partial \hat{n}_I}\Bigg) dl' \quad \text{for} \quad \in O, \end{aligned}$$

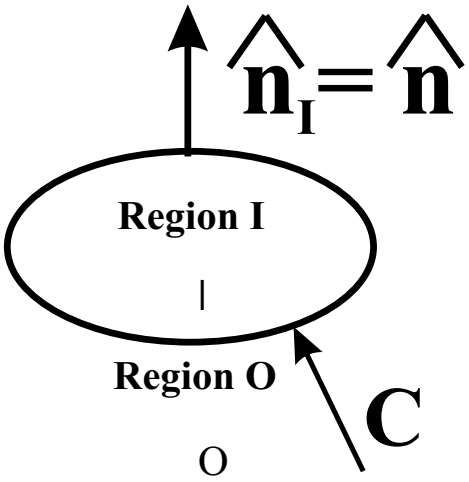

Figure 1: ***Basic geometry treated within the Boundary Element Method.***

(2)

where the field derivative $v^{tot}_{I,\,O}(\ \ )$ is given by

$$v^{tot}_{I,\,O}(\ \ ) = \frac{\partial u^{tot}_{I,\,O}(\ \ )}{\partial \hat{n}_{I,\,O}} \tag{3}$$

and the incoming field reads as

$$u^{inc}_{O}(\ \ ) = \int_{C\infty} f(\ \ ')G_O(\ \ ,\ \ ')dl'. \tag{4}$$

$'$ is a source point defined in the infinity. The two-dimensional free space Green's function is

$$G_{I,\,O}(\ \ ,\ \ ') = \frac{1}{4i}H^{(2)}_0(k_{I,\,O}|\qquad '|) \tag{5}$$

with $H^{(2)}_0(k_{I,\,O}|\qquad '|)$ being the Hankel function of second kind. To solve the two integral equations, the boundary conditions on C

$$\begin{aligned} u^{tot}_I(\ \ ) &= u^{tot}_O(\ \ ) \qquad \text{for} \quad \in C \\ \frac{1}{p_I}\frac{\partial u^{tot}_I(\ \ )}{\partial \hat{n}_I} &= \frac{1}{p_O}\frac{\partial u^{tot}_O(\ \ )}{\partial \hat{n}_O} \quad \text{for} \quad \in C \end{aligned} \tag{6}$$

are applied with $p_{I,O} = 1$ in the case of TE polarization and $p_{I,O} = {}_{I,O}$ for TM polarization. For a simplification of Eqn.2, the total field is written as a sum of the incident and scattered field

$$u^{tot} \;=\; u^{inc} + u^{sc}, \tag{7}$$

and the Sommerfeld radiation condition is incorporated

$$\int_{C_\infty} \quad u^{sc}(\ ')\frac{\partial G_O(\ ,\ ')}{\partial \hat{n}_I} \quad p_O G_O(\ ,\ ')v^{sc}(\ ')\Bigg)\, dl' = 0 \quad \text{for} \quad \in O. \tag{8}$$

The condition says that the scattered field must vanish in infinity. In addition we know, that if their is no scattering object, the total field is given by the incident field

$$u_O^{tot} \;=\; u_O^{inc}, \tag{9}$$

which makes it possible to simplify Eqn.2 by incorporating the following identity

$$\int_C \quad p_O G_O(\ ,\ ')v^{inc}(\ ') \quad u^{inc}(\ ')\frac{\partial G_O^{tot}(\ ,\ ')}{\partial \hat{n}_I}\Bigg)\, dl' = 0 \quad \text{for} \quad \in O \tag{10}$$

By using this identity and applying the Sommerfeld radiation condition, the boundary integral equations Eqn. 2 evaluated on the surface of the particle can be written as [2]

$$\begin{aligned}
0 \;&=\; u^{sc}(\ _S) + \int_C \left\{ u^{sc}(\ ')\frac{\partial G_I(\ _S,\ ')}{\partial \hat{n}_I} \quad p_I G_I(\ _S,\ ')v^{sc}(\ ') \right\} dl' \\
&+\; u^{inc}(\ _S) + \int_C \left\{ u^{inc}(\ ')\frac{\partial G_I(\ _S,\ ')}{\partial \hat{n}_I} \quad p_I G_I(\ _S,\ ')v^{inc}(\ ') \right\} dl' \quad \text{for} \quad _S \in I \\
0 \;&=\; u^{sc}(\ _S) + \int_C \left\{ u^{sc}(\ ')\frac{\partial G_O(\ _S,\ ')}{\partial \hat{n}_O} + p_O G_O(\ _S,\ ')v^{sc}(\ ') \right\} dl' \quad \text{for} \quad _S \in O,
\end{aligned} \tag{11}$$

which is Eqn. 2 of chapter 1. It has to be kept in mind that the contour normal pointing in the exterior space has a different sign than that pointing in the interior space, i.e. $\hat{n}_I = \quad \hat{n}_O$. Care has to be taken if $' = \ $, because a singularity appears in the Green's function. The problem can be overcome by

applying Cauchy's principal value of integral. Equation 11 may be cast into a set of linear equations by expanding the unknown scattered field $u^{sc}(\ _S)$ and its normal derivative $v^{tot}(\ _S)$ in terms of interpolation functions

$$\begin{aligned}
\mathbf{u}^{sc}(r_S(\xi)) &= \sum_{n=1}^{N} \hat{u}_n^{sc}(\xi) = \sum_{n=1}^{N} u_n^{sc}\ _1(\xi) + u_{n+1}^{sc}\ _2(\xi) \\
\mathbf{v}^{sc}(r_S(\xi)) &= \sum_{n=1}^{N} \hat{v}_n^{sc}(\xi) = \sum_{n=1}^{N} v_n^{sc}\ _1(\xi) + v_{n+1}^{sc}\ _2(\xi). \qquad (12)
\end{aligned}$$

The interpolation functions $\ _1(\xi)$ and $\ _2(\xi)$ are defined over a single element. In the present work linear interpolation functions have been used. They are defined as

$$\begin{aligned}
_1(\xi) &= \frac{1 \quad \xi}{2} \\
_2(\xi) &= \frac{1+\xi}{2}. \qquad (13)
\end{aligned}$$

ξ is defined in an interval between $\ \ 1$ and 1. Using the interpolation function, the contour of the scatterer is written as

$$\begin{aligned}
\hat{x}_n(\xi) &= x_n\ _1(\xi) + x_{n+1}\ _2(\xi) \\
\hat{y}_n(\xi) &= y_n\ _1(\xi) + y_{n+1}\ _2(\xi) \qquad (14)
\end{aligned}$$

The nodal values $\ _n(x_n, y_n)$ and $\ _{n+1}(x_{n+1}, y_{n+1})$ are sample points of the surface and $\hat{}_n\,(\hat{x}_n(\xi), \hat{y}_n(\xi))$ are the interpolated coordinates of single line element with length Δl_n. By introducing equations 14 and 12 in 11, the system of linear equations in matrix form reads [2]

$$\begin{bmatrix} ZI_{n,m} & p_I YI_{n,m} \\ ZO_{n,m} & p_O YO_{n,m} \end{bmatrix} \begin{bmatrix} u_m^{sc} \\ v_m^{sc} \end{bmatrix} = \begin{bmatrix} ZI_{n,m} & p_I YI_{n,m} \\ 0 & 0 \end{bmatrix} \begin{bmatrix} u_m^{inc} \\ v_m^{inc} \end{bmatrix}, \qquad (15)$$

where the coefficients $ZI_{n,m}$, $YI_{n,m}$, $ZO_{n,m}$, and $YO_{n,m}$ are defined as [2]

$$\begin{aligned}
ZI_{n,m} &= \left(1 \quad \frac{n}{2}\right)\ _{nm} \\
&+ \int_1^1 \left\{ \frac{\Delta l_n}{2}\ _1(\xi) \frac{\partial G_I(\ '(\hat{x}_n, \hat{y}_n),\ '_m)}{\partial \hat{n}_I} \right. \\
&+ \left. \frac{\Delta l_n\ _1}{2}\ _2(\xi) \frac{\partial G_I(\ '(\hat{x}_n\ _1, \hat{y}_n\ _1),\ '_m)}{\partial \hat{n}_I} \right\} d\xi,
\end{aligned}$$

$$
\begin{aligned}
YI_{n,m} &= \int_{1}^{1} \left\{ \frac{\Delta l_n}{2} \ {}_1(\xi) G_I(\ '(\hat{x}_n, \hat{y}_n),\ {}'_m) \right. \\
&+ \left. \frac{\Delta l_{n\ 1}}{2} \ {}_2(\xi) G_I(\ '(\hat{x}_{n\ 1}, \hat{y}_{n\ 1}),\ {}'_m) \right\} d\xi, \\
ZO_{n,m} &= \left. \frac{n}{2} \right) \ {}_{nm} \\
&+ \int_{1}^{1} \left\{ \frac{\Delta l_n}{2} \ {}_1(\xi) \frac{\partial G_O(\ '(\hat{x}_n, \hat{y}_n),\ {}'_m)}{\partial \hat{n}_I} \right. \\
&+ \left. \frac{\Delta l_{n\ 1}}{2} \ {}_2(\xi) \frac{\partial G_O(\ '(\hat{x}_{n\ 1}, \hat{y}_{n\ 1}),\ {}'_m)}{\partial \hat{n}_I} \right\} d\xi, \\
YI_{n,m} &= \int_{1}^{1} \left\{ \frac{\Delta l_n}{2} \ {}_1(\xi) G_O(\ '(\hat{x}_n, \hat{y}_n),\ {}'_m) \right. \\
&+ \left. \frac{\Delta l_{n\ 1}}{2} \ {}_2(\xi) G_O(\ '(\hat{x}_{n\ 1}, \hat{y}_{n\ 1}),\ {}'_m) \right\} d\xi, \qquad (16)
\end{aligned}
$$

with $d\xi = 2dl'/\Delta l_n$. Once the system of equations 15 is solved and the scattered field and its derivation is known over the entire surface of the object, the scattered field can be calculated everywhere in space using

$$
u^{sc}(\ ) = \int_C \left\{ u^{sc}(\ ') \frac{\partial G_O(\ ,\ ')}{\partial \hat{n}_I} \quad G_O(\ ,\ ') v^{sc}(\ ') \right\} dl'. \qquad (17)
$$

In a final step the total field is calculated by adding the field distribution of the incoming wave.

References

[1] H. El-Mikati and J. B. Davies, "Improved boundary element techniques for two-dimensional scattering problems with circular boundaries", IEEE Trans. Antennas Propag., AP-35, 539 (1987)

[2] D. W. Prather, M. S. Mirotznik and J. N. Mait, "Boundary integral method applied to the analysis of diffractive optical elements", JOSA A, Vol. 14, 34 (1997)

[3] D. W. Prather, J. N. Mait, M. S. Mirotznik and J. P. Collins, "Vector-based synthesis of finite aperiodic subwavelength diffractive optical elements", JOSA A, Vol. 15, 1599 (1998)

Appendix II

Gauss-Hermite and Gauss-Laguerre beams

The amplitude of a Gauss-Hermite beam of order (m, n) in the point (x, y, z) is given by[1]

$$U_{mn}(x,y,z) = \frac{\omega_0}{\omega} H_m \quad \sqrt{2}\frac{x}{\omega} \quad H_n \quad \sqrt{2}\frac{y}{\omega} \quad e^{i[kz \quad \Phi_{mn}(z)]} \; e^{ik\frac{x^2+y^2}{2R}} \; e \quad ^{\frac{x^2+y^2}{\omega^2}}, \quad (1)$$

ω_0 is the beam width in the waist, the radius of curvature $R(z)$ is given by

$$R(z) = z \quad 1 + \frac{z_0^2}{z^2}\Big) \quad (2)$$

and the beam width ω is

$$\omega(z)^2 = \omega_0^2 \quad 1 + \frac{z^2}{z_0^2}\Big) . \quad (3)$$

z_0 is the Rayleigh-distance defined by

$$z_0 = \underline{\quad \omega_0^2} \quad (4)$$

with being the wavelength. The Hermite-polynomial of order m is given by

$$H_m(\zeta) = (\quad 1)^m \; e^{\zeta 2} \frac{d^n}{dx^n} e \quad ^{\zeta 2} \quad (5)$$

and the phase of the laser mode reads as

$$\Phi_{mn}(z) = (1 + m + n)\Phi(z) \quad (6)$$

with

$$tan \; \Phi(z) = \frac{z}{z_0}. \quad (7)$$

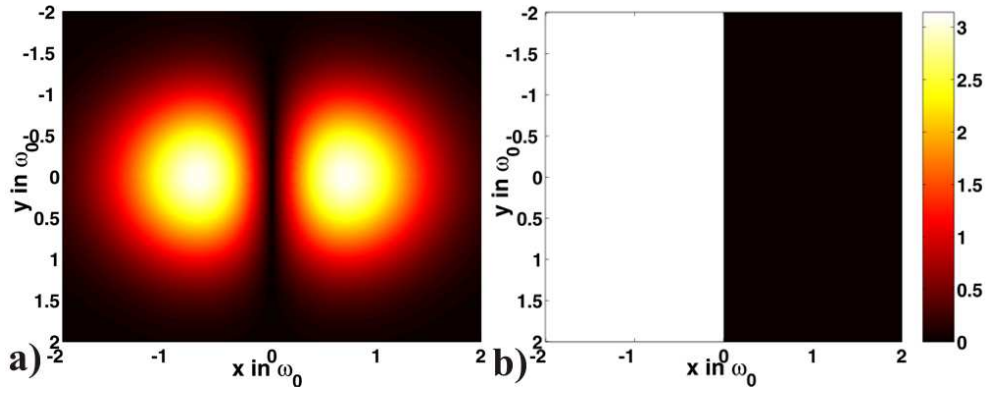

Figure 1: Amplitude (a) and phase (b) distribution of a Gauss-Hermite beam of order $(1, 0)$.

As an example for a field distribution of a Gauss-Hermite beam, Fig. 1 shows the amplitude and phase for a beam of order $(1, 0)$. As one can see, a dislocation of the edge type appears along the y-axis, the phase jumps at . The amplitude of a Gauss-Hermite beam of order $(2, 3)$ is shown in Fig. 2. The beam has 2 edge dislocations related to the x-coordinate and 3 with respect to the y-coordinate.

The amplitude of a Gauss-Laguerre beam is given by a simmilar equation

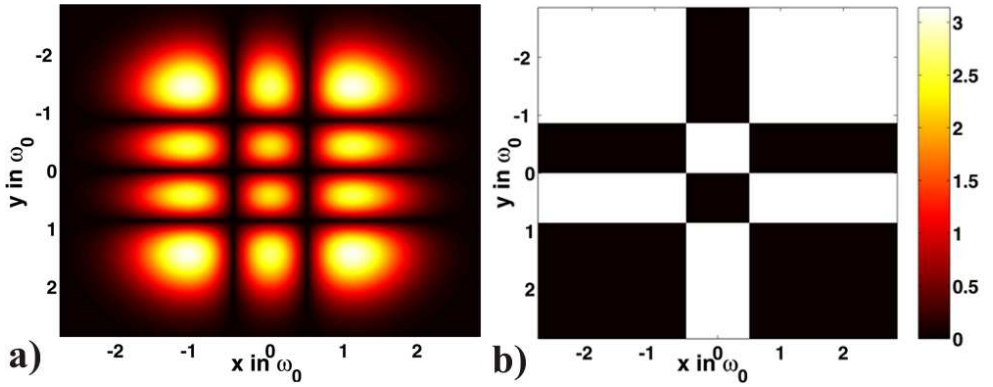

Figure 2: Amplitude (a) and phase (b) distribution of a Gauss-Hermite beam of order $(2, 3)$.

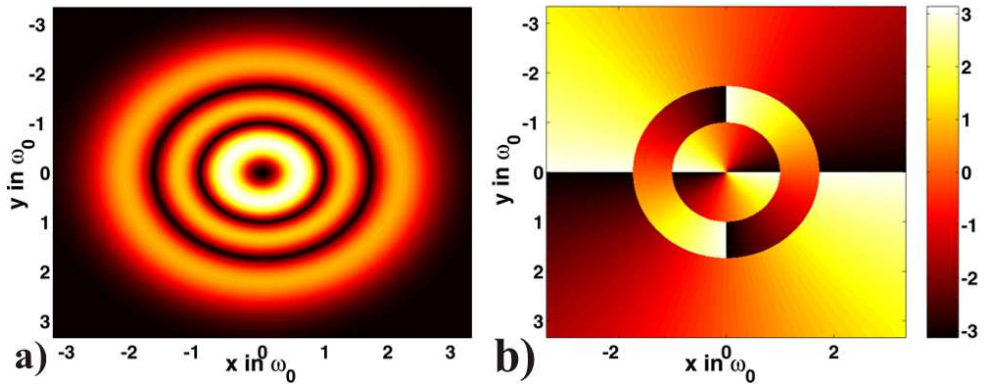

Figure 3: Amplitude (a) and phase (b) distribution of a Gauss-Laguerre beam of order $(2, 2)$.

as Eqn. 1 and reads as [1]

$$U_{pl}(r, \ , z) = \ \sqrt{2}\frac{r}{\omega} \ ^2 L_p^l \ \ 2\frac{r^2}{\omega^2}\Big) \ e^{i\theta l} \ e^{i\left[kz \ \ \Phi_{pl}(z)\right]} \ e^{ik\frac{r^2}{2R}} \ e \ ^{\frac{r^2}{\omega^2}}. \tag{8}$$

p is the radial and l the axial mode parameter. The azimuthal mode parameter corresponds to the strength of the screw singularity associated with the term $e^{i\theta l}$ and the radial mode parameter gives the number of points with zero intensity in the radial direction. Along each of the appearing circles with no intensity, the phase jumps at .
The generalized Laguerre polynomial is defined as

$$L_p^l(\zeta) = \sum_{n=0}^{p} \ \frac{p+l}{p \quad l}\Big) \ \frac{\zeta^n}{n!}. \tag{9}$$

The phase term $\Phi_{pl}(z)$ is given by

$$\Phi_{pl}(z) = (2p+ \mid l \mid +1)\Phi(z). \tag{10}$$

As an example for a Gauss-Laguerre beam, Fig. 3 shows the amplitude and phase distribution of a beam with the mode parameter $(2, 2)$.

For comparison of the measured intensity and phase distributions as presented in the publication "High-resolution measurement of phase singularities produced by computer-generated holograms", Fig. 4 till 7 show the intensity and phase distributions of a Gauss-Laguerre beam with a radial mode

parameter of $p = 0$ and with an increasing azimuthal mode parameter from $l = 1$ till $l = 4$.

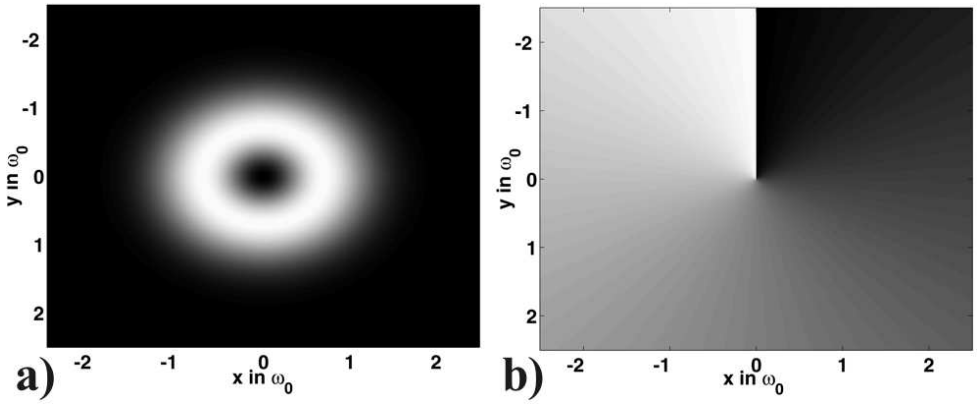

Figure 4: Intensity (a) and phase (b) distribution of a Gauss-Laguerre beam of order (0, 1).

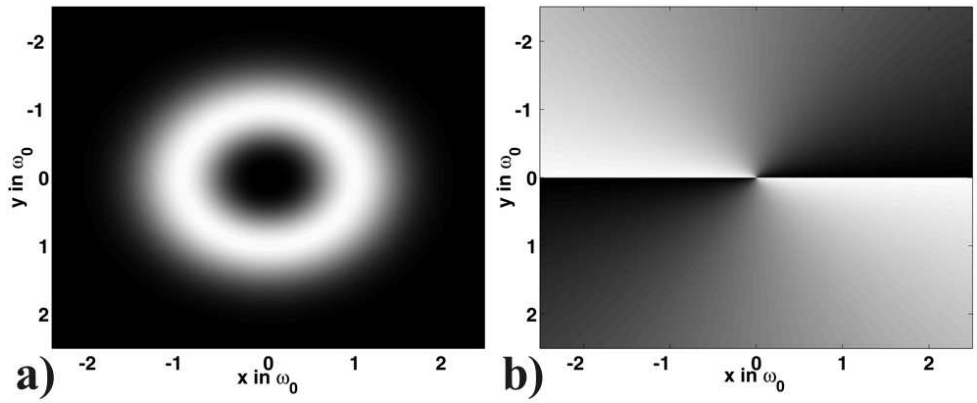

Figure 5: Intensity (a) and phase (b) distribution of a Gauss-Laguerre beam of order $(0, 2)$.

References

[1] H. Kogelnik und T. Li, , "Laser Beams and Resonators", Proc. IEEE, Vol. 54, 1312, (1966)

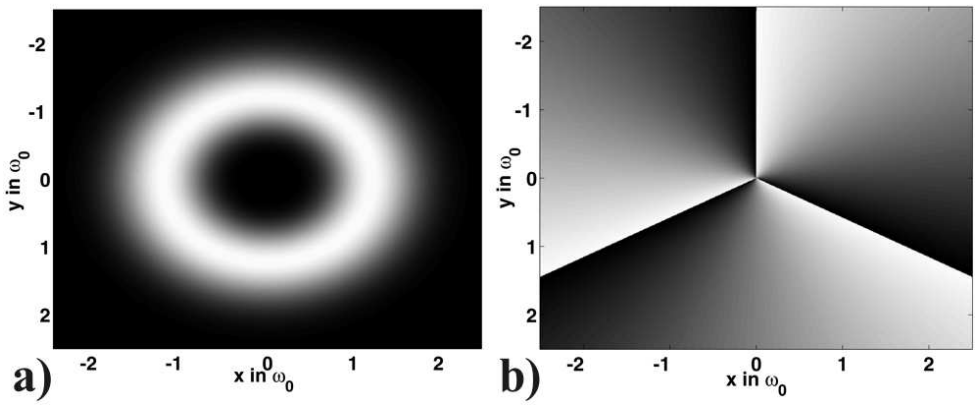

Figure 6: Intensity (a) and phase (b) distribution of a Gauss-Laguerre beam of order $(0, 3)$.

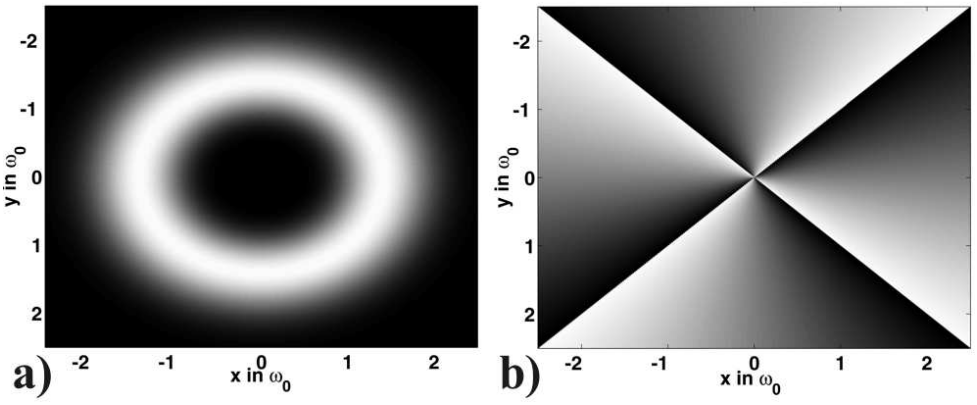

Figure 7: Intensity (a) and phase (b) distribution of a Gauss-Laguerre beam of order $(0, \quad 4)$.

Acknowledgements

After all the scientific contents of this thesis, it is a personal pleasure of the author to thank all the people and institutions, who supported me during the time of this work in different ways, both scientific and personal.

- First of all and most important, I would like to thank my thesis advisor Professor Hans Peter Herzig for accepting me as an aspirant and for making available such a pleasant working environment. His fascination about optics and his creativity causing never ending new ideas on how to progress in our research, was a constant stimulation for a continuation of my work and for extending it to new adjacent fields. I thank him for giving me the freedom to choose the details of my specific research.

- Similar, I would like to thank Professor Rene Dändliker for his guidance throughout the time of my thesis and my trainee period. Especially I deeply acknowledge his encouragement for being accepted by the faculty as a research assistant than can submit a PhD-thesis.

- Dr. S. Quabis and Prof. C. Hafner I would like to thank for being the members of my jury, that they took themselves the time to read my thesis and for their critical annotations.

- I would like to take the chance to thank all the anonymous reviewer of my publications and to highly appreciate their effort in revising the manuscripts. And of course, I thank all the editors from the various journals for finally accepting them.

- I would like to thank the European Union for supporting this research within the project acronymed as SLAM. The project about Super Laser Array Memory. In this context I would like to appreciate the collaboration with all the contributing partners and the stimulating discussions we had.

Acknowledgements.

- Dr. M. Salt is thanked for being the direct supervisor of my work, for his constructive revisions of my publications and for keeping the administrative aspects of my work on an enjoyable negligible level. Besides the scientific aspects, I thank him for his sense of humour, which made me laughing about boring aspects of our work that could appear from time to time too.

- Dr. W. Nakagawa is thanked for teaching me the American way of writing publications, applications, and scientific texts in general. I thank him for renting me his "Simpsons" and "Futurama" DVD-collection and for being a friend, no matter where we currently live or in the future.

- I thank Drs. A.S. van de Nes from the Technical University in Delft, The Netherlands for his guidance meanwhile my first contact with the technique of calculating numerically Green's functions and for the fabrication of various samples that have been used for the research about phase singularities.

- I thank Dr. J. Pezoldt from the Technical University Ilmenau, Germany for making available the silicon carbide samples.

- For general discussions about singular optics and for making available samples used in the CGH-measurements I thank Prof. M. Soskin and A. Ivanovskyy from the National Academy of Science Ukraine in Kiev.

- I thank the group of Prof. J. Faist and especially R. Maulini from the Institute of Physics at the University of Neuchâtel for the assistance in the spectroscopic measurements in the infra-red.

- Dr. E. Kriezis from the Aristotle University of Thessaloniki, Greece is thanked for indicating some secrets about the FDTD to me.

- J. Guillet is thanked for the discussions in the work about solar cells.

- I thank S. Olibet for contributing within a semester work about the subject of negative refraction.

- Dr. W. Noell, Dr. R. Völkel, and Dr. T. Scharf are thanked for their collaboration in the investigation about the influence of phase or amplitude apertures used for the focal point shaping of microlenses.

Acknowledgements.

- I would like to thank my bureau colleague and the other grand SLAMmer E. Descrovi for the pleasant atmosphere in the office, for his Italian way on the telephone that made me always smile ("Ciao, Ciao, Ciao, Ciao, Ciao, Ciao,Ciao"), for the unforgettable discussion about Olivier Toscani and for being always there if I was stuck in a problem or had a question.

- Dr. T. Scharf is thanked for being Dr. T. Scharf, his adorable sense of humor, for taking the world with all its terrestrial problems not too serious and for his amazing ability to undermine expectations in different situations.

- Finally I thank all the members of the Applied Optics group and more generally of the Institute of Microtechnology for the nice and stimulating atmosphere.

- I would like to thank Christian Bohley, from which I could learn so much, probably most notably, to learn how to learn. He brought always new ideas, concepts and, more practical, literature, music and films to my attention, such that the time I spent in Neuchâtel became an important period in being socialized and in the development of (something like) a personality (no matter what that means).

- Ditto I owe so much to Thomas Zentgraf, that some single lines are not enough to express my gratitude for his encouragement, support and often direct help for my work and all the things beyond the scientific issues from the very first beginning. Many, many thanks.

- A great thanks, merci, domo harigato gozaimasu, and dankeschön goes to all the Sabloniers for the time we spent together in Neuchâtel, especially Alexis Gabadinho, Stefanie Kühn, Paul Beziers and Tomoko Hatasaki.

- I would like to thank Bernard Lenoir, John Peel, Gilles Peterson and all the other DJ's from the BBC Radio 1 for providing me with my daily dose of Pop-candies.

- Finally, I will deeply thank all my parents, my brothers, my friends in Germany and Switzerland for their help, encouragement and support during all the last years.